DEVELOPMENT OF A NOVEL NON-INVASIVE IMAGING TECHNIQUE FOR CHARACTERIZING SUBCHONDRAL BONE DENSITY AND STIFFNESS

by

JAMES DUNCAN JOHNSTON

A Thesis Submitted in Partial Fulfillment of the
Requirements for the Degree of

DOCTOR OF PHILOSOPHY

in

THE FACULTY OF GRADUATE STUDIES

(Mechanical Engineering)

THE UNIVERSITY OF BRITISH COLUMBIA
(VANCOUVER)

December 2010

ABSTRACT

Osteoarthritic (OA) subchondral bone is marked by mechanical and morphological alterations which are thought to influence cartilage integrity, leading to degeneration. The exact role of subchondral bone in OA etiology is, however, unclear and much of our understanding of OA-related subchondral bone changes has come from animal models or cadaveric specimens as opposed to *in vivo* assessments of people living with OA.

The objectives of this thesis were to 1) develop a noninvasive clinical imaging tool capable of measuring proximal tibial subchondral bone density—a surrogate measure of bone stiffness, 2) compare subchondral bone density differences between normal and OA knees using this novel imaging technique with an existing maximum intensity projection technique, 3) determine the *ex vivo* and *in vivo* precision of proximal tibial subchondral bone density measures using this novel imaging technique, and 4) determine whether this novel imaging technique can be used to predict bone stiffness values obtained using mechanical indentation testing.

We developed the novel imaging tool: computed tomography topographic mapping of subchondral density (CT-TOMASD), which characterizes and maps 3D subchondral bone mineral density (BMD) in relation to depth from the subchondral surface. *Ex vivo* comparisons between OA and normal knees revealed significantly higher density (17-36%) in OA knees. CT-TOMASD was more proficient than the maximum intensity projection technique at distinguishing density pattern differences between OA and normal knees. CT-TOMASD precision errors were <4.3%; ~9x smaller than observed BMD differences between OA and normal knees. CT-TOMASD predicted (r^2 = 0.67), non-invasively, subchondral bone structural stiffness directly at the subchondral surface. The relationship between subchondral bone density and stiffness was non-linear, whereby small differences in density resulted in large stiffness differences. This information could explain the mechanical role of subchondral bone in OA more effectively than bone density alone.

CT-TOMASD has potential to identify and quantify changes in subchondral bone density and stiffness associated with OA disease progression. This information could be used to test hypotheses regarding the mechanical role of subchondral bone in people living with OA, which could lead to early OA detection and assist with treatment methods aimed at preventing or delaying OA.

PREFACE

Sections of this thesis have been submitted as multi-authored papers in refereed journals. The research was performed by me except for computed tomography imaging, which was carried out by trained technicians, and clinical diagnoses, which were carried out by a participating orthopaedic surgeon. Data analyses and manuscript preparation were carried out by me and the co-authors contributed in editing the manuscripts for submission to refereed journals.

Published Papers

1. Johnston JD, Masri BA, Wilson DR. Computed tomography topographic mapping of subchondral density (CT-TOMASD) in osteoarthritic and normal knees: methodological development and preliminary findings. *Osteoarthritis and Cartilage*. 2009; 17(10):1319-1326. Epub 2009 May 4.

   Authors' contribution: J.D. Johnston was jointly responsible for the original ideas behind the paper, conducting the experiments, image and data analyses, presentation of the findings, and writing and editing of the original paper. Dr. Bassam Masri conducted the clinical evaluations. Dr. David Wilson was jointly responsible for the original ideas, provided supervision, and was the key editor on this paper. This research is discussed in Chapter 2 of this thesis.

   The results in this study were presented at national and international conferences:

   i. Osteoarthritis Research Society International World Congress, Fort Lauderdale, FL, USA, 2007 December 6-9, Paper No. 305.
   ii. Orthopaedic Research Society, San Francisco, CA, USA, 2008 March 2-5, Paper No. 194. *Selected for oral podium presentation*
   iii. Canadian Orthopaedic Research Society Meeting, Quebec City, QC, 2007 June 4-7.

2. Johnston JD, Kontulainen SA, Masri BA, Wilson DR. A comparison of conventional maximum intensity project with a new depth-specific topographic mapping technique in the CT analysis of proximal tibial subchondral bone density. *Skeletal Radiology*. 2010; 39(9): 867-876. Epub 2009 November 22.

   Authors' contribution: J.D. Johnston was jointly responsible for the original ideas behind the paper, conducting the experiments, image and data analyses, presentation of the findings, and

writing and editing of the original paper. Dr. Saija Kontulainen assisted with statistical analyses and edited the original paper. Dr. Bassam Masri conducted the clinical evaluations. Dr. David Wilson was jointly responsible for the original ideas, provided supervision, and was the key editor on this paper. This research is discussed in Chapter 3 of this thesis.

The results in this study were presented at national and international conferences:

i. Orthopaedic Research Society, Las Vegas, Nevada, USA, 2009 February 21-25, Paper No. 2137.
ii. Canadian Orthopaedic Research Society Meeting, Whistler, BC, Canada, 2009 July 3-5, Paper No. 32. *Selected for oral podium presentation*.

3. Johnston JD, McLennan CE, Hunter DJ, Wilson DR. *In vivo* precision of a depth-specific topographic mapping technique in the CT analysis of osteoarthritic and normal proximal tibial subchondral bone density. *Skeletal Radiology*. Epub 2010 September 3.

Authors' contribution: J.D. Johnston was jointly responsible for the original ideas behind the paper, conducting the experiments, image and data analyses, presentation of the findings, and writing and editing of the original paper. Christine McLennan recruited study participants and was involved in the original study design. Dr. David Wilson and Dr. David Hunter were jointly responsible for the original ideas, provided supervision, and were key editors on this paper. This research is discussed in Chapter 4 of this thesis.

The results in this study were also presented at national and international conferences:

i. 2nd International Workshop on Imaging Based Measures of Osteoarthritis, Boston, MA, USA, 2008 June 25-28.
ii. Orthopaedic Research Society, Las Vegas, Nevada, USA, 2009 February 21-25, Paper No. 242. *Selected for oral podium presentation.*
iii. International Society for Technology in Arthroplasty, Big Island, Hawaii, 2009 October 22-24, Paper No. A973. *Best poster award.*

Submitted Papers

4. Johnston JD, Kontulainen SA, Masri BA, Wilson DR. Predicting subchondral bone stiffness using a depth-specific CT topographic mapping technique in normal and osteoarthritic proximal tibiae. *Osteoarthritis and Cartilage*. Submitted 2010 July 9.

   Authors' contribution: J.D. Johnston was jointly responsible for the original ideas behind the paper, conducting the experiments, image and mechanical data analyses, presentation of the findings, and writing and editing of the original paper. Dr. Saija Kontulainen assisted with statistical analyses and edited the original paper. Dr. Bassam Masri conducted the clinical evaluations. Dr. David Wilson was jointly responsible for the original ideas, provided supervision, and was the key editor on this paper. This research is discussed in Chapter 5 of this thesis.

   The results in this study were (or will be) presented at national and international conferences:

   i. Canadian Orthopaedic Research Society Meeting, Edmonton, AB, Canada, 2010 June 17-20. Paper 32.
   ii. American Society for Bone and Mineral Research, Toronto, ON, Canada, 2010 October 15-19. *Nominated for Young Investigator Award.*

Areas of this thesis research required approval of the UBC Clinical Research Ethics Board:
UBC CREB NUMBER: H03-70308. *New Coordinate Applications for Bone Health: Effects of Bone Weakening of Joint Health*. Principal Investigator: Wilson DR, Co-Investigators: McWalter EJ, Johnston JD, LaFrance AE. Expiration: August 1, 2009.

TABLE OF CONTENTS

LIST OF TABLES

LIST OF FIGURES

GLOSSARY

TERMS	DEFINITION
Anterior	Front plane of a body (i.e., belly)
Apparent bone mineral density	Imaging measure of bone mass / total image area (DXA) or volume (QCT)
Apparent density	Laboratory measure of hydrated bone mass / total specimen volume (g/cm3); synonymous with wet apparent density
Areal apparent bone mineral density	Imaging measure of bone mineral content / image area (g/cm^2) as measured by DXA
Ash content	Laboratory measure of ash mass / bone volume (g/cm^3)
Ash density	Laboratory measure of ash mass / total specimen volume (g/cm^3)
Axial	Plane that divides the body into superior and inferior parts; synonymous with transverse plane
Bone density	General term referring to the mass of bone within a specified volume. Refers to apparent bone mineral density, areal apparent bone mineral density, volumetric apparent bone mineral density and apparent density
Cancellous	Type of bone tissue comprised of vertical and horizontal trabeculae which create a spongy, cellular-like tissue; typically occurs at the ends of long bones; high surface area compared to cortical bone and is therefore more metabolically active; synonymous with trabecular bone
Compact bone	Type of bone tissue comprised of multiple layers of compacted bone; forms the cortex or outer shell of bone; much denser, stronger and stiffer than cancellous bone; synonymous with cortical bone
Coronal	Plane that divides the body into anterior and posterior sections
Cortical bone	Type of bone tissue comprised of multiple layers of compacted bone; forms the cortex or outer shell of bone; much denser, stronger and stiffer than cancellous bone; synonymous with compact bone
Distal	Pertains to different ends of an extremity; distal end of extremity is the end situated farthest from the center of the body (e.g., distal tibia is located at ankle joint)

TERMS	DEFINITION
Inferior	Bottom plane of a body (i.e., bottom of feet)
In situ	Latin for “in the place”; in biomechanics refers to experimentation of a largely intact structure (i.e., joint or entire bone) as opposed to (*in vitro*) experimentation of a small tissue or bone sample
In vivo	Latin for “within the living”; experimentation using a whole, living organism as opposed to partial or dead organism
In vitro	Latin for “within the glass”; in biomechanics refers to experimentation of a small tissue or bone sample excised from a larger structure as opposed to (*in situ*) experimentation of a complete or largely intact structure
Joint space narrowing	Reported change in joint space width
Joint space width	Radiographically measured distance between two articulating bones
Lateral	Situated at or extending to the side
Material density	Laboratory measure of bone mass / bone volume (g/cm^3)
Material stiffness	Describes intrinsic material properties of bone itself; independent of specimen geometry or size
Medial	Situated at or extending to the middle
Osteoid	New, unmineralized bone tissue
Osteophyte	Bony projection that forms along the periphery of joints, also known as bone spurs
Posterior	Back plane of a body (i.e., back)
Proximal	Pertains to different ends of an extremity; proximal end of extremity is the end situated nearest the center of the body (e.g., proximal tibia is located at knee joint)
Sagittal	Plane that travels from the top to the bottom of the body, dividing it into left and right portions
Sclerosis	Generally referred to as a stiffening or hardening of a structure

TERMS	DEFINITION
Structural stiffness	Describes bone's response to deflection; dependent upon both material stiffness properties and physical size of the bone tissue being tested
Subchondral bone	Bone below (sub) cartilage (chondral)
Superior	Top plane of a body (i.e., top of head)
Trabecular bone	Type of bone tissue comprised of vertical and horizontal trabeculae which create a spongy, cellular-like tissue; typically occurs at the ends of long bones; high surface area compared to cortical bone and is therefore more metabolically active; synonymous with cancellous bone
Trabeculae	Latin for "small beam"; bone tissue element in the form a small beam, strut or rod
Transverse	Plane that divides the body into superior and inferior parts; synonymous with axial plane
Valgus	Outward angulation of the distal segment of a bone or joint; at the knee synonymous with "knock-kneed"; opposite of varus
Varus	Inward angulation of the distal segment of a bone or joint; at the knee synonymous with "bow-legged"; opposite of valgus
Volumetric apparent bone mineral density	Imaging measure of bone mineral content / image volume (g/cm^3) as measured by QCT
Wet apparent density	Laboratory measure of hydrated bone mass / total specimen volume (g/cm^3); synonymous with apparent density

ABBREVIATION	DEFINITION
2D	Two dimensional
3D	Three dimensional
aBMD	2D areal apparent bone mineral density (mg/cm^2); DXA measure
BM/BV	Material density (bone mass / bone volume)
BM/TV	Apparent density (bone mass / total volume)
BV/TV	Bone volume fraction (bone volume / total volume)
BMC	Bone mineral content (mg)
BMD	Apparent bone mineral density
BW	Body weight
CI	Confidence interval, as in 95% confidence interval
CT	Computed tomography
CT-OAM	Computed tomography osteoabsorptiometry
CT-TOMASD	Computed tomography topographic mapping of subchondral density
CV%	Percentage coefficient of variation
DEXA	Dual energy x-ray absorptiometry, same as DXA
DOF	Degrees of freedom
DPA	Dual photon absorptiometry; precursor to DXA
DXA	Dual energy x-ray absorptiometry, same as DEXA
ECM	Extracellular matrix
FE	Finite element
FSA	Fractal signature analysis
GLM	Generalized linear model

ABBREVIATION	DEFINITION
HMH	Half maximum height
HU	Hounsfield unit
ICC	Intraclass correlation coefficient
ICRS	International cartilage repair society
JSN	Joint space narrowing
JSW	Joint space width
K_2HPO_4	Dipotassium phosphate
KL	Kellegren-Lawrence scoring method
mKL	Modified Kellgren Lawrence
M:L	Medial : Lateral
MRI	Magnetic resonance imaging
OA	Osteoarthritis
OP	Osteoporosis
PBS	Phosphate buffered saline
PMMA	Poly(methyl methacrylate)
pQCT	Peripheral Quantitative computed tomography
PVC	Polyvinylchloride
QCT	Quantitative computed tomography
RMS	Root mean square
ROI	Region of interest
SD	Standard deviation
vBMD	3D volumetric apparent bone mineral density (mg/cm^3); QCT measure

SYMBOLS	DEFINITION
δ	Deflection (mm)
ρ	Apparent density (mg/cm^3)
υ	Poisson's ratio
d	Depth (mm)
E	Material stiffness, Modulus of elasticity, Young`s modulus (MPa)
F	Force (N)
k	Structural stiffness; slope of load/displacement curve (N/mm)
γ	Exponent of non-linear stiffness-density relationship (i.e., E = ρ^{γ})

ACKNOWLEDGEMENTS

I would like to thank my wife Saija for her support and endless patience.

I would like to thank my family, Mary, Jim, Lindsay, Hattie, Poe and Jack for their support and understanding.

I would like to thank Dr. David Wilson for his mentorship, supervision and support.

I would like to thank my previous mentors including Dr. Phil Noble, Dr. Carolyn Small, Dr. Edmund Biden, Gerry Saunders, Mr. MacCormack and Mr. Buley for their teachings and guidance.

I would like to thank the 16 anonymous men and women who donated their bodies to science and participated in this study.

I would like to thank the 14 men and women who volunteered to participate in this study.

I would like to thank Dr. Bassam Masri for spending his valuable time carrying out clinical evaluations.

I would like to thank my research committee, Dr. David Wilson, Dr. Tom Oxland, Dr. Robert Rohling and Dr.Rizhi Wang for their guidance.

I would like to thank my examination committee, Dr. Douglas Romilly, Dr. Purange Abolmaesumi and Dr. Cari Whyne for their input and recommendations regarding this thesis.

I am grateful for the special assistance given by staff and fellow students of the Division of Orthopaedic Engineering Research, in particular, Emily McWalter, Jennifer Douglas, Amy LaFrance, Derek Wilson, Claire Jones, Dr. Qing-An Zhu, Chad Larsen and Dr. Anthony Choo.

I am grateful for the special assistance given by staff and researchers at the New England Baptist Hospital, including Pam Connor, Sue Baker, Carol Grill, Christine McLennan and Dr. David Hunter.

There are also many others who have helped in some way including Dean Malpas, Keenan Brown, Dr. Peter Cripton, Dr. Antony Hodgson, Yuki Matsumura, Dr. Don Bergstrom, Dr. Jim Bugg, Dr. Allan Dolovich, Dr. Richard Burton and faculty and staff with the Department of Mechanical Engineering at the University of Saskatchewan.

I would like to acknowledge funding from the Natural Sciences and Engineering Research Council of Canada, the Michael Smith Foundation for Health Research, the Canadian Arthritis Network and the Canadian Institutes of Health Research.

1 Introduction

1.1 Overview

Osteoarthritis (OA) is a painful, debilitating disease involving cartilage degeneration at joint surfaces. OA affects almost 3 million Canadians; roughly half exhibiting knee OA [1]. Currently, there are no tools for early OA detection, and thus, OA is usually not diagnosed until after significant cartilage loss.

In addition to cartilage degeneration, OA is marked by mechanical and morphological changes in the underlying subchondral bone which have been proposed to influence cartilage integrity, leading to joint degeneration [2-4]. Repetitive, high impact loading is thought to trigger changes in the underlying subchondral bone, resulting in increased remodeling effects, bone formation, and stiffer subchondral bone. A stiffened subchondral bone will be less able to deform under dynamic impact loading (i.e., transfer strain energy), leading to more energy being transferred through the overlying cartilage. This would lead to higher internal cartilage stresses, cartilage breakdown, and eventual OA [2-4]. However, the exact role of subchondral bone in the etiology of OA is unclear. To date, much of our understanding of OA-related subchondral bone changes has come from animal models or cadaveric specimens.

There is a need for a tool to assess subchondral bone changes non-invasively in living people. Various imaging studies have shown direct relationships between apparent bone mineral density (BMD), a measure of bone mass per unit volume (or area), and the presence or severity of knee OA [5-12]. Apparent BMD is commonly regarded as a surrogate measure of bone stiffness, therefore subchondral BMD measures may help explain the role of subchondral bone in OA. These studies have generally assessed BMD at sites remote from the affected joint, though evidence from both human and animal studies suggests that subchondral bone located nearest to the overlying articular cartilage plays a significant role in the initiation, acceleration and/or progression of OA [13-20]. The few research studies examining direct associations between knee BMD and knee OA offer conflicting results [10, 12,

21-28]. The conflicting results are likely due to limitations of the imaging tools used to assess BMD combined with selected analysis regions containing different types of subchondral bone (subchondral cortical, subchondral trabecular, epiphyseal trabecular bone), which differ in location and depth from the subchondral surface and may each be affected differently by OA [17, 28, 29].

Available clinical imaging tools for bone density assessment are poorly suited for analyzing region- and depth- specific variations in bone density at the knee. The planar nature of dual energy x-ray absorptiometry (DXA) is limited to two-dimensional (2D) measures of areal BMD (aBMD, mg/cm^2). Correspondingly, 2D DXA projections cannot distinguish between subchondral cortical and trabecular bone near the subchondral surface or characterize 3D density at defined depths from the subchondral surface. Peripheral quantitative computed tomography (pQCT) is capable of assessing volumetric BMD (vBMD, mg/cm^3); however, pQCT analyses are generally limited to epiphyseal trabecular bone regions because pQCT is limited to a single axial CT scan of fixed slice thickness (typically 2.3 mm).

Clinical QCT offers a promising alternative to DXA- and pQCT-based measures of subchondral bone density. QCT offers wide availability using clinical CT scanners [30, 31], short acquisition times (seconds) for large 3D datasets (300+ slices), and small isotropic voxel sizes (0.5–0.625 mm) which permit density characterizations of thin bony layers near the subchondral surface.

In addition to characterizing subchondral bone density, clinical QCT could potentially be used to non-invasively predict subchondral bone stiffness. By linking QCT-derived measures of density with laboratory-based measures of subchondral bone stiffness, it may be possible to derive stiffness-density relationships for non-invasive predictions of subchondral bone stiffness. This information could help explain the role of subchondral bone alternations in OA etiology more effectively than bone density alone, particularly if relationships between stiffness and density are nonlinear. Importantly, non-invasive stiffness predictions could be used to directly test hypotheses regarding the mechanical role of subchondral bone in people living with OA.

There is presently no cure for OA, and the exact etiology is unknown. Examining subchondral bone density and stiffness *in vivo*, especially at early stages of OA, could help elucidate the role of subchondral bone in OA disease initiation and development. This information could lead to early OA detection and assist with monitoring treatments such as bracing or bone-modifying drugs aimed at preventing or delaying OA onset and progression.

The overall goal of my dissertation research was to develop a tool to improve the current understanding of OA pathogenesis. Using QCT imaging and a novel image processing technique, in combination with mechanical indentation testing, I developed a method to characterize 3D subchondral bone density and estimate bone stiffness *in vivo*.

1.2 Functional Anatomy

1.2.1 Knee Joint

The knee joint (Figure 1-1) is comprised of three bones; the proximal tibia, the distal femur, and the patella. Two different articulating joints are present at the knee: the patello-femoral joint and tibio-femoral joint. The tibio-femoral joint permits flexion and extension of the leg and is the main load bearing joint in the knee. The bone of interest related to this work is the proximal tibia, which is often a site for OA disease. The proximal tibia is comprised of separate medial and lateral compartments. The medial compartment is the more loaded compartment; supporting approximately 70% of total joint load during the stance phase of gait [32].

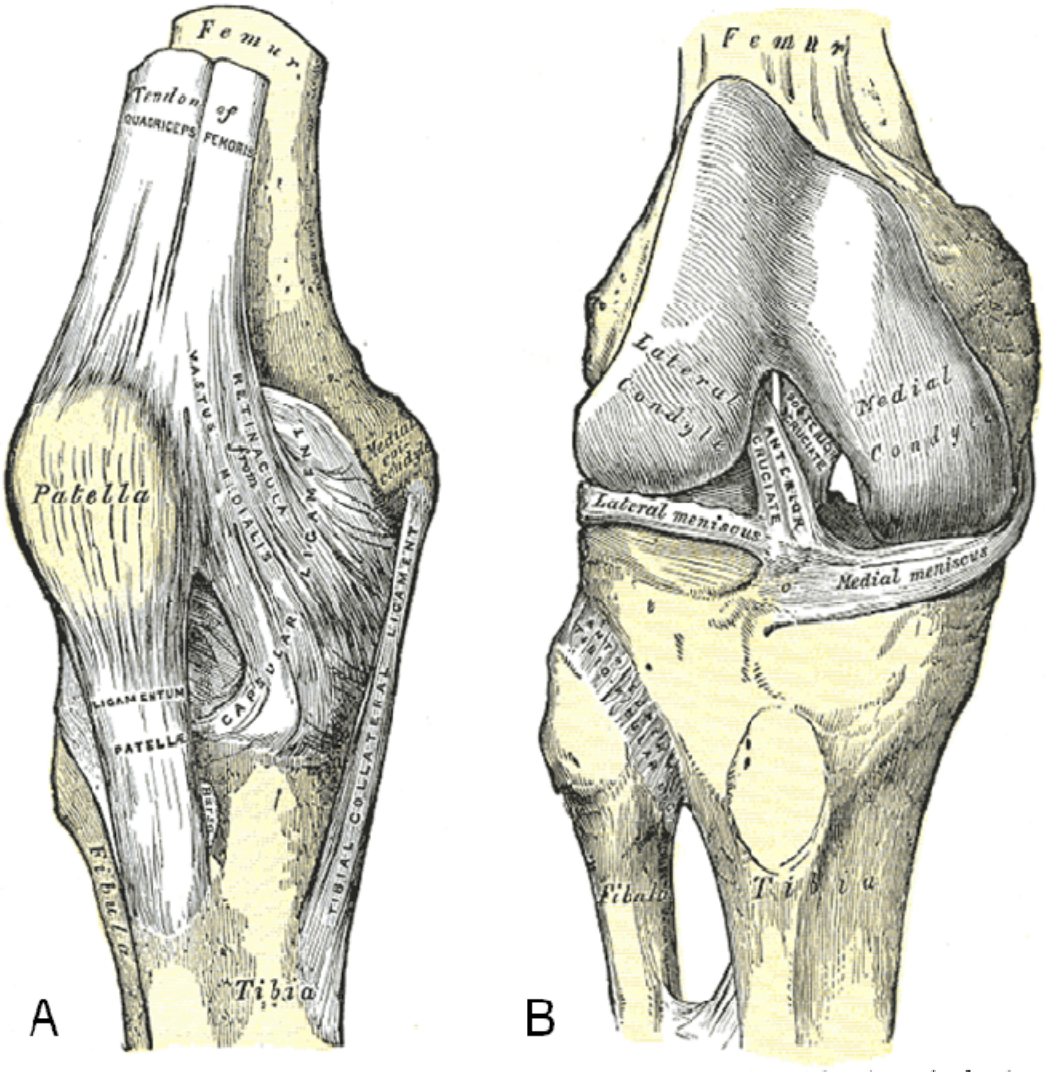

Figure 1-1. *A.* Anterior view of bones of knee joint, including the patella. *B.* Anterior view of bones of knee joint.. Displayed bones include the proximal tibia and corresponding medial and lateral compartments, fibula, and the distal femur and corresponding medial and lateral condyles. Modified from Gray's Anatomy [33].

1.2.2 Meniscus

Between the articulating surfaces of the distal femur and proximal tibia lie two c-shaped wedges of fibrocartilage called menisci, which are semi-rigidly attached to the medial and lateral proximal tibial compartments (Figure 1-2). The main functions of the menisci are stability and load transmission to the underlying articular cartilage during movement and loading [34-36]. The meniscus covers 59-71% of the corresponding articular cartilage along the anterior, posterior and peripheral regions of each compartment [36, 37]. Approximately 50% of the load on the proximal tibia is distributed through the meniscus to the underlying articular cartilage; particularly along the thin regions near the centre of each compartment [38-40].

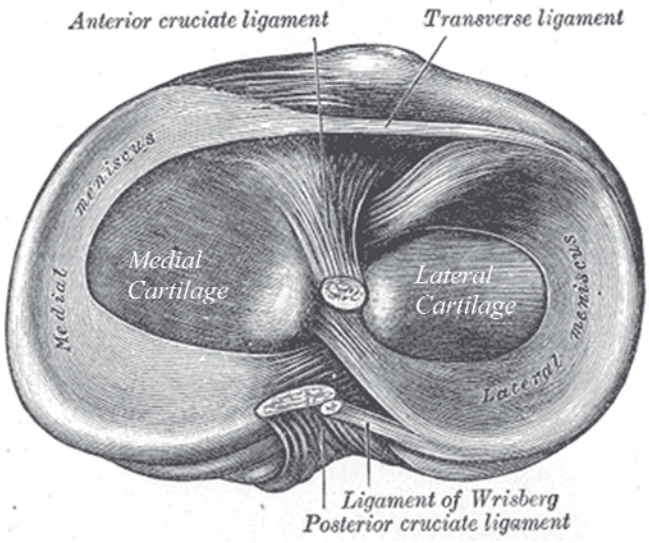

Figure 1-2. Axial view of structures of the proximal tibia, including medial and lateral menisci which overlie the medial and lateral articular cartilage. Note that the medial compartment is larger than the lateral compartment. Note also that the medial meniscus is more situated posteriorly while the lateral meniscus has equal portions both anteriorly and posteriorly. Modified from Gray's Anatomy [33].

1.2.3 Articular Cartilage

The joint surfaces of the proximal tibia, distal femur and posterior patella are covered with articular cartilage; a material which serves to transmit loads between bones and act as a low friction bearing material (Figure 1-3). Cartilage is an avascular material with a limited ability to repair and regenerate [41]. Articular cartilage is composed of an extracellular matrix (ECM) and chondrocytes (cartilage cells which maintain the ECM). It is a viscoelastic material, with water comprising between 68-85% of the total ECM volume [42]. The remaining volume is made up primarily of collagen type-II fibres (which resists tension and shear) and proteoglycans (which resist compression). Together these materials intertwine with one another to provide stiffness and resist deformation of the articular surface. Approximately 50% of the load on the proximal tibia is transmitted directly through the central areas of each compartment via cartilage-on-cartilage contact between the articulating femur and tibia [38-40].

1.2.4 Subchondral Bone

Directly inferior to the articular cartilage lie various layers of bony tissues, including:

- calcified cartilage; a thin partially mineralized tissue interconnected with subchondral cortical bone which begins at the tidemark (Figure 1-3)
- subchondral cortical bone (also known as subchondral plate or endplate), a thin highly mineralized layer of bone (Figure 1-3 & 1-4);
- subchondral trabecular bone, a spongy cancellous bone which is attached to and supports overlying subchondral cortical bone (Figure 1-3 & 1-4);
- epiphyseal trabecular bone at the proximal epiphysis [43] (Figure 1-3 & 1-4);
- metaphyseal trabecular bone at the proximal metaphysis [43] (Figure 1-4).

The term “subchondral bone” is used loosely to describe the subchondral bone structure, which includes subchondral cortical and subchondral trabecular bone. Subchondral bone functions as a supportive structure for the joint. Mechanically, subchondral bone acts in series with overlying cartilage to transfer energy between articulating bones. Kinetic energy of moving articulating bones is transferred to potential energy via bone and cartilage deflection. During dynamic impact loading, subchondral bone is the primary structure which deflects [44]. Subchondral bone deflection, subsequently, minimizes cartilage deflection and associated internal cartilage stresses.

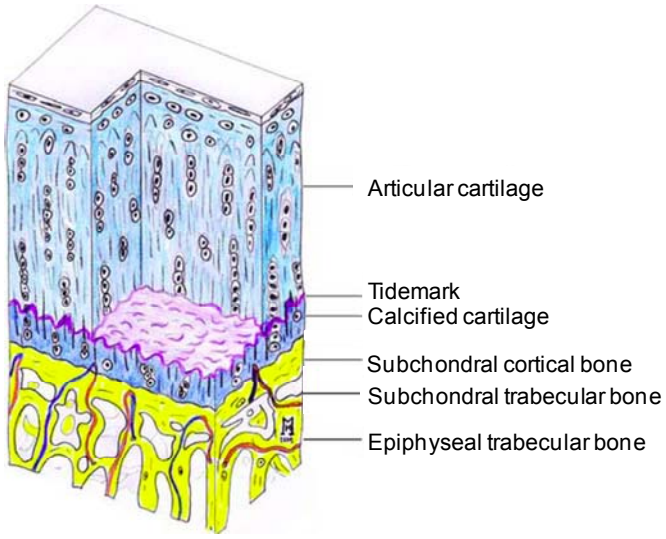

Figure 1-3. Schematic drawing of the different layers of the cartilage-subchondral bone complex, including articular cartilage, subchondral cortical, subchondral trabecular and epiphyseal trabecular bone. Modified from Imhof et al [43] and Madry et al [45], with permission from Springer.

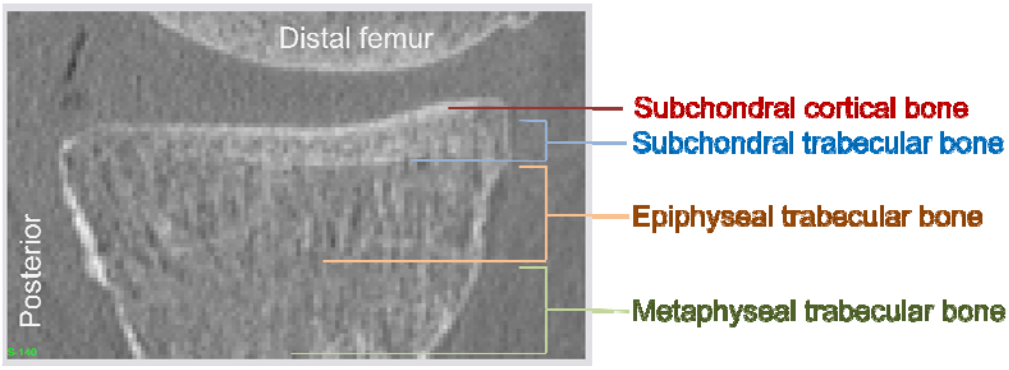

Figure 1-4. Sagittal computed tomography (CT) image of the proximal tibia and pertinent bony components, including subchondral cortical, subchondral trabecular, epiphyseal trabecular and metaphyseal trabecular bone. Neither cartilage nor the meniscus is observed in this image because neither tissue can absorb radiation.

1.3 Osteoarthritis

1.3.1 Disease Characteristics

OA is characterized by various clinical symptoms and morphological and biomechanical alterations. Clinically, OA is characterized by joint pain, swelling, stiffness and limited range of motion [46, 47]. Morphologically, OA is characterized by a loss of articular cartilage in normal weight bearing areas of a joint, subchondral bone sclerosis (bone hardening), subchondral cysts, osteophyte presence along the joint periphery, and synovial inflammation [46, 47] (Figures 1-5 & 1-6). Biomechanically, OA cartilage is characterized by altered mechanical properties (decreased tensile stiffness, decreased shear stiffness, decreased compressive stiffness), increased water content and excessive swelling [46, 47]. Subchondral bone was long thought to become stiffer than normal in joints with OA, but recent research at the knee and hip show conflicting findings [48-55] and increased stiffness may only occur at certain stages of OA disease progression.

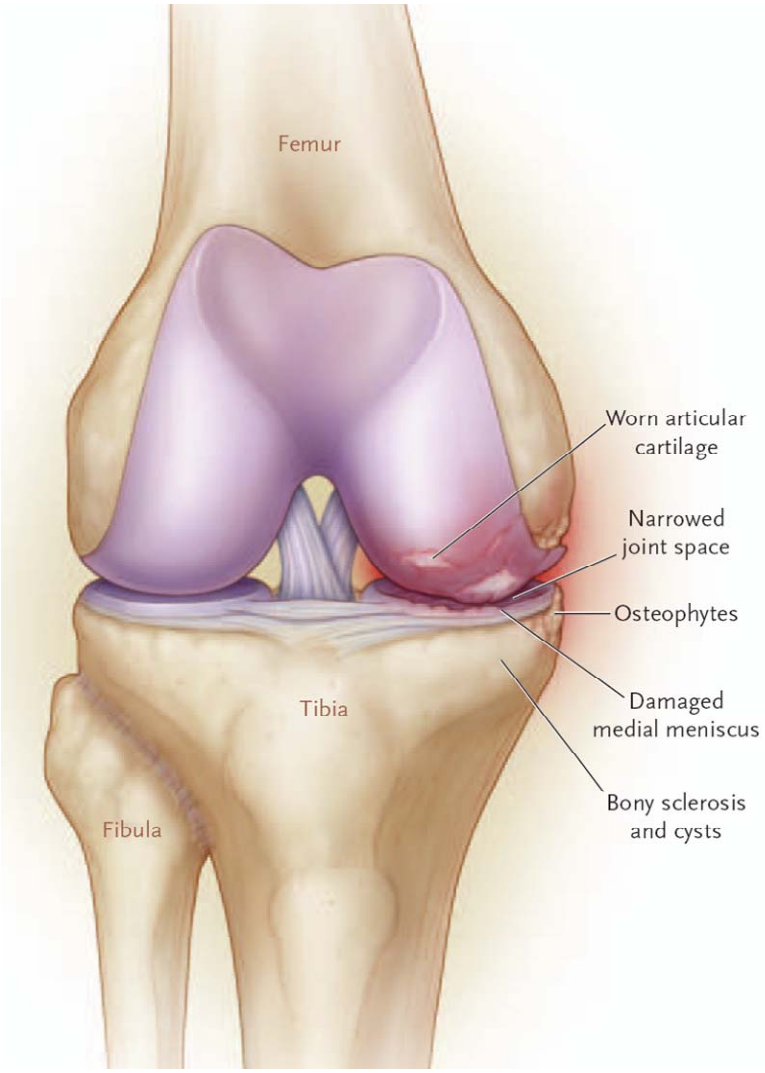

Figure 1-5. OA of the medial side of the knee. From Felson [56] with permission from the Massachusetts Medical Society.

Figure 1-6. Coronal CT images of normal (*A*) and OA (*B*) proximal tibiae. Sclerotic evidence and osteophyte presence is shown in the OA image (*B*).

1.3.2 Assessment Techniques

OA disease progression and severity is most commonly assessed using semi-quantitative evaluations of OA features visible in radiographic images (primarily osteophytes) or physical and visual evidence of articular cartilage degeneration. The Kellgren-Lawrence (KL) scoring system [57] is the most commonly used technique to assess radiographic OA severity (Table 1-1). The KL scoring system grades radiographic OA severity according to qualitative, subjective assessments of joint space narrowing, osteophyte presence and subchondral sclerosis observed in radiographic images. A KL score of 0 indicates no OA, 1-2 generally indicates early OA; and 3-4 indicates late OA.

Table 1-1. Kellgren Lawrence [57] grading of radiographic OA.

Grade	Property
0	Normal, no osteophytes
1	Possible osteophytic lipping
2	Definite osteophytes; possible joint space narrowing
3	Moderate or multiple osteophytes; definite joint space narrowing; some sclerosis and possible bony attrition
4	Large osteophytes; marked joint space narrowing; severe sclerosis and definite bony attrition

Other radiographic assessment techniques include estimates of cartilage thickness via joint space width (JSW): the measured distance between two articulating bones, and joint space narrowing (JSN): a reported change in JSW. The International Cartilage Repair Society (ICRS) system [58, 59] is a widely-used method to assess OA severity according to cartilage health, primarily the size and depth of lesions observed by arthroscopy or visual inspection (Table 1-2). The ICRS method involves both physical probing and visual assessment of the cartilage surface to find abnormalities in texture or hidden defects, and is closely correlated with histological gradings [60, 61]. The classification ranges from healthy cartilage (ICRS 0) to the absence of cartilage with exposed subchondral bone (ICRS 4).

Table 1-2. International Cartilage Repair Society (ICRS) grading [58] based on Outerbridge score [59].

Grade	Property
0	Normal cartilage
1	Superficial lesions, fissures and cracks; softening
2	Fraying and fissuring; lesions extending <50% cartilage depth; lesions <0.5" diameter
3	Fraying and fissuring; lesions extending >50% cartilage depth; lesions >0.5" diameter
4	Erosion of cartilage down to bone

1.3.3 Risk Factors

Initiation and progression of knee OA is linked to biomechanical factors such as obesity, joint injury, varus (bow-legged) and valgus (knock-kneed) mal-alignment [62]. Other factors linked to OA include age, sex, and—of particular interest for this work—bone density [62]. Various imaging studies have shown direct relationships between apparent bone mineral density (BMD), a measure of bone mass per unit volume (vBMD) or area (aBMD) [63], and OA. Importantly, apparent BMD is also commonly regarded as a surrogate measure of bone stiffness. A review paper [63] summarizing the results of 67 articles investigating links between BMD and OA revealed that 53 studies found BMD to be higher in OA, 13 showed no difference, and 1 study showed lower BMD. These studies have generally assessed whole body BMD or BMD at sites remote from the affected joint. Few studies have investigated direct relationships between joint-specific OA and adjacent BMD. Although higher than normal bone density appears to be associated with OA, the exact etiologic role played by bone in the degenerative process is unclear. Evidence from both human and animal studies, however, suggests that bone located nearest to the overlying articular cartilage may play a role in the initiation and/or progression of OA [13-19].

1.3.4 Etiopathogenesis

OA is generally considered to be a disease of articular cartilage with changes in the bone being secondary to damaged cartilage. The most prevalent and researched hypothesis regarding OA pathogenesis is that altered joint mechanics, impact loading, or repetitive loading at levels beyond normal physiologic ranges destroy cartilage chondrocytes and disrupt the ECM, resulting in proteoglycan depletion [64, 65]. Prolonged loading is anticipated to result in further cartilage breakdown and subsequent OA.

Alternatives to the "cartilage first" theory gaining support in the literature focus on bony changes preceding cartilage changes. The strongest evidence comes from a rabbit OA model in which high impact loads (≈12 BW) were applied to the patello-femoral joint using drop-tower impact testing [66]. A significant reduction in cartilage stiffness was not observed until 12 months post impact, even though there was a statistically significant increase in subchondral endplate thickness after 6 months.

The most often cited theory regarding the role of subchondral bone in OA, by Radin et al [4], proposes that OA subchondral bone is stiffer than normal which, for the same joint contact forces, predisposes the joint to progressive OA by increasing stresses within the overlying cartilage. This theory was based upon the observation of more subchondral trabecular bone microfractures in cadavers with early OA versus age-matched controls [67]. Similar observations were made in animals developing OA as a consequence of repetitive loading [3]. The same group also found that subchondral bone from joints with evidence of early OA had a reduced ability to transfer strain-energy generated during impact loading [67]. In this study the energy-transferring qualities of subchondral bone with different degrees of overlying cartilage degeneration were determined using drop tower impact testing and energy methods. Strain energy (area under load-displacement curve) was approximated using half the product of peak dynamic force and deflection at time of peak dynamic force (Figure 1-7).

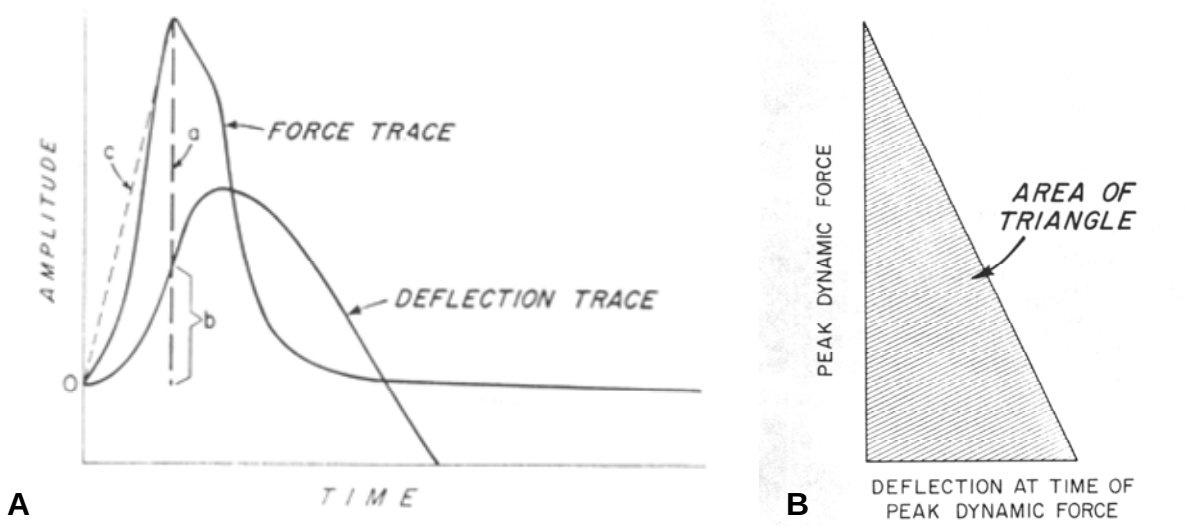

Figure 1-7. *A,* The use of force and deflection data to approximate the relative strain energy transferred by subchondral bone plugs at the time peak dynamic force is attained. Line a represents peak dynamic force; part b of that line represents deflection at that time. *B,* The approximation of energy generated and transferred by the specimens is the area of a triangle formed by using lines a and b from *A*. Modified from Radin et al [67], with permission from Wiley.

Early OA subchondral bone plugs subjected to 1.5 kg drop tests from 3.2 and 6.4 mm heights showed reduced strain energies of -64% when compared with normal subchondral bone [67]. The diminished ability of early OA subchondral bone to transfer strain energy means that more energy must be transferred by the remaining parts of the skeletal system, particularly overlying articular cartilage. Altered stiffness and absorption qualities were speculated to be due to trabecular microfractures generated during high impact loading and cumulative damage, which would be repaired and strengthened by fracture callus [2, 3]. As the trabeculae became thicker and new trabeculae were added, the repair process would stiffen subchondral bone, in effect acting as a support for the overlying subchondral cortical bone. A stiffened subchondral bone will be less able to deform under dynamic impact loading (i.e., transfer strain energy), leading to more energy being transferred through the overlying cartilage for the same contact loads. This would lead to higher internal cartilage stresses, cartilage breakdown, and eventual OA [2-4]. This theory was supported by a finite element study which

showed that increased stiffness of subchondral cortical or trabecular bone within 1-2 mm of the subchondral surface would increase cartilage stresses by ~50% in the deepest layers [19].

A second (more recent) hypothesis regarding the role of subchondral bone relates to increased biological activity, resulting in subchondral cortical bone thickening and decreased cartilage thickness leading to increased cartilage stresses and eventual OA [68]. Microfractures within subchondral cortical bone resulting from impulse loading and repetitive stress are hypothesized to increase biological activity at the site of injury and result in increased bone turnover [68]. Increased bone turnover should result in thicker subchondral cortical bone since reactivation advances the tidemark towards the cartilage surface, resulting in thinner cartilage. Thicker subchondral cortical bone and thinner articular cartilage would also result in increased cartilage stresses and eventual loss of cartilage leading to OA. Evidence supporting the role of increased bone turnover includes the increased presence of biochemical markers of bone formation and resorption in OA patients [69-71].

Although the exact role of subchondral bone in OA is unknown, bony changes nearest the joint surface appear to be involved in the initiation, progression and/or acceleration of OA.

1.4 Osteoarthritic Subchondral Bone

This review focuses on OA-related changes in morphometry, density and mechanical properties of human proximal tibial subchondral bone. When applicable, studies of proximal femora which have produced key findings in the present knowledge of OA subchondral bone changes are also included.

Bone morphometry and density are typically investigated using measures which assess the mineral density of the bone tissue itself, the quantity of bone within a fixed volume, and the mass of bone mineral within a fixed volume. These measures include material density (bone mass / bone volume), bone volume fraction (bone volume / total volume), and apparent density (bone mass / total volume). Apparent density is equal to material density multiplied by bone volume fraction. Bone

morphometry and density measure are generally regarded as surrogate estimates of bone stiffness since more bone should, at least logically, equate with stiffer bone. Mechanically, bone is traditionally investigated using assessments of material stiffness (slope of stress-strain curve, referred as Young's modulus or modulus of elasticity E) or structural stiffness (slope of load-displacement curve, N/mm). Material stiffness describes the intrinsic material properties of bone itself and is independent of specimen geometry or size. Structural stiffness is an assessment of a bone specimen's response to deflection and is dependent upon both material stiffness properties and physical size of the bone tissue being tested.

1.4.1 *Ex Vivo* Research

1.4.1.1 Morphology

Subchondral cortical bone from normal and OA proximal tibiae varies in thickness from 0.8 to 3.3 mm at the joint centers [16, 23, 72] and 0.01 to 0.3 along the periphery [23, 72] (Table 1-3). The greatest thicknesses are observed at the centers of the medial and lateral regions, corresponding to sites that experience high load [72]. The medial compartment typically has greater cortical bone thickness than the lateral [72].

Subchondral cortical bone is thicker in joints with OA than in normal joints [48, 73, 74]. At the proximal tibia, there have only been two studies comparing OA and normal subchondral cortical bone thickness [16, 73] (Table 1-3). One study showed 43% thicker subchondral cortical bone with early OA and ~2x thicker subchondral cortical bone with late OA [73]. The second study showed similar thicknesses beneath cartilage exhibiting varying degrees of degeneration [16].

Table 1-3. Compilation of proximal tibial and femoral studies comparing subchondral cortical thickness of OA and normal tissue.

Author	Bone region	Study type	Study method	# Specimens			Location / Category	Sex	Subchondral Cortical Thickness (mm) Mean ± SD or Median [95% C.I.]				OA findings	Comments
				Normal	£OA	Pooled			Normal	Early OA	Late OA	Pooled		
Clark & Huber (1990)	Proximal tibia	Ex Vivo	Histology			20	Central Periphery					< 3 > 0.01	Bone as thin as 0.01 except central thickness < 3 mm	No standard deviations, only minimum/maximum
Milz & Putz (1994)	Proximal tibia	Ex Vivo	Histology			24	Central Periphery Medial Lateral					0.8-1.5 0.1-0.3 0.02-2.1 0.04-1.4	•Central thickness generally ranged 0.8-1.5mm •Medial compartment thicker than lateral	No standard deviations, only ranges provided
Yamada et al (2002)	Proximal tibia	Ex Vivo	Histology Radiography			140	Medial Lateral		3.5 [2.4-4.8] 3.0 [1.1-4.2]	3.5 [1.6-5.0] 2.9 [1.5-4.9]	2.9 [1.3-4.8] 2.3 [1.3-4.8]		•Nonsignificant trend for lower thickness with OA •Medial compartment thicker than lateral •Medial compartment thicker in males than females	•Thickness from x-ray images of 10mm thick sections of bone •OA definition: Normal: Intact surface Early OA: Minimal fibrillation Late OA: Overt fibrillation, erosion
							Medial Lateral Medial Lateral	M F 				3.3 ± 1.3 2.7 ± 1.2 2.7 ± 1.1 2.5 ± 1.0		
Buckland-Wright (2004)	Proximal tibia	Ex Vivo	Radiography	28	36/15				0.37 ± 0.06	*0.53 ± 0.11	*0.76 ± 0.16		Thicker subchondral cortical bone with early and late OA	Early OA: Joint space width > 3 mm Late OA: Joint space width < 1.5 mm

£ OA population is either solely Early OA or Late OA, or a combination of the two (Early OA / Late OA)

* $p < 0.05$, statistically significant difference between normal and OA samples

Table 1-4. Compilation of *ex vivo* proximal tibial studies comparing subchondral bone volume fraction (%) in OA and normal tissue. Studies are listed in order of proximity to the subchondral bone surface.

Author	Study type	Study method	# Specimens Normal	# Specimens £OA	φBone type	~Distance from surface	Location / Category	‡ Bone Volume Fraction (%) Mean ± SD or [95% confidence interval] Normal	Early OA	Late OA	OA findings	Comments
Matsui et al (1994)	Ex Vivo	Histology		11	SubC & SubT	0-2 mm		30	*51	*48	•Higher bone volume beneath damaged cartilage regions •Medial compartment bone changes focused across 1.5 mm from surface •Lateral compartment bone changes focused across 0.5 mm from surface	•OA tissue obtained from knee arthropasty patients •OA categorization defined using Mankin scorings of histological sections whereby Normal = Mankin 0-6 Early OA = Mankin 7-9 Late OA = Mankin 10-14
						0-0.5 mm	Medial			86		
						0.5-1 mm				77		
						1-1.5 mm				70		
						1.5-2 mm				60		
						0-0.5 mm	Lateral			64		
						0.5-1 mm				36		
						1-1.5 mm				27		
						1.5-2 mm				25		
Bobinac et al (2003)	Ex Vivo	Histology	10	10	SubC & SubT	0-0.5 mm		56 ± 12	*69 ± 13	*72 ± 13	•Higher bone volume found in OA knees •Higher bone volume beneath degenerated cartilage regions	OA categorization defined using Mankin scorings in same manner as Matsui et al (1994)
						0.5-1 mm		31 ± 8	*50 ± 11	*54 ± 12		
						1-1.5 mm		28 ± 7	34 ± 10	*47 ± 14		
						1.5-2 mm		27 ± 6	32 ± 8	*39 ± 12		
						0-2 mm	Medial	37 ± 9		63 ± 13		
						0-2 mm	Lateral	38 ± 9		45 ± 10		
Kambiyashi et al (1995)	Ex Vivo	Histology	11	4	SubC & SubT	0-1 mm	Medial	39 ± 6		*66 ± 10	•Higher bone volume with OA •Highest bone volume nearest the joint surface	OA tissue obtained from knee arthroplasty patients
						1-3 mm	Medial	28 ± 6		*54 ± 10		
						3-5 mm	Medial	22 ± 6		*42 ± 10		
Ding et al (2001)	Ex Vivo	Histology	10	10	SubT & Epi	2-5-10 mm	Medial	20 [18-23]	*24 [22-26]		Higher bone volume beneath degenerated cartilage regions	Normal = Mankin 0-2 Early OA = Mankin 1.5-7
							Lateral	16 [14-18]	*18 [15-20]			
Day et al (2001)	Ex Vivo	Histology	10	10	SubT & Epi	2-5-10 mm	Medial	22 ± 6	25 ± 4		No difference in bone volume between normal and Early OA	Normal = Mankin 0-2 Early OA = Mankin 1.5-7
							Lateral	18 ± 3	20 ± 6			
Christensen et al (1982)	Ex Vivo	Histology		11	Epi	5-25 mm	Medial			9-19	•Varus: higher BV medially •Valgus: higher BV laterally	Range of bone volumes for varus and valgus knees
							Lateral			10-20		

£ OA population is either solely Early OA or Late OA, or a combination of the two (Early OA / Late OA)

φ Bone types include subchondral cortical bone (SbT), subchondral trabecular bone (SbT) and epiphyseal trabecular bone (Epi)

‡ Bone volume fraction (bone volume / total specimen volume)

* $p < 0.05$, statistically significant difference between normal and OA samples

Bone volume fraction (bone volume / total specimen volume) near the subchondral bone surface is higher than normal in OA proximal tibiae [14, 15, 75] (Table 1-4). These measures—which essentially combine subchondral cortical bone thickness and the quantity of subchondral trabecular bone located within 0-5 mm of the subchondral surface—are 19-70% higher than normal with early-OA [14, 15] and 29-93% higher with late-OA [14, 15, 75]. Higher than normal bone volume fractions has been largely attributed to increased thickness of individual trabeculae [14, 15, 75]. Near the subchondral surface the thickness of normal trabeculae range between 0.15 and 0.18 mm [14, 15, 75]. In OA the thicknesses range between 0.19 and 0.33 mm [14, 15, 75].

1.4.1.2 Material Density

While OA subchondral bone appears sclerotic on x-ray, OA subchondral cortical and trabecular bone is actually hypomineralized relative to normal bone. The material density (bone mass / bone volume) of subchondral cortical, subchondral trabecular and epiphyseal trabecular bone is lower in OA subjects [48, 49, 74, 76] (Table 1-5). This is due to OA bone having a higher than normal bone turnover rate [71], resulting in younger, less highly mineralized bone and greater amounts of osteoid [18, 74, 77]. At the hip, recent studies have shown late OA subchondral bone to have material densities 6-8% lower than normal values (Figure 1-8) [48, 49, 76]. At the proximal tibia, only one study has directly assessed material density and this study showed no material density differences between normal and early OA subchondral bone [54]. However, one study assessing the ash content (ash mass / bone volume)—a measure comparable to material density—of proximal tibial subchondral trabecular bone has shown 11% lower than normal values in late OA [50].

Table 1-5. Compilation of *ex vivo* proximal tibial and femoral studies comparing subchondral material density in OA and normal tissue. Studies are listed by proximity to the subchondral bone surface with proximal tibial studies listed first.

Author	Bone region	Study type	Study method	# Specimens		φBone type	~Distance from surface	Location / Category	‡ Material Density (g/cm^3) Mean ± SD or Median [95% C.I.]			Findings	Comments
				Normal	£OA				Normal	Early OA	Late OA		
†Zysset et al (1994)	Proximal tibia	Ex Vivo	Ashing		6	SubT	2.5-5.5 mm	Medial Lateral	1.20 ± 0.05 1.15 ± 0.15	1.12 ± 0.08 1.07 ± 0.06	*1.07 ± 0.17 1.25 ± 0.08	Lower medial ash content with Late OA	Limited sample size (6 knees from four cadavers)
Ding et al (2001)	Proximal tibia	Ex Vivo	Archimedes	10	10	SubT & Epi	2.5-10 mm	Medial Lateral	2.21 [2.20-2.22] 2.19 [2.16-2.22]	2.23 [2.22-2.24] 2.23 [2.22-2.24]		No difference in material density with Early OA	Reported Mean [95% C.I.]
Li & Aspden (1997)	Femoral head	Ex Vivo	Archimedes	7	16	SubC	0-1 mm		1.79 ± 0.08		*1.69 ± 0.13	Lower material density with OA	OA tissue from arthroplasty
Chappard et al (2006)	Femoral head	Ex Vivo	Synchrotron Imaging		6	SubC, SubT & Epi	0-10 mm			0.87 ± 0.16	*0.82 ± 0.14	Lower material density with Late OA vs Early OA	Early OA is arthroplasty tissue w/ cartilage, Late OA w/o
Li & Aspden (1997)	Femoral head	Ex Vivo	Archimedes	7	16	SubT & Epi	2.5-10 mm		1.89 [1.80-1.96]		*1.73 [1.53-1.86]	Lower material density with OA	Lower density near surface, middle of head & neck
Brown et al (2002)	Femoral head	Ex Vivo	Archimedes	11	21	SubT & Epi	2.5-15 mm	Superior Inferior	1.66 (1.36-1.89) 1.77 (1.30-2.00)		1.68 (1.47-1.90) 1.78 (1.57-1.97)	No material density differences with OA	Report Medial (Range)
Grynpas et al (1991)	Femoral head	Ex Vivo	Fractionation	13	12	SubC, SubT & Epi SubC, SubT & Epi Epi Epi	0-10 mm 0-10 mm 20-40 mm 20-40 mm	> 2.1 g/cm^3 < 2.0 g/cm^3 > 2.1 g/cm^3 < 2.0 g/cm^3	33% 18% 34% 16%		*3% *55% *24% *40%	Late OA bone has smaller % of high density bone and larger % of low density bone	Coarse method of subdividing bone tissue mineralization into fractions (<1.9, 1.9-2, 2-2.1, >2.1 g/cm^3)

£ OA population is either solely Early OA or Late OA, or a combination of the two (Early OA / Late OA)

φ Bone types include subchondral cortical bone (SbT), subchondral trabecular bone (SbT) and epiphyseal trabecular bone (Epi)

‡ Material density (bone weight / bone volume) (g/cm^3)

† Ash content (ash weight / bone volume) (g/cm^3)

* $p < 0.05$, statistically significant difference between normal and OA or between Early OA and Late OA

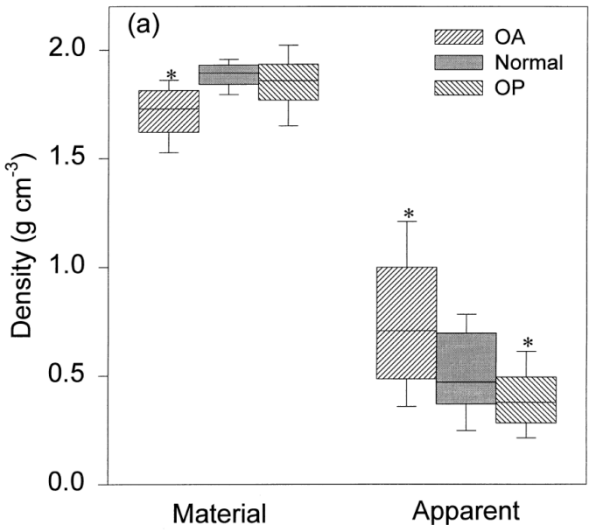

Figure 1-8. The material density (bone mass / bone volume) of bone in OA is significantly less than normal, but the apparent density (bone mass / total volume) is significantly greater. Reproduced from Li and Aspden [49] with permission from the American Society for Bone and Mineral Research.

1.4.1.3 Apparent Density

Laboratory-based measures of volumetric apparent density (bone mass / total volume) from OA joints are generally higher than normal at both the hip and knee [49, 54, 78] (Table 1-6, Figure 1-8). Recalling that apparent density is equal to material density multiplied by bone volume fraction; apparent density will increase in response to either an increase in mineralization of the tissue or an increase in bone volume. Although material density seems to decrease with OA (see previous section), increases in bone volume near the subchondral surface (0-5 mm) appear to offset such material density reductions, leading to higher than normal measures of apparent density. At the hip, apparent density of OA subchondral bone has been found to be 48% [78] and 51% [49] higher than normal (Figure 1-8). At the proximal tibia, early OA subchondral bone has 21% higher apparent density than normal [54]. However, late OA subchondral trabecular bone has apparent density that is 45% lower than normal, although the sample population for this study was very small (6 knees from 4 cadavers) [50].

Table 1-6. Compilation of *ex vivo* proximal tibial and femoral studies comparing subchondral apparent density in OA and normal tissue. Studies are listed by proximity to the subchondral bone surface with proximal tibial studies listed first.

Author	Bone region	Study type	Study method	Ω Density type	# Specimens Normal	# Specimens £OA	φ Bone type	~Distance from surface	Location / Category	Sex	3D Volumetric Apparent Density (g/cm^3) Mean ± SD or Median [95% C.I.] Normal	Early OA	Late OA	OA comparison with normal findings	Comments
Zysset et al (1994)	Proximal tibia	Ex Vivo	Lab	ρ_{app}		6	SubT	2-5 mm	Medial		0.32 ± 0.14	0.33 ± 0.13	0.33 ± 0.15	•Lower lateral apparent density with Late OA	Limited sample size (6 knees from four cadavers)
									Lateral		0.33 ± 0.14	0.32 ± 0.12	*0.18 ± 0.06		
							Epi	7-13 mm	Medial		0.17 ± 0.06	0.17 ± 0.05	0.18 ± 0.04	•Similar density at distal sites	
									Lateral		0.17 ± 0.06	0.17 ± 0.05	0.18 ± 0.03		
Ding et al (2001)	Proximal tibia	Ex Vivo	Lab	ρ_{app}	10	10	SubT & Epi	2.5-10 mm	Medial		0.43 [0.37-0.49]	*0.52 [0.47-0.57]		Higher medial apparent density with Early OA	Reported Mean [95% C.I.]
									Lateral		0.35 [0.30-0.40]	0.39 [0.35-0.42]			
Li & Aspden (1997)	Femoral head	Ex Vivo	Lab	ρ_{app}	7	16	SubT & Epi	2.5-10 mm			0.47 [0.25-0.78]		*0.71 [0.35-1.21]	Higher apparent density with OA	Entire femoral head and neck had higher density with OA
Brown et al (2002)	Femoral head	Ex Vivo	Lab	ρ_{app}	11	21	SubT & Epi	2.5-15 mm	Superior		0.62 (0.30-1.00)		0.73 (0.44-1.07)	Higher apprent density in unloaded, inferior region	No standard deviations, only ranges provided
									Inferior		0.29 (0.20-0.57)		*0.43 (0.27-0.75)		

Ω Density types include:

ρ_{app} - apparent density or *wet* apparent density (hydrated bone mass / total specimen volume)

£ OA population is either solely Early OA or Late OA, or a combination of the two (Early OA / Late OA)

φ Bone types include subchondral cortical bone (SbT), subchondral trabecular bone (SbT) and epiphyseal trabecular bone (Epi)

* $p < 0.05$, statistically significant difference between normal and OA or between Early OA and Late OA

1.4.1.4 Mechanical Properties

No studies have investigated the structural stiffness of proximal tibial subchondral bone directly at the subchondral bone surface; a measure which reflects bone's response to articular cartilage loading and is most relevant in studies of OA progression. Most studies of OA and normal proximal tibiae have assessed the material stiffness of epiphyseal and metaphyseal trabecular bone [52-54, 79-89] while only a few have assessed the subchondral trabecular region [50, 51, 55] (Tables 1-8). The few proximal tibial studies which focused on mechanical properties directly at the subchondral surface were limited to assessments of ultimate bone strength [90-92], not stiffness. These studies found that in the normal knee, ultimate strength decreases rapidly with distance from the surface [90-92], especially over the first 5 mm [90] (Figure 1-9). Although the focus of this review is on stiffness (since subchondral bone stiffness is believed to be linked to OA), the rapid change with depth of these ultimate strength findings highlights the importance of assessing bone properties nearest the subchondral surface.

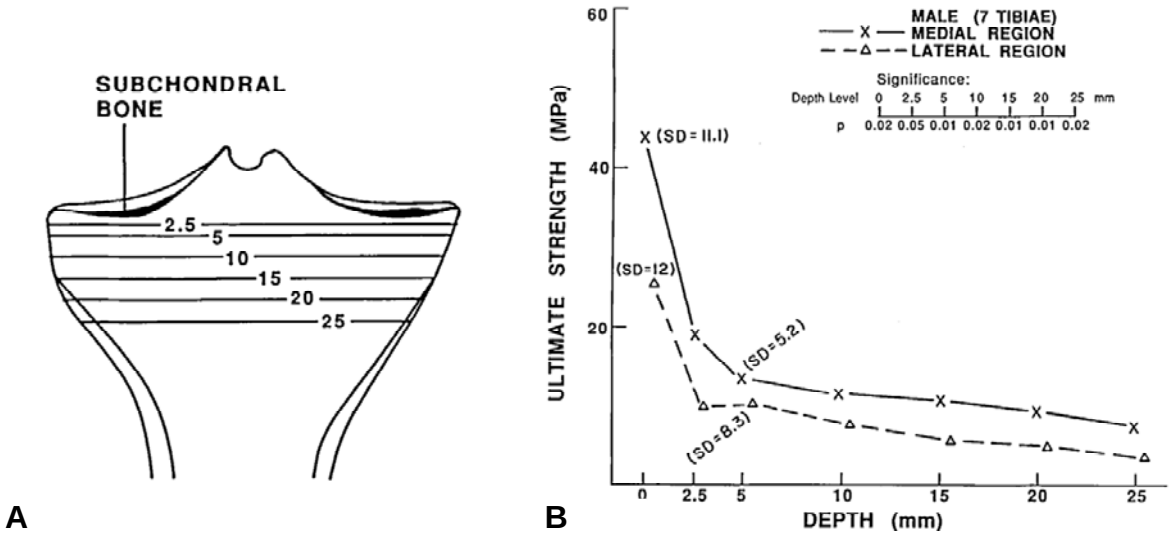

Figure 1-9. *A,* Indentation test sites in the transverse plane below the lowest part of the subchondral bone surface. *B,* Relationship between ultimate bone strength and depth below the surface of the subchondral bone. From Harada et al [90] with permission from Elsevier.

Table 1-7. Compilation of studies assessing the material stiffness (modulus of elasticity E) of normal proximal tibiae. Studies are listed in order of proximity to subchondral bone surface and/or specimen size. If the location is not known, the study is listed last. If the distances from the surface are similar, the studies are listed in chronological order. Studies are listed by proximity to the subchondral bone surface.

Author	Study type	ψStudy method	Joint status	# Bones	# Tests	φBone type	~Distance from surface	Modulus range (MPa)	Comments
Choi et al (1990)	Ex Vivo	3-Point Bending	Normal	1	20	SubC	0-1 mm	600-1900	
Bentzen et al (1987)	Ex Vivo	Platen	Normal	3	165	SubT & Epi	2-10, 10-18, 18-26 mm	6-1670	
Hvid et al (1989)	Ex Vivo	Platen	Normal	10	250	Epi	5-12.5, 12.5-20 mm	60-1250	
Linde et al (1989)	Ex Vivo	Platen	Normal	5	33	Epi	5-12.5, 12.5-20 mm	105-942	
Linde et al (1990)	Ex Vivo	Platen	Normal	5	119	Epi	5-12.5, 12.5-20 mm	67-734	
Linde et al (1991)	Ex Vivo	Platen	Normal	1	60	Epi	5-12.5, 12.5-20 mm	90-1000	Assume distance from surface based upon related research
Odgaard et al (1991)	Ex Vivo	Platen	Normal	1	18	Epi	5-12.5, 12.5-20 mm	108-1637	
Linde et al (1992)	Ex Vivo	Platen	Normal	4	31	Epi	5-12.5, 12.5-20 mm	€0-679	4 knees from 2 subjects
Williams & Lewis (1982)	Ex Vivo	Platen	Normal	1	21	Epi	5-10, 11-17, 18-24, 25-30 mm	8-457	
Lindahl (1976)	Ex Vivo	Platen	Normal	60	64	Epi	5-15,15-25,25-35,35-45 mm	1-79	
Goldstein et al (1983)	Ex Vivo	Platen	Normal	5	~150	Epi	5-15,15-25,25-35,35-45 mm	4-433	Report range for 1 example tibia exhibiting largest variance
Anderson et al (1992)	Ex Vivo	Platen	Normal	4	30	Epi	10-30 mm	32-1066	•4 knees from 2 subjects •E range from Appendix
Morgan et al (2003)	Ex Vivo	End-caps	Normal	15	15	Epi	8-32 mm	10-2770	
Keyak et al (1994)	Ex Vivo	Platen	Normal	4	36	Epi	5-29, 30-54, 55-79 mm	36-2767	4 knees from 2 subjects
Carter & Hayes (1977)	Ex Vivo	Confined compression	Normal		100			20-200	Specimen site / location unknown

ψ Study methods include:
3-Point Bending - Excised slab of bone tested in bending. Specimen is not fixed to testing apparatus.
Platen Compression - Excised bone cubes or cores compressed between two platen surfaces. Specimens are not fixed to testing apparatus.
End-caps - The test ends of the specimens are fixed to the mechanical testing apparatus
Confined Compression - Excised bone cubes pressed into cylinder, then compressed

φ Bone types include subchondral cortical bone (SbT), subchondral trabecular bone (SbT) and epiphyseal trabecular bone (Epi)

€ Range represents 95% confidence interval, either provided or established using Mean ± 1.96·SD

Table 1-8. Compilation of proximal tibial and proximal femoral studies comparing material stiffness (E) or hardness (HB) of OA and normal tissue.

Author	Bone region	Study type	ΨStudy method	# Specimens		φBone type	~Distance from surface	Location / Category	Elastic Modulus (MPa) or †Hardness (HB) Mean ± SD or Median [95% C.I.]			OA comparison with normal findings	Comments
				Normal	£OA				Normal	Early OA	Late OA		
Finlay et al (1988)	Proximal tibia	In Situ	Indent Inverse	15	13	SubT	2.5-0	M - Ant	375 ± 126		397 ± 133	•Similar stiffnesses •Higher M/L stiffness ratio with OA	•Tested upside-down •Only include Medial OA •4 mm diameter indentor •Poisson's ratio 0.2 with Timoshenko-Goodier (1970)
								M - Pos	318 ± 91		316 ± 120		
								L Ant	263 ± 101		178 ± 114		
								L Pos	279 ± 115		190 ± 138		
								M/L	1.31 ± 0.25		*2.21 ± 0.81		
Zysset et al (1994)	Proximal tibia	Ex Vivo	Platen		6	SubT	2-5 mm	Medial	434 ± 257	421 ± 286	*179 ± 104	•Lower elastic modulus with Late OA •Similar elastic modulus at distal sites	Limited sample size (6 knees from four cadavers)
								Lateral	421 ± 286	303 ± 143	*131 ± 67		
						Epi	7-13 mm	Medial	505 ± 320	581 ± 316	474 ± 223		
								Lateral	472 ± 274	411 ± 189	467 ± 154		
Ding et al (1998)	Proximal tibia	Ex Vivo	Platen Inverse	10	9	SubT	8.5-0 mm	Medial	311 (53-887)	237 (53-646)		Similar stiffness with Early OA	•Reported Mean (Range) •Tested upside-down
								Lateral	292 (30-723)	218 (23-608)			
Ding et al (2001)	Proximal tibia	Ex Vivo	Platen	10	10	SubT & Epi	2.5-10 mm	Medial	475 [257-693]	275 [211-339]		Similar stiffness with Early OA	•Reported Mean [95% C.I.] •Large stiffness variation
								Lateral	275 [208-386]	293 [187-401]			
Day et al (2001)	Proximal tibia	Ex Vivo	Platen	10	10	SubT & Epi	2.5-10 mm	Medial	610 ± 450	370 ± 220		Similar stiffness with Early OA	Large stiffness variation
								Lateral	400 ± 120	390 ± 260			
†Lereim et al (1974)	Proximal tibia	In Situ	Hardness	19	21	SubT	2.5		7.6 ± 2.3		*3.9 ± 2.5	Lower hardness with OA	Removed subchondral cortical bone prior to testing.
Li & Aspden (1997)	Femoral head	Ex Vivo	Ultra-sound	7	16	SubC	0-1 mm		19.8 [13.5-20.0]		*17.0 [8.3-18.5]	Lower stiffness with Late OA	Expressed as GPa
Li & Aspden (1997)	Femoral head	Ex Vivo	Platen	7	16	SubT & Epi	2.5-10 mm		310 [41-460]		*356 [118-551]	Higher stiffness with Late OA	Entire femoral head and neck had higher stiffness with OA

Ψ Study methods include:
Indentation - Use of a flat indentor for compressive indentation testing. The Timoshenko-Goodier (1970) equation is used to obtain an elastic modulus from stiffness.
Platen Compression - Excised bone cubes or cores compressed between two platen surfaces.
Hardness - Micro hardness testing using the Brinell Method (1900).
Inverse Compression - In such scenarios, the specimen is flipped and compression occurs from a trabecular site towards the subchondral surface.

£ OA population is either solely Early OA or Late OA, or a combination of the two (Early OA / Late OA)

φ Bone types include subchondral cortical bone (SbT), subchondral trabecular bone (SbT) and epiphyseal trabecular bone (Epi)

* $p < 0.05$, statistically significant difference between normal and OA or between Early OA and Late OA

Although OA subchondral bone is generally thought to be highly stiff (i.e., sclerosis = hardened) the material stiffness of OA proximal tibial bone has been found in one study to be lower [50] and in others to be similar [50, 52-55] to normal subchondral bone (Table 1-8). The most intriguing research relating OA and normal material properties has been conducted at the hip [48, 49]. Subchondral cortical bone from late OA hips had 14% lower material stiffness than subchondral bone from normal hips [48]. Subchondral trabecular bone located immediately below the previously assessed subchondral cortical bone from late OA hips had 15% higher material stiffness than normal. The authors proposed that subchondral trabecular bone was more stiff than normal because more trabecular bone was present with OA (higher apparent density) [49]. They also hypothesized that although OA subchondral cortical bone has a lower than normal material stiffness, such deficiencies would be offset by greater amounts of bone (i.e., thicker subchondral cortical bone [48]). The combined effects of a thicker—though slightly weakened—cortical bone with stiffer underlying subchondral trabecular bone may therefore result in an overall *structural* stiffness exceeding normal values [48]. These studies highlight the importance of measuring the structural stiffness of subchondral bone directly at the subchondral bone surface since OA-related changes to both subchondral cortical and subchondral trabecular bone may contribute to the overall stiffness of subchondral bone. This is important because it is the overall structural stiffness which will have the greatest influence on overlying cartilage integrity.

1.4.1.5 Critique of *Ex Vivo* Research

Ex vivo research studies suggest that subchondral bone nearest the subchondral surface is most affected by OA. Comparisons of OA and normal proximal tibiae show OA cortical bone to be thicker than normal [73] while OA subchondral trabecular bone located less than 5 mm from the subchondral surface has higher than normal bone volume fractions [14, 15, 75]. OA-related reductions in material density [50] appear to be offset by these increased bone properties, leading to higher than normal measures of apparent density [54]. Subchondral cortical and subchondral trabecular bone located nearest the subchondral bone surface (< 5 mm) also appear to be the primary constituents comprising the structural stiffness of subchondral bone [90-92].

Our current understanding of OA-related subchondral bone changes, particularly early changes, is largely incomplete due to analyses of cadaver specimens with unknown medical histories or late OA tissue obtained after arthroplasty surgery. There is uncertainty regarding the validity of OA and normal comparison studies given that that the clinical OA status or pain symptoms with cadaver specimens is generally unknown. Our understanding of early OA bone changes is limited to only a few studies with small sample populations, likely due to difficulties in obtaining applicable human tissue. Late OA subchondral bone changes may also differ from early OA changes. Current hypotheses regarding the mechanical role of subchondral bone in OA are also largely based upon animal studies. However, animal studies of OA initiation and progression may not be applicable to the human OA process. In order to better understand the role of subchondral bone in OA, there is a need to monitor subchondral bone properties in people living with OA, particularly at early stages of the disease. There is also a need to monitor OA-related subchondral bone changes longitudinally to study OA prevention and treatment strategies.

1.4.2 *In Vivo* Research

Non-invasive *in vivo* imaging methods previously used to assess OA proximal tibial subchondral bone properties—listed in order of frequency of usage—include ‡dual-energy x-ray absorptiometry (DXA) [10, 12, 21-27], fractal signature analysis (FSA) [27, 73, 93-95], magnetic resonance imaging (MRI) [96-99], and peripheral quantitative computed tomography (pQCT) [28]. These methods have been used to assess bone properties such as bone volume fraction and volumetric BMD—a measure comparable with laboratory-based apparent density—in people living with OA. However, each imaging method has particular limitations which may hinder characterizations of subchondral bone properties nearest the subchondral bone surface. *In vivo* measures of bone properties, like laboratory-based measures of bone morphometry and apparent density, are also generally regarded as surrogate measures of bone stiffness.

In regards to strengths and limitations of different imaging methods, spatial resolution—the size of the smallest possible feature that can be detected—is typically represented by a point spread function (PSF) for each imaging system. The PSF describes the response of an imaging system to a small point object (e.g., small bead), with the spread of the point object in the image characterizing the PSF. For most medical imaging research, voxel size is commonly used to indicate differences in spatial resolutions between different imaging methods, with the assumption that the voxel size is greater than the PSF. It is important to note that voxel size is not equivalent with PSF. However, for this work, the term voxel size will be used to indicate better spatial resolutions for different types of imaging modalities.

‡ Dual-photon absorptiometry (DPA) was the natural precursor to dual-energy x-ray absorptiometry (DXA). One of the aforementioned DXA studies is a DPA study [12]. Due to similarities between the two methods, DPA and DXA are generally regarded as synonymous methods and commonly referenced using the term DXA.

1.4.2.1 Dual-Energy X-ray Absorptiometry (DXA or DEXA)

To date, most studies linking knee OA with imaged bone properties have been conducted using DXA [10, 12, 21-27]. DXA is a 2D projection-based imaging tool which uses radiographic absorption techniques to measure the amount of bone found within a specified 2D area or region of interest (ROI); expressed as bone mineral content (BMC). By dividing BMC by the specified 2D area, measures of apparent density in the form of areal BMD (aBMD, mg/cm^2) can be obtained. DXA represents a 3D structure as a 2D projection and is therefore very sensitive to subject size because larger individuals will contain more bone mineral within a specified 2D area. Further, aBMD measures are sensitive to patient positioning (i.e.,misalignment will alter BMC measures within a fixed ROI) and DXA is limited to imaging in the sagittal and coronal planes. Due to the planar nature of DXA the tool is unable to distinguish subchondral cortical from trabecular bone, particularly near the curved subchondral bone surface, and it cannot characterize the density of a complex 3D region of interest

Due to an inability to separate subchondral cortical from trabecular bone, combined with size-related imaging artifacts, DXA is ill suited for studying subchondral bone changes in OA. The few studies which compared proximal tibial aBMD from OA and normal knees offered conflicting results, with reports of no difference [11, 27], 8-10% lower [12, 22], and 15-26% higher [12, 24] aBMD in the OA groups compared with normals (Table 1-9). Each of the DXA studies used different sized ROIs at different locations within the proximal tibia. Conflicting results may therefore be due to the use of ROIs containing subchondral cortical, subchondral trabecular and/or epiphyseal trabecular bone, each of which may be affected differently by OA (Figure 1-10). For example, aBMD for OA subchondral bone near the subchondral surface (0-6.5 mm) was higher than normal while distally (16-24 mm), aBMD showed similar results [12]. OA is also associated with obesity [62] therefore findings of higher than normal aBMD with OA may not be due to disease presence but due to obese individuals having bigger bones. The larger bone size along the projection image would have larger aBMD—a limitation of DXA.

Table 1-9. Compilation of proximal tibial studies comparing image-based 2D areal BMD (aBMD) for OA and normal tissue. Studies are listed by proximity to the subchondral bone surface.

Author	Study type	ψStudy method	# Specimens Normal	# Specimens £OA	φBone type	~Distance from surface	Location / Category	2D Areal BMD (g/cm^2) Mean ± SD or Median [95% C.I.] Normal	Early OA	Late OA	OA findings	Comments
Madsen et al (1994)	In Vivo	DPA	24	28	SubC & SubT	0-6.5 mm	Medial	0.96 (0.72-1.25)		*1.21 (079-1.86)	•Higher medial aBMD •Lower lateral aBMD •Similar distal aBMD (16-24 mm)	•Reported Median (Range) •DPA was the natural precursor to DXA
							Lateral	0.77 (0.56-0.91)		*0.71 (0.14-1.05)		
							M/L	1.31 (1.02-1.77)		*1.98 (1.28-5.64)		
					Epi	6.5-16 mm		0.50 (0.42-0.66)		*0.58 (0.49-0.85)		
					Epi	16-24 mm		0.43 (0.21-0.78)		0.48 (0.05-1.12)		
Karvonen et al (1998)	In Vivo	DXA	43	43	SubC & SubT	0-6.5 mm	Medial	1.18	1.11		•Similar medial aBMD •Lower lateral aBMD	Attempted to create 3D BMD using sagittal 2D images, which are unreliable, and hence not included
							Lateral	1.06	*0.95			
					Epi	6.5-13 mm	Medial	0.91	0.84			
							Lateral	0.90	*0.81			
Bruyere et al (2003)	In Vivo	DXA		56	SubC & SubT	1-5 mm			0.85 ± 0.17	Reanalyzed OA knees after 1 year	Higher aBMD with lower joint space width	
Messent et al (2005)	Ex Vivo	DXA	11	11	SubT & Epi	2.5-8.5 mm	Medial	0.89 ± 0.25		0.84 ± 0.23	Similar aBMD with normals	ROIs not focused at compartment but extend below tibial spine
							Lateral	0.73 ± 0.29		0.71 ± 0.18		
					Epi	8.5-14.5 mm	Medial	0.66 ± 0.20		0.68 ± 0.19		
							Lateral	0.60 ± 0.21		0.61 ± 0.18		
Clarke et al (2004)	In Vivo	DXA	11	21	SubT & Epi	2.5-8 mm	Medial	1.10 [1.03-1.18]		1.14 [1.09-1.19]	Similar BMD with normals	
							Lateral	0.94 [0.88-1.00]		0.88 [0.84-0.91]		
Wada et al (2001)	In Vivo	DXA		23 / 46	Epi	5-25 mm	Medial		0.67 (0.23-1.13)	*0.77 (0.10-1.51)	•Higher medial aBMD •Similar lateral aBMD •Higher M/L ratio	•Reported Median (Range) •Lumbar aBMD did not differ between OA and normals
							Lateral		0.52 (0.15-0.94)	0.54 (0.12-1.11)		
							M/L		1.33 (0.86-1.55)	*1.54 (0.21-2.69)		

ψ Study imaging types include 2D dual energy x-ray absorptiometry (DXA, DEXA) and 2D dual photon absorptiometry (DPA)
£ OA population is either solely Early OA or Late OA, or a combination of the two (Early OA / Late OA)
φ Bone types include subchondral cortical bone (SbT), subchondral trabecular bone (SbT) and epiphyseal trabecular bone (Epi)
* $p < 0.05$, statistically significant difference between normal and OA or between Early OA and Late OA

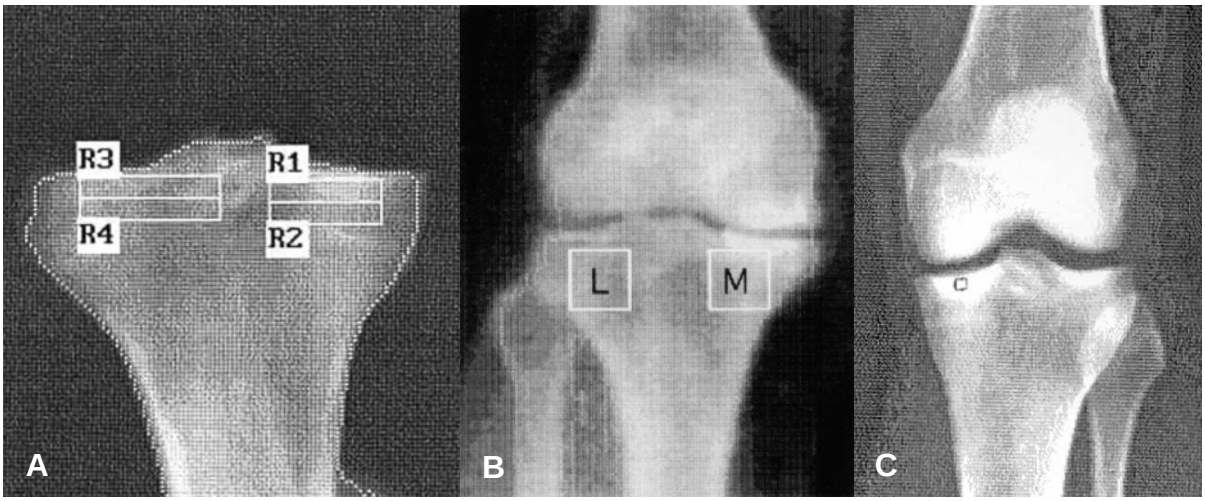

Figure 1-10. Different sized regions of interest using DXA. *A,* From Messent et al [27] with permission from Springer. *B,* From Wada et al [24] with permission from British Society for Rheumatology. *C,* From Bruyere et al [10] with permission from Elsevier.

1.4.2.2 Fractal Signature Analysis (FSA)

Fractal signature analysis (FSA) has been used to estimate differences in thickness and number of trabeculae between OA and normal proximal tibiae at sites distal to the subchondral surface (> 5 mm from surface) [27, 93-95]. FSA uses computational texture analyses of digitized 2D macroradiographs (4x-5x magnification) to define "fractal signatures" for each image (Figure 1-11). Fractal signatures pertaining to OA or normal bone can then be compared to better understand trabecular bone changes in OA. For example, FSA will count the number of trabeculae with thicknesses ranging between 0.48 and 0.60 mm for both OA and normal bone, and compare those quantities to determine if OA trabecular bone is thinner or has more trabeculae. Due to the planar nature of FSA, the tool suffers similar limitations as DXA (e.g., cannot characterize bone properties from a complex 3D region of interest, size related imaging artifacts, patient positioning errors). FSA is also limited to studying bone regions distal to the subchondral surface (> 5 mm) since subchondral cortical and subchondral trabecular bone show minimal "signatures" in macroradiographic images (i.e., subchondral cortical and

subchondral trabecular bone consistently appear primarily white). Previous studies using FSA to assess OA and normal proximal tibia showed OA trabeculae to be thinner than normal [27, 93, 94] and fewer in number [95] at sites distal to the subchondral surface (> 5 mm). This loss of bone is believed to be due to a "stress shielding" effect [73] caused by the increased subchondral cortical bone thickness and subchondral trabecular bone volume seen in OA. In contrast to subchondral bone stiffening theories proposed by Radin [4], Buckland-Wright [73] proposed that the increased amount of weakened subchondral cortical and subchondral trabecular bone near the subchondral surface decreases the overall stiffness of subchondral bone. A weakened subchondral bone will deform more during loading, leading to deformation being locally constrained to the subchondral bone region with reduced load transmission to the underlying epiphyseal bone. The result is localized osteoporosis [73] in-line with †Wolff's Law [100]. However, this theory is unsupported by evidence, and it is not known whether reduced epiphyseal trabecular bone changes occur before or after alterations of overlying subchondral cortical and trabecular bone.

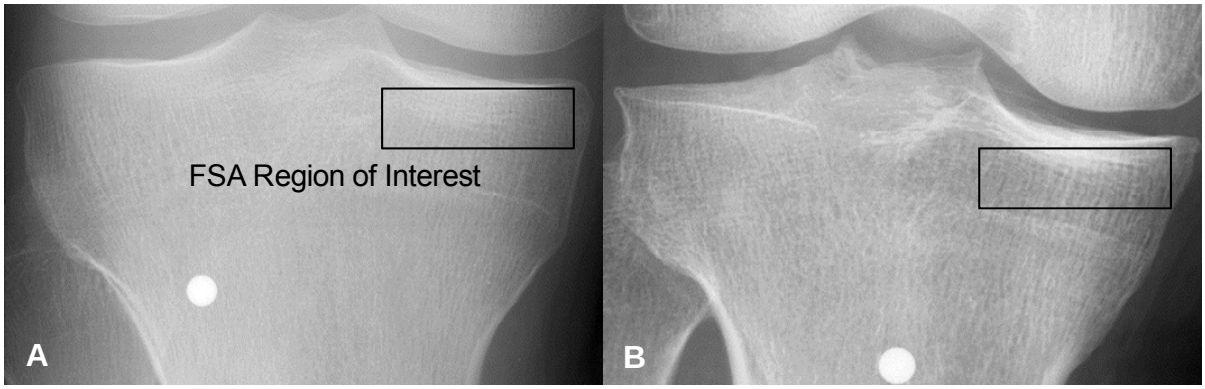

Figure 1-11. FSA microradiograph (4x magnification) of a left proximal normal (*A*) and OA tibia (*B*). Localized osteoporosis, manifested as increased radiolucency, is evident in the medial and lateral compartments of the OA tibia (*B*). The diameter of the ball bearing is 5 mm. From Messent et al [93] with permission of Osteoarthritis Research Society International.

† Wolff's Law [100] is a fundamental concept in bone research stating that bone will remodel in response to mechanical loading. If load increases, bone will remodel itself over time to become stronger at resisting loading. Likewise, if load decreases, bone will remodel and become weaker to reduce metabolic activity associated with bone maintenance.

1.4.2.3 Magnetic Resonance Imaging (MRI)

Bone volume fractions from OA and normal proximal tibia have been assessed *in vivo* using magnetic resonance imaging (MRI) [96-99] (Table 1-10). MRI offers multi-planar 3D images, nonionizing radiation, and the ability to simultaneously image both trabecular bone and articular cartilage. MR image acquisition is however time consuming (multiple minutes for a single MR image), therefore bone volume results are susceptible to motion artifacts. More importantly, MRI is unable to account for the mineralization of subchondral bone because MRI does not directly image bone but images high intensity fluids surrounding bone (e.g., fatty marrow, water). This is because bone shows no signal with MRI as it is primarily composed of calcium hydroxyapatite, which has only one proton which does not move. The decay time of bone is therefore very short and minimal signal arises, leading to bone appearing black with MRI [101, 102] (Figure 1-12). By measuring fluid intensity, indirect measures of bone quantity can be obtained using MRI. However, subchondral cortical bone and trabecular bone near the subchondral surface have minimal fluid presence; therefore MRI measures of subchondral bone quantity are primarily limited to trabecular regions apart from morphological measures (e.g., cortical thickness and/or volume). Due to an inability to quantify the mineralization of subchondral bone, combined with long scanning times, MRI is ill-suited for studying subchondral cortical and/or subchondral trabecular bone changes in OA.

The few studies which used MRI to assess OA and normal proximal tibial bone volume fractions were limited to epiphyseal trabecular bone sites distal to the subchondral surface (e.g., 5-10 mm). These studies found epiphyseal trabeculae bone volume fractions in OA proximal tibia to be lower than normal in two studies [96, 98] and similar in two others [97, 98] (Table 1-10). Lower than normal bone volume fractions have been attributed to epiphyseal trabecular bone having thinner trabeculae [96, 97] and larger spaces between adjacent trabeculae [96, 98]. It therefore appears that

Table 1-10. Compilation of *in vivo* proximal tibial studies comparing subchondral bone volume fraction (%) in OA and normal tissue. Studies are listed by proximity to the subchondral bone surface.

Author	Study type	Study method	# Specimens		φBone type	~Distance from surface	Location / Category	‡ Bone Volume Fraction (%) Mean ± SD or [95% confidence interval]			OA findings	Comments
			Normal	£OA				Normal	Early OA	Late OA		
Lindsay et al (2004)	In Vivo	MRI	12	21/32	Epi	5-10 mm	Medial	29 ± 4	29 ± 6	28 ± 5	No difference in bone volume at sites distal to surface	•For MRI studies, OA categorized using Kellgren Lawrence scoring: OA0 - KL=0 OA1 - KL=1-2 OA2 - KL=3-4 •Young sample population OA: 36 ± 11; Normal: 47 ± 12
							Lateral	33 ± 3	31 ± 7	31 ± 6		
Bolbos et al (2008)	In Vivo	MRI	16	16	Epi	5-10 mm	Medial	43 ± 7	*37 ± 12		Lower bone volume at sites distal to surface with Early OA	
							Lateral	43 ± 9	*36 ± 10			
Beuf et al (2002)	In Vivo	MRI	10	8/10	Epi	5-50 mm		28 ± 2	*25 ± 2	28 ± 4	Lower bone volume at sites distal to surface with Early OA	

£ OA population is either solely Early OA or Late OA, or a combination of the two (Early OA / Late OA)

φ Bone types include subchondral cortical bone (SbT), subchondral trabecular bone (SbT) and epiphyseal trabecular bone (Epi)

‡ Bone volume fraction (bone volume / total specimen volume)

* $p < 0.05$, statistically significant difference between normal and OA samples

epiphyseal trabecular bone volume decreases with OA while *ex vivo* research suggests that subchondral trabecular bone volume increases.

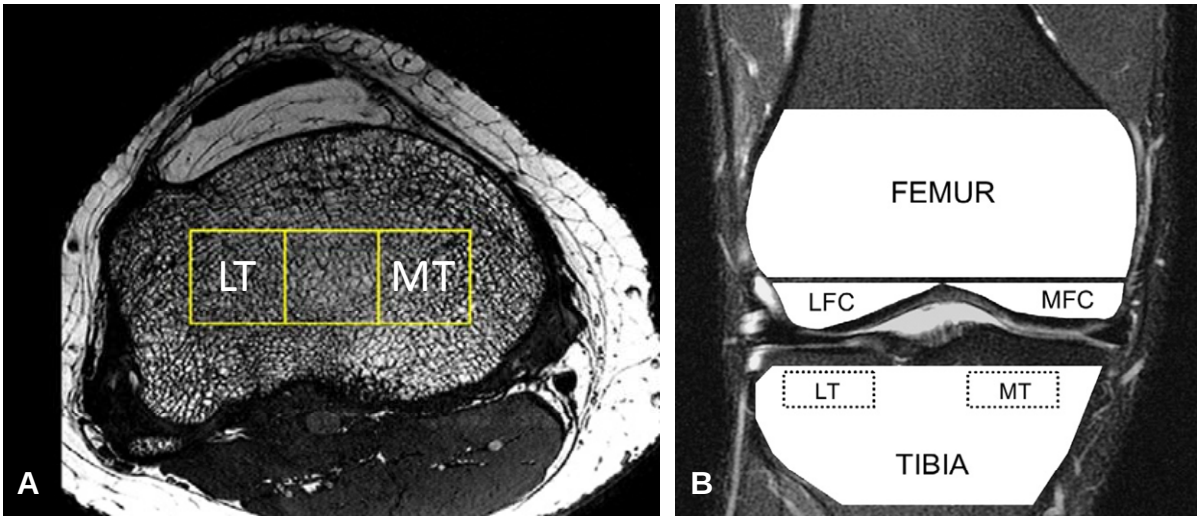

Figure 1-12. Axial (*A*) and coronal (*B*) images of analyzed medial and lateral trabecular bone regions from MR images. Modified from Bolbos et al [96] with permission from Osteoarthritis Research Society International.

1.4.2.4 Quantitative Computed Tomography (QCT)

Quantitative CT (QCT) is a CT based imaging tool capable of imaging 3D cortical and trabecular density. QCT uses CT radiographic absorption techniques and calibration phantoms to convert grayscale CT Hounsfield units (HU) to equivalent volumetric BMD (vBMD, mg/cm^3). Non-invasive *in vivo* measures of vBMD are comparable with laboratory-based measures of [₮]apparent density; with proximal tibial vBMD measures being approximately equal to apparent density halved (vBMD ≈ $\rho_{app}/2$) [83]. vBMD, like apparent density, therefore captures both the amount of bone tissue (bone volume fraction) and mineralization content (material density) present in OA, but it cannot assess each measure separately.

[₮] QCT measures of vBMD are most closely correlated with ash density (ash mass / total volume) (r^2 = 0.96 [83]), not apparent density. However, ash density is approximately equal to $\rho_{app}/2$, therefore conversions can be made between the different types of densities [83].

Peripheral QCT (pQCT)—a type of QCT imaging technology—has recently been used for the first time to study proximal tibial bone density from patients living with knee OA [28] (Table 1-11, Figure 1-13). This study showed that normal, early OA, and late OA knees had similar whole compartment vBMD in the epiphyseal trabecular bone regions (~6.4-8.6 mm from surface) [28]. This study also showed that late OA bone had lower than normal vBMD in the posterior regions of medial and lateral compartments [28]. It is, however, difficult to image proximal tibial subchondral cortical and subchondral trabecular bone density near the subchondral surface using pQCT. This is because pQCT scanners are often limited to a single axial CT scan with a relatively large slice thickness (typically fixed to 2.3 mm), leading to significant partial volume effects at the subchondral bone surface and an imaged dependence upon correct patient positioning. pQCT scanning times are also long (minutes for a single pQCT scan), therefore density results are susceptible to motion artifacts. Further, pQCT scanners are not widely available and are typically limited to academic research centers.

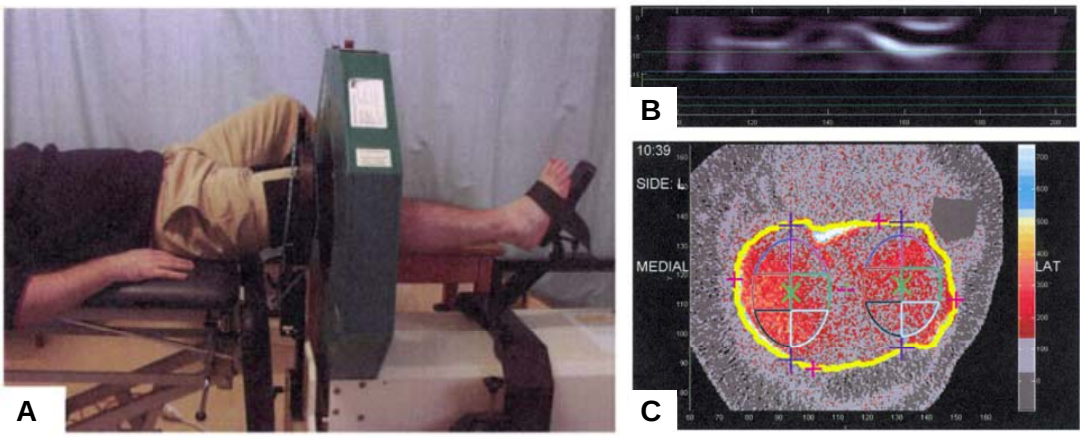

Figure 1-13. *A,* Subject positioning for pQCT measurement of tibial subchondral trabecular vBMD. *B,* Scout view, showing medial and lateral reference lines. *C,* Axal pQCT scan of the subchondral tibia, showing the medila and lateral elliptical regions of interest used for BMD assessments. From Bennell et al [28] with permission from Wiley.

Table 1-11. Compilation *of in vivo* and *ex vivo* proximal tibial studies assessing 3D volumetric apparent BMD in OA and normal tissue.

Author	Bone region	Study type	Study method	Ω Density type	# Specimens		φ Bone type	~Distance from surface	Location / Category	Sex	3D Volumetric BMD (g/cm^3) Mean ± SD or Median [95% C.I.]			OA comparison with normal findings	Comments
					Normal	£ OA					Normal	Early OA	Late OA		
Bennell et al (2008)	Proximal tibia	In Vivo	pQCT	ρ_{pQCT}	41	40/35	Epi	7.5-12.5 mm	Medial		0.21 ± 0.03	0.21 ± 0.03	0.20 ± 0.03	•Similar whole compartment densities between OA and normals •Posteriorly, lower medial and lateral vBMD nearest joint surface with OA	•Posterior vBMD results average of central and peripheral vBMD measures •OA lateral compartment showed marginal differences with normals (p=0.057)
									M Pos		0.19	0.18	*0.16		
									Lateral		0.19 ± 0.03	0.18 ± 0.03	0.17 ± 0.04		
									L Pos		0.23	0.22	*0.20		
							Epi	15-20 mm	Medial		0.19 ± 0.03	0.19 ± 0.03	0.18 ± 0.04		
									Lateral		0.16 ± 0.03	0.16 ± 0.03	0.15 ± 0.03		
Khodadadyan-Klostermann et al (2004)	Proximal tibia	Ex Vivo	QCT	ρ_{QCT}	40		Epi	5-12 mm	M Ant	M	0.12 [0.04-0.19]			•Males had higher vBMD than females •Females > 60 years had lower vBMD than females < 60 years of age	•Report Mean [95% C.I.] •Reported female group > 60 years of age •Soft tissue removed prior to QCT imaging
									M Pos		0.20 [0.12-0.25]				
									L Ant		0.22 [0.10-0.26]				
									L Pos		0.23 [0.13-0.27]				
									M Ant	F	0.06 [0.03-0.13]				
									M Pos		0.10 [0.06-0.23]				
									L Ant		0.12 [0.08-0.17]				
									L Pos		0.12 [0.05-0.22]				

Ω Density types include:

ρ_{pQCT} - imaged volumetric bone mineral density (vBMD) using peripheral QCT (pQCT).

ρ_{QCT} - imaged vBMD using QCT.

pQCT and QCT measured density is most closely related with ash density (Keyak et al., 1994).

ρ_{pQCT} and ρ_{QCT} at the proximal tibia is approximately equal to ρ_{app}/2 (Keyak et al., 1994).

£ OA population is either solely Early OA or Late OA, or a combination of the two (Early OA / Late OA)

φ Bone types include subchondral cortical bone (SbT), subchondral trabecular bone (SbT) and epiphyseal trabecular bone (Epi)

* $p < 0.05$, statistically significant difference between normal and OA or between Early OA and Late OA

Clinical QCT has potential to identify and quantify OA-related changes in subchondral bone density *in vivo* because of recent technological advances. Until recently, available clinical CT imaging slice thicknesses were large (1-4 mm) and therefore poorly suited for imaging thin layers of subchondral cortical and trabecular bone. This may partially explain why the literature contains no reports of QCT assessments of OA and normal proximal tibial subchondral bone. Currently available clinical CT scanners now offer small isotropic voxel sizes (0.5–0.625 mm) which enable reliable data reconstructions in any plane of choice and thereby minimize imaged density dependence upon correct patient positioning. QCT also offers wide availability using whole body clinical CT scanners (Figure 1-14) and very short acquisition times (seconds for hundreds of axial QCT images). Concerns regarding ionizing radiation dosage with QCT are also minimal due to the low presence of radiosensitive tissues at the knee joint. The effective dosage associated with a CT scan for knee replacement surgery is 0.12 mSv [103]. This compares with an average exposure of 2.4 mSv of background radiation per year [104], approximately 0.05 mSv during a transatlantic flight from Europe to North America [105], and 0.7 mSv [106, 107] for a pelvic radiograph or a long-leg standing radiograph.

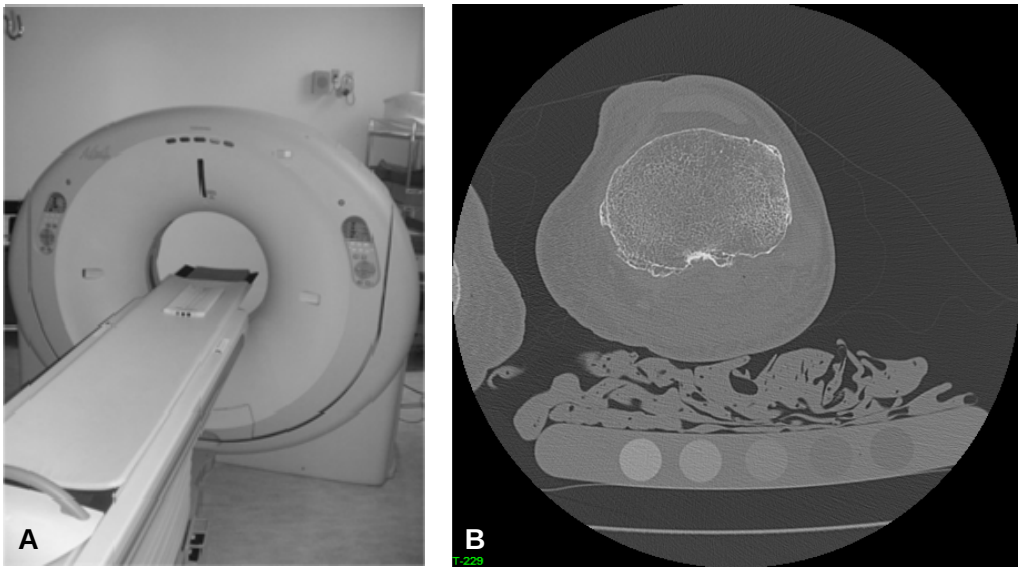

Figure 1-14. *A*, Common clinical CT scanner. *B*, Axial QCT image of tibia, which is a CT image including a QCT reference phantom to convert CT Hounsfield Units (HU) to vBMD (mg/cm^3 K_2HPO_4).

The benefits of clinical QCT, particularly the ability to characterize small 3D regions of interest, make this tool well suited for characterizing subchondral cortical and trabecular bone density at sites near the proximal tibial subchondral surface. To date only one study has used clinical QCT to assess proximal tibial vBMD [108] (Table 1-11), and this *ex vivo* study of normal proximal tibiae was limited to epiphyseal and metaphyseal trabecular bone regions. To my knowledge, no study has used clinical QCT to assess vBMD of proximal tibial subchondral bone regions for both normal and OA populations.

It is worth noting that although no studies have used clinical QCT to assess subchondral vBMD at the proximal tibia, CT has been previously used to assess proximal tibial bone density [109-111] (though no studies quantitatively assessed OA density). These studies did not include a calibration phantom (i.e., reported HU in place of vBMD) even though HU measures are highly influenced by CT scanning parameters (voltage, current) and beam hardening effects. For these reasons, previous CT studies which did not include a QCT reference phantom within each CT image cannot be compared alongside existing QCT measures of vBMD or laboratory-based measures of apparent density, and are therefore excluded from this review.

1.4.2.5 Computed Tomography Osteoabsorptiometry (CT-OAM)

Computed tomography osteoabsorptiometry (CT-OAM) is a QCT-based imaging technique used to characterize subchondral bone density—primarily subchondral cortical bone density—directly at the joint surface [111-116]. CT-OAM employs QCT and maximum intensity projection (MIP) image processing to select the maximum subchondral bone densities contained within the subchondral bony region, ignoring less dense bone located above or below the maximum density, and projects maximum density results to a 2D MIP image (Figure 1-15-A). Previous CT-OAM research has largely focused on the shoulder [112, 114], though studies have also been completed at the knee looking at the patella [114, 115] (Figure 1-15-B) and tibia (but only qualitatively) [111]. The only reported application of CT-

OAM to quantify OA subchondral bone density was at the patella [117]. It is currently unknown whether CT-OAM can be used to distinguish OA from normal proximal tibial subchondral bone density. The selection of maximum densities by CT-OAM largely limits its use to the highly dense subchondral cortical bone region. The effectiveness of CT-OAM at studying OA-related changes in subchondral trabecular and epiphyseal trabecular bone density is therefore likely limited, though currently unknown.

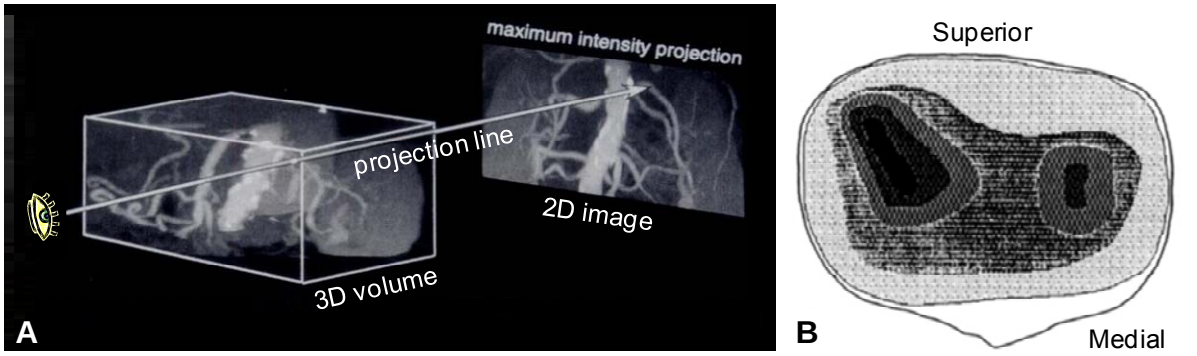

Figure 1-15. *A,* Diagram illustrating basic principle of maximum intensity projection (MIP): parallel rays or projection lines are cast through a 3D volume of interest, and the maximum CT intensity along each projecting ray is displayed on a 2D MIP image. Modified from Prokop et al [118] with permission from Radiological Society of North America. *B,* Posterior view of the surface of a patella showing the subchondral bone density distribution following CT-OAM MIP image processing. Black corresponds with high density bone. Modified from Muller-Gerbl et al [114] with permission from the American Society for Bone and Mineral Research.

1.4.2.6 Critique of *In Vivo* Research

In vivo research studies suggest that subchondral trabecular and epiphyseal trabecular bone—which differ in location and depth from the subchondral surface—may be affected differently by the OA process. *In vivo* research studies of OA trabecular bone distal to the proximal tibial subchondral surface from epipihyseal trabecular bone regions show reduced bone volume fractions [96, 98], trabecular thickness [27, 93, 94, 96], and vBMD [28]. These results differ from *ex vivo* research studies which suggest that subchondral bone nearest the subchondral surface increases in thickness [73], bone volume [14, 15, 75] and apparent density [54] with OA. The transition zone between these two types of bone appears to be located approximately 5 mm from the subchondral surface (Figure 1-16). These results highlight the importance of an imaging technique capable of characterizing bone properties across different regions and depths from the subchondral surface.

Currently available clinical imaging tools for assessing bone properties are poorly suited for analyzing region- and depth-specific variations at the proximal tibia. DXA is limited to 2D measures of aBMD and therefore cannot characterize a complex 3D region nor distinguish between subchondral cortical and trabecular bone near the subchondral surface. FSA is limited to epiphyseal trabecular bone regions. MRI is unable to characterize bone mineralization and is limited to epiphyseal trabecular bone regions. pQCT is limited to a single axial CT scan of fixed thickness (typically 2.3 mm) and is therefore susceptible to large partial volume effects near the subchondral bone surface. CT-OAM is likely limited to imaging only subchondral cortical bone density. Clinical QCT is an imaging technique capable of assessing 3D vBMD and offers potential usage for characterizing OA and normal subchondral cortical, subchondral trabecular and epiphyseal trabecular bone density across different regions and/or depths from the subchondral surface.

Figure 1-16. Compilation of *ex vivo* proximal tibial studies comparing bone volume fraction between normal (black border), early OA (yellow border) and late OA (red border) subjects.

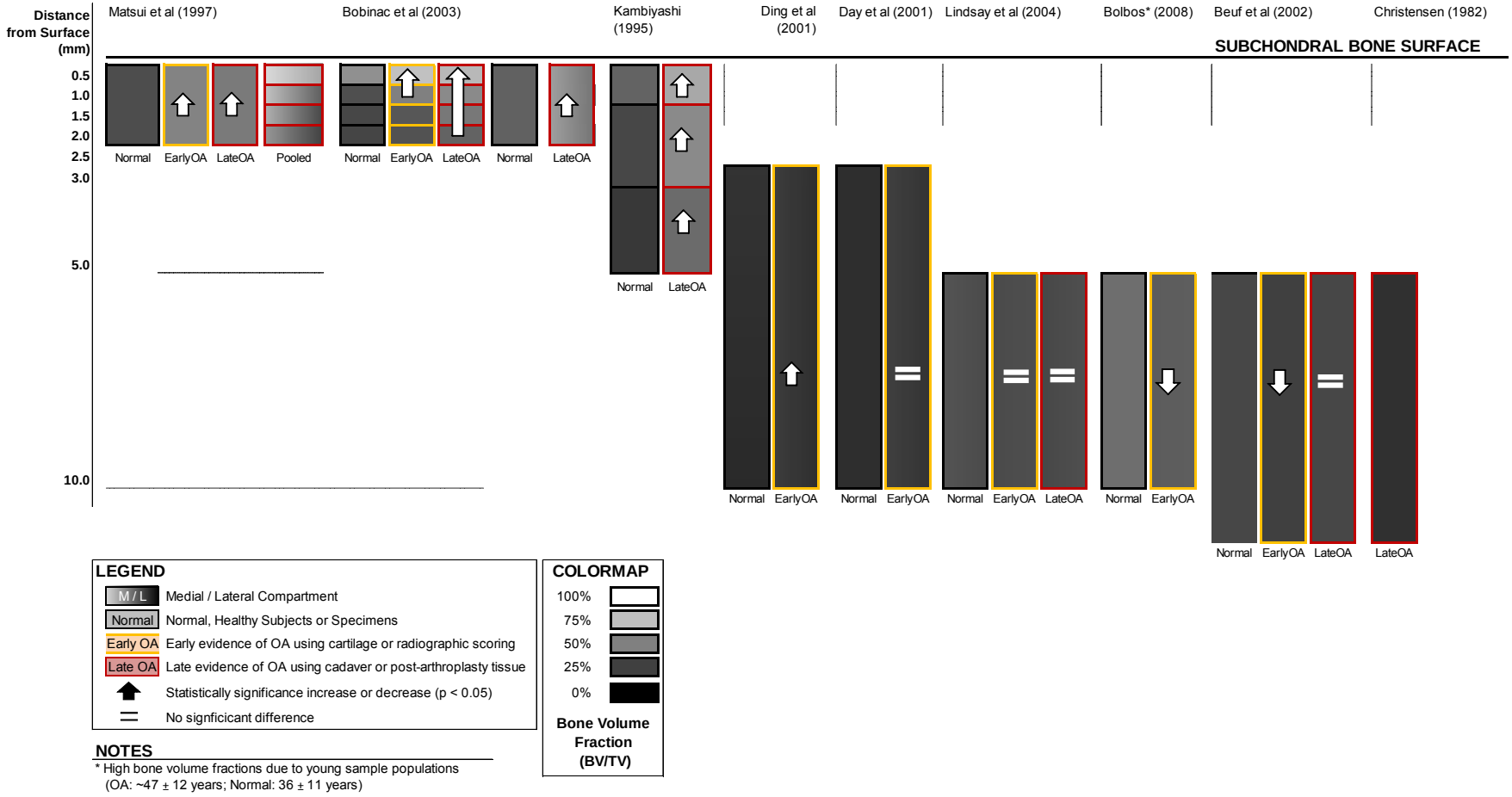

1.5 Predicting Subchondral Bone Stiffness

Clinical QCT could potentially be used to non-invasively predict subchondral bone stiffness in addition to characterizing subchondral bone density. By linking QCT-derived BMD with laboratory-based measures of subchondral bone stiffness, it may be possible to derive stiffness-density relationships for non-invasive predictions of subchondral bone stiffness. Importantly, non-invasive stiffness predictions could be used to directly test hypotheses regarding the mechanical role of subchondral bone in people living with OA.

Various studies have shown direct relationships between laboratory-based apparent density and the material stiffness E of proximal tibial trabecular bone [79, 80, 82-89] (Table 1-12). These stiffness-density relationships are typically characterized by a nonlinear power law function, i.e., $E = \rho_{app}^{\gamma}$, with γ focused around a value of 2 at the proximal tibia (Table 1-12). This is an important relationship because a small change in density could result in a large change in stiffness. This information could help explain the role of subchondral bone alternations in OA etiology more effectively than bone density alone. Recalling that apparent density can be equated with ¥vBMD ($\rho_{app} = 2.01 \cdot vBMD + 0.15$ [83]), QCT could be used to non-invasively estimate the mechanical and/or structural stiffness of bone.

To date, no studies have established stiffness-density relationships for subchondral bone from the proximal tibia. All existing studies have established stiffness-density relationships for epiphyseal or metaphyseal trabecular bone, using only normal tissue (Table 1-12). The mechanical testing method most commonly used to investigate stiffness-density relationships was the platen technique. This technique involves unconstrained compression testing of bone samples excised from trabecular

¥ ρ_{app} - apparent density or wet apparent density (hydrated bone mass / total specimen): $\rho_{app} = 2.01 \cdot \rho_{QCT} + 0.15$
ρ_{dry} – dry apparent density (dry mass / total specimen): $\rho_{dry} = 1.85 \cdot \rho_{QCT} + 0.063$
ρ_{ash} - ash density (ash mass / total specimen): $\rho_{ash} = 1.11 \cdot \rho_{QCT} + 0.036$ [83]

regions of the proximal tibial epiphysis and metaphysis (typically > 5 mm from subchondral surface). However, it is unlikely that the material properties of isolated tissues distal to the subchondral surface accurately reflect the overall structural stiffness of subchondral bone directly *at* the subchondral surface. Further, it is the bone located closest to the subchondral surface (< 5 mm) which offers maximal resistance to loading [90] and greatest potential to negatively affect the overlying cartilage [19].

As opposed to platen compression of excised bone samples, *in situ* macro indentation testing directly at the subchondral surface may be more representative of the *in vivo* condition [119], and may more accurately reflect bone's response to cartilage loading. Macro indentation testing has been the preferred method for determining subchondral bone mechanical properties from various articulating bones [55, 90, 120-128], including the proximal tibia [55, 90, 120, 121]. The macro indentation test typically involves displacement of a flat cylindrical indentor (generally 3 to 4 mm diameter [121-124, 127]) to a depth of 0.2 to 0.5 mm [90, 122, 123] at a slow displacement rate (2 mm/min) (Figure 1-17).

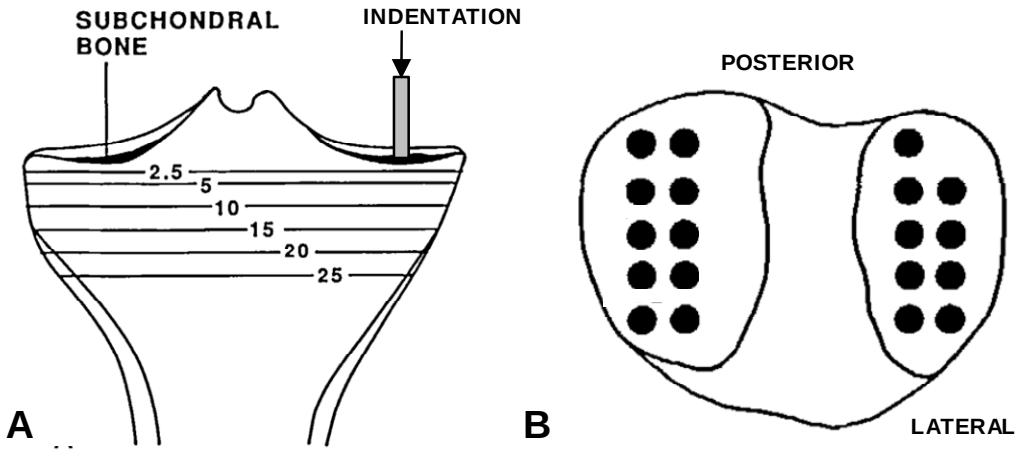

Figure 1-17. *A*, Illustration of macro indentation test directly at the subchondral bone surface. *B*, Distribution of indentation test sites at the proximal tibia. From Harada et al [90] with permission from Elsevier.

Table 1-12. Compilation of proximal tibial and femoral studies relating apparent density with the material stiffness (modulus of elasticity E) of bone.

Author	Bone region	Study type	ψStudy method	ΩDensity type	Joint status	# Bones	# Tests	φBone type	~Distance from surface	Density range (g/cm^3)	Modulus range (MPa)	Modulus-Density Relation (MPa, g/cm^3) E	r^2	Comments
Carter & Hayes (1977)	Proximal tibia	Ex Vivo	Confined compression	ρ_{app}	Normal		100			0.07-2.0	10-500	$E = 2875\rho_{app}^{3}$		E-ρ strain dependent, example is for 0.01/s rate
Hvid et al (1989)	Proximal tibia	Ex Vivo	Platen	ρ_{dry}	Normal	10	250	Epi	5-12.5, 12.5-20 mm	0.05-0.60	60-1250	$E = 2132\rho_{drv}^{1.46}$	0.61	
Linde et al (1989)	Proximal tibia	Ex Vivo	Platen	ρ_{dry}	Normal	5	33	Epi	5-12.5, 12.5-20 mm	€0.13-0.45	105-942	$E = 10256\rho_{dry}^{2.5}$	0.85	
Linde et al (1990)	Proximal tibia	Ex Vivo	Platen	ρ_{dry}	Normal	5	119	Epi	5-12.5, 12.5-20 mm		67-734	$E = 1012\rho_{drv}^{1.13}$	0.52	
Linde et al (1991)	Proximal tibia	Ex Vivo	Platen	ρ_{dry}	Normal	1	60	Epi		0.23-0.59	90-1000	$E = 1798\rho_{drv}^{1.56}$	0.71	
Odgaard et al (1991)	Proximal tibia	Ex Vivo	Platen	ρ_{ash}	Normal	1	18	Epi	5-12.5, 12.5-20 mm	0.10-0.29	108-1637	$E = 23544\rho_{ash}^{2.1}$	0.72	
Linde et al (1992)	Proximal tibia	Ex Vivo	Platen	ρ_{dry}	Normal	4	31	Epi	5-12.5, 12.5-20 mm	€0.12-0.43	€0-679	$E = 4778\rho_{drv}^{1.99}$	0.79	4 knees from 2 subjects
Anderson et al (1992)	Proximal tibia	Ex Vivo	Platen	ρ_{dry}	Normal	4	30	Epi	10-30 mm	0.14-0.48	32-1066	$E = 3890\rho_{drv}^{2}$		•4 knees from 2 subjects •E range from Appendix
Keyak et al (1994)	Proximal tibia	Ex Vivo	Platen	ρ_{ash}	Normal	4	36	Epi	5-29, 30-54, 55-79 mm	0.06-0.27	36-2767	$E = 33900\rho_{ash}^{2.2}$	0.84	4 knees from 2 subjects
Morgan et al (2003)	Proximal tibia	Ex Vivo	End-caps	ρ_{app}	Normal	15	15	Epi	8-32 mm	0.09-0.41	10-2770	$E = 15520\rho_{app}^{1.93}$	0.84	
Li & Aspden (1997)	Femoral head	Ex Vivo	Platen	ρ_{app}	Normal OA	7 16	49 112	SubT & Epi	2.5-10 mm	0.17-1.05 0.17-1.4	10-550 20-650	$E = 573\rho_{app} - 9.4$ $*E = 278\rho_{app} + 129$	0.59 0.33	OA bone was less stiff for identical density

ψ Study methods include:

Platen Compression - Excised bone cubes or cores compressed between two platen surfaces. Specimens are not fixed to mechanical testing apparatus.

End-caps - The test ends of the specimens are fixed to the mechanical testing apparatus

Confined Compression - Excised bone cubes pressed into cylinder, then compressed

φ Bone types include subchondral cortical bone (SbT), subchondral trabecular bone (SbT) and epiphyseal trabecular bone (Epi)

€ Range represents 95% confidence interval, either provided or established using Mean ± 1.96·SD

Ω Density types include:

ρ_{app} - apparent density or *wet* apparent density (hydrated bone mass / total specimen volume)

ρ_{dry} - dry apparent density (dry bone mass / total specimen volume). $\rho_{dry} = 0.92 \cdot \rho_{app}$ (Keyak et al., 1994)

ρ_{ash} - ash density (ash mass / total specimen volume). $\rho_{ash} = 0.55 \cdot \rho_{app}$ (Keyak et al., 1994)

The *in situ* macro indentation test is essentially a test of structural stiffness, which is dependent upon both material stiffness properties of the underlying tissues and physical size of the tissues being tested. However, many researchers have used the traditional Timoshenko-Goodier indentation equation to approximate the material stiffness of subchondral bone [129]. Material stiffness, in contrast to structural stiffness, describes the intrinsic material properties of bone itself independent of specimen geometry or size. The Timoshenko-Goodier indentation equation is important because it enables comparisons with traditional findings using the platen-technique. The Timoshenko-Goodier equation for indentation is expressed as:

$$E = k \cdot \frac{(1 - v^2)}{2r}$$

where ν is Poisson's ratio, *r* is the radius of the indentor, *k* is the slope of the load-displacement curve, and *E* is the local modulus of elasticity. This equation assumes continuous, homogeneous, isotropic conditions. It is important to note that although the Timoshenko-Goodier equation approximates material stiffness, the *in situ* macro indentation test is essentially a test of structural stiffness.

To date, macro indentation testing has been used to determine the stiffness of proximal tibial subchondral bone [55, 120, 121], but these studies have been limited to subchondral trabecular bone. No studies have determined the structural stiffness of subchondral bone directly at the subchondral bone surface. Further, no proximal tibial studies have established direct relationships between the stiffness of bone located near the subchondral surface (< 5 mm) with corresponding measures of density (neither laboratory-based apparent density or QCT-based BMD).

Stiffness-density relationships for normal and OA subchondral bone may differ due to OA-related alterations in bone volume, material density and apparent density. This is supported by observations at the hip [49] where the slope of the stiffness-density curve for OA subchondral bone (subchondral trabecular and epiphyseal trabecular bone) is approximately half that for normal bone

(Figure 1-18, Table 1-12). This discrepancy was explained by OA bone being hypomineralized with higher than normal bone volume [49]. Therefore, for identical apparent densities, OA stiffness was less than normal stiffness. This is an important concern because while OA bone may appear highly dense according to QCT-based measures of vBMD and therefore assumed highly stiff, it may in fact be less stiff than normal bone. To date, no studies have verified whether stiffness-density relationships differ between OA and normal proximal tibial subchondral bone.

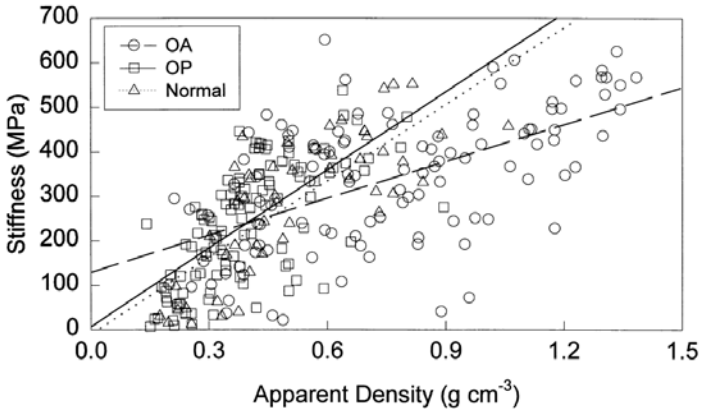

Figure 1-18. Linear regression relationships between stiffness and apparent density of cancellous bone from late-OA femoral heads. OA bone is significantly different from normal bone. From Li et al [49] with permission from the American Society for Bone and Mineral Research.

1.6 Summary

1. The exact role and timing of subchondral bone changes in OA is unclear, but it appears that subchondral bone is intricately involved in the progression of OA. Leading hypotheses propose that mechanical and morphological changes in subchondral bone could initiate and accelerate the OA disease process.
2. Understanding subchondral bone changes is vital to improving OA prevention, diagnosis and treatment. There is a need for a tool to assess subchondral bone changes non-invasively in living people. Much of our understanding of OA-related subchondral bone changes has come

from animal models, which may not be applicable to humans, or cadaveric tissues, where longitudinal assessments are not possible and changes cannot be related to symptoms.

3. Human studies of subchondral bone volume, material density, and apparent density suggest that the different constituents of subchondral bone (subchondral cortical, subchondral trabecular and epiphyseal trabecular bone), which differ in location and depth from the subchondral surface, are affected differently by OA.
4. Noninvasive imaging tools have been used to study the role of subchondral bone in OA, but existing imaging methods are poorly suited for analyzing the region- and depth-specific variations in bone density at the proximal tibia that are likely critical in understanding the disease process.
5. QCT has potential to image small changes in vBMD associated with OA disease progression at sites near the subchondral bone surface. However, the image processing tools used to date (chiefly CT-OAM) are poorly suited for analyzing subchondral cortical, subchondral trabecular and epiphyseal trabecular bone density.
6. Changes in subchondral bone stiffness have been hypothesized to play a key role in OA, but this has not been tested in humans because we lack a tool to assess subchondral bone stiffness non-invasively. A QCT-based method has potential to non-invasively estimate subchondral bone stiffness as well as density.

1.7 Research Questions and Objectives

The fundamental question which motivates my doctoral research is: What role does subchondral bone play in the OA disease process? To help answer this fundamental question, the goal of my dissertation research was to develop a noninvasive imaging tool which could be used to characterize subchondral

bone density and estimate bone stiffness *in vivo*. Using a novel technique incorporating QCT images, in combination with mechanical indentation testing, I aimed to answer the following research questions:

1. Can a QCT-based imaging technique characterize the density and thickness of subchondral cortical and trabecular bone in the proximal tibia?
2. Can this imaging technique identify patterns of subchondral bone density that are characteristic of OA?
3. Does this imaging technique's ability to measure depth-dependent properties give it advantage over existing imaging methods (CT-OAM) for distinguishing between normal and OA joints?
4. How precise are this technique's measures of subchondral bone density, both *in vitro* and *in vivo*?
5. Can this imaging technique be used to non-invasively estimate the stiffness of subchondral bone measured directly at the subchondral surface in normal and OA joints?

To answer the questions posed in this study, our objectives were to:

1. Develop a novel noninvasive imaging tool capable of imaging 3D proximal tibial subchondral bone density in relation to depth from the subchondral surface using QCT and the surface projection image processing method.
2. Identify differences in patterns of subchondral bone density between normal and OA proximal tibiae using this novel imaging technique and an existing imaging method (CT-OAM).
3. Determine the *ex vivo* and *in vivo* precision of proximal tibial subchondral bone density measures using this novel imaging technique.
4. Determine whether QCT-derived density measures of proximal tibial subchondral bone predict bone stiffness values obtained using *in situ* macro indentation testing.

1.8 Scope

Chapter 2 outlines the methodological details of our developed subchondral bone imaging tool, computed tomography topographic mapping of subchondral density (CT-TOMASD). Chapter 2 also presents *ex vivo* precision results of density measures using CT-TOMASD and isolated comparisons of OA and normal proximal tibial subchondral density patterns. Chapter 3 describes our comparisons of CT-TOMASD layer analyses and CT-OAM maximum intensity projections for distinguishing OA from normal proximal tibial bone density patterns. Chapter 3 also describes technical and methodological differences between CT-TOMASD and CT-OAM. Chapter 4 describes our test of the precision of CT-TOMASD measures, *in vivo*, in knees with and without evidence of OA. Chapter 5 describes our tests of the ability of CT-TOMASD layer analyses to predict, non-invasively, subchondral bone structural stiffness in OA and normal proximal tibiae. Chapter 6 reviews the findings of this research and offers recommendations for future research.

2 CT-TOMASD Methodological Development and Preliminary Findings

2.1 Synopsis

This chapter outlines the methodological details of our novel subchondral bone imaging tool, computed tomography topographic mapping of subchondral density (CT-TOMASD), which characterizes and maps 3D subchondral cortical and trabecular BMD in relation to depth from the subchondral surface. This chapter also presents *ex vivo* precision results of density measures using CT-TOMASD along with isolated comparisons of OA and normal proximal tibial subchondral density patterns.

2.2 Introduction

Subchondral bone changes during the OA disease process have become a controversial and growing area of focus in OA research. Currently, the exact role or timing of OA subchondral bone changes are not well understood [17, 29], in particular, whether the observed changes occur prior to, simultaneously or secondary to articular cartilage degeneration [130]. The different components of proximal tibial subchondral bone (subchondral cortical bone; subchondral trabeculae bone; epiphyseal trabeculae bone), which differ in location and depth from the subchondral surface, may undergo different alterations in architecture and density at different stages of OA progression [17, 28, 29]. Improved understanding of bone density changes across these regions and depths in people living with OA could help clarify the role of subchondral bone in OA disease initiation and progression.

Currently available clinical imaging tools for bone density assessment (DXA and pQCT) are poorly suited for analyzing region- and depth- specific variations at the proximal tibia. Clinical QCT offers a promising alternative to DXA- and pQCT-based measures of subchondral bone density. QCT offers wide availability using clinical CT scanners [30, 31], short acquisition times for large 3D datasets, and small isotropic voxel sizes which permit separation of 3D cortical and trabecular bone density.

The objective of this study was to develop a novel clinical imaging tool: CT-TOMASD (computed tomography topographic mapping of subchondral density), which employs QCT and a surface projection image processing method to characterize and map 3D subchondral density in relation to depth (measured relative to the subchondral surface). Our research questions were:

1. Can CT-TOMASD provide repeatable and precise measures of subchondral bone density in human cadaver specimens?
2. Using preliminary cadaveric results, does CT-TOMASD demonstrate potential to discriminate differences in subchondral bone density patterns between normal and osteoarthritic joints?

2.3 Methods

2.3.1 Specimens

We obtained sixteen intact fresh human cadaver knee specimens, including tissues 25 cm proximal and distal to the tibio-femoral joint line (~50 cm total length), from the University of British Columbia Anatomy Department and an anatomical tissue bank (LifeLegacy, St. Paul, MN, USA). Specimens came from ten consenting donors (8 males and 2 females; ages ranging from 67 to 88 years (mean ± standard deviation (SD): 77.8 ± 7.4)) and included six left:right pairs, two right and two left knees. We wrapped the specimens in saline soaked towels, sealed, and stored them at −20 °C. Prior to preparation or scanning, we thawed the sealed specimens for 18 hours at 20 °C (room temperature). Study approval was provided by the University of British Columbia Clinical Research Ethics Board (CREB #: H03-70308).

2.3.2 Imaging Methodology

2.3.2.1 QCT Image Acquisition

We imaged intact knee specimens using single-energy quantitative computed tomography (QCT) with a multi-slice helical CT scanner (64-slice helical Aquilion 64, Toshiba Medical Systems, Tokyo, Japan). The QCT image volume included the patella, distal femur and proximal tibia, though only QCT images of the proximal tibia were used in this analysis. CT scanning parameters included: bone reconstruction kernel (FC30), axial scanning plane, 120 kVp tube voltage, 300 mA tube current, ~3.7 second scan time, ~300 slices, 0.5 isotropic voxel size (0.5 mm slice thickness, 0.5 x 0.5 mm in-plane pixel size). Our voxel size was based upon 1) recommendations by the QCT phantom manufacturer that the z-dimension of the 3D voxel match the slice thickness capabilities of the CT machine (0. 5 mm), and 2) a preference to use isotropic voxels for CT-TOMASD analyses. The primary advantage of isotropic voxels is the ability to perform reliable data reformations in any plane of choice — a process unsuitable for voxels with differing slice thicknesses and in-plane pixel resolutions. To simulate a physiologic setting, we oriented left and right knees in a supine position and imaged simultaneously with the knee of interest centrally located within the CT gantry. We included a solid dipotassium phosphate (K_2HPO_4) QCT reference phantom (Model 3T; Mindways Software Inc, Austin, TX, USA) within each knee CT image to transform CT Hounsfield units (HU) to equivalent volumetric BMD (mg/cm^3 K_2HPO_4) (Figure 2-1-A). The five reference materials present within our phantom ranged between -50 and 375 mg/cm^3 K_2HPO_4, with higher density values linearly extrapolated using regression equations. We placed an ultrasound gel-filled bag between the specimens and the reference phantom to minimize air gaps, thereby limiting beam hardening effects and radiation scatter. We assessed the precision of CT-TOMASD measures by scanning eight knees in three different orientations, followed by complete CT-TOMASD analyses for each individual scan (24 separate analyses).

2.3.2.2 CT-TOMASD Image Analysis

2.3.2.2.1 BMD Conversion

We converted CT HU values to volumetric BMD using a custom-written algorithm (Matlab 2007a; MathWorks, Natick, MA, USA). Circular regions of interest were overlaid within each of the reference phantom cylinders, and mean HU values were recorded for all pertinent images (Figure 2-1-A). A linear regression equation ($r^2 > 0.99$) derived from the mean HU values and known reference cylinder densities was used to convert HU to equivalent volumetric BMD. Individual bone mineral density conversions were conducted for each individual axial image. We did not use a global conversion equation because we noted different HU-BMD conversion equations for the subchondral region, proximal epiphysis, and proximal metaphysis of the proximal tibia (likely due to beam hardening effects). For identical HU values, the different conversion equations provided densities differing by as much as 7.7% (average: 5.5%). Therefore, individual conversion equations were used for each individual CT image.

2.3.2.2.2 Segmentation

We segmented the proximal tibia using a combination of manual and semi-automated segmentation techniques with commercial segmentation software (Analyze8.1; Mayo Foundation, Rochester, MN, USA) (Figure 2-1-B). To guide the segmentation process, we determined optimal threshold values for defining the subchondral bone surface, for each individual knee, using the Half-Maximum Height (HMH) method [131, 132]. We determined HMH values for each individual knee because correct definition of the subchondral surface is difficult due to limited CT slice thickness capabilities (0.5 mm) and subsequent partial volume effects at the subchondral bone / articular cartilage interface. The HMH method defines an optimum threshold value for characterizing cortical periosteal surfaces using histogram line profiles of imaged density to determine the 50% density midpoint between low density

soft tissue (predominantly articular cartilage) and high density (subchondral) bone. The HMH value represents the density of a 3D voxel containing 50% soft tissue and 50% bone and acts as a minimum threshold value for voxels predominantly containing bone. To accelerate the segmentation process, we smoothed the QCT images using ITK open-source software (National Library of Medicine; http://www.itk.org) with the Binary Min/Max Curvature Flow filter (Iterations: 30, Time Step: 0.125, Radius: 1, Threshold: density of soft tissue previously found using HMH). This filter smoothed image noise while retaining edges such as the bone-cartilage interface, and reduced the manual segmentation time by ~50%. We then segmented the complete proximal tibia (superior tibial spine to tibial tuberosity) in the sagittal plane using region growing with manual correction. We controlled region growing segmentations using the HMH threshold value specific to each individual knee. Following region growing, we manually corrected the segmentations using an interactive touch-screen tablet (Cintiq 21UX, Wacom, Krefeld, Germany) to ensure that segmentations omitted osteophytes. Manual correction was also used to remove outliers at the bone surface, which helped ensure that the subchondral bone surface was represented as a smooth, consistent surface.

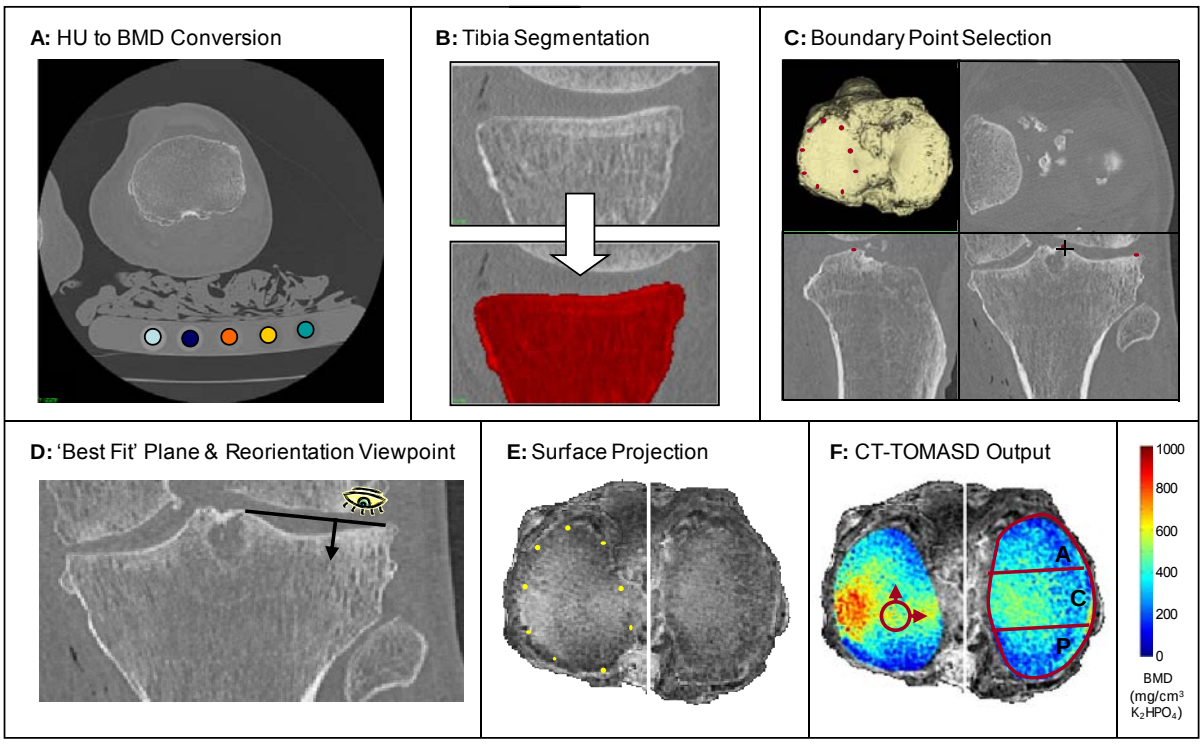

Figure 2-1. Methodological sequence for CT-TOMASD analyses of proximal tibiae consists of converting computed tomography (CT) grey-scale intensity to bone mineral density (BMD) using a quantitative CT (QCT) reference phantom (*A*), followed by semi-automatic tibial segmentation in the sagittal plane (*B*). Peripheral and inner boundary points are manually selected (*C*) to define the medial and lateral plateaus; with the proximal tibia reorientated relative to 'best fit' planes passing through plateau boundary points (*D*). A surface projection image processing algorithm is performed to map 3D subchondral density in relation to depth (measured from the subchondral surface) directly at the joint surface (*E*). CT-TOMASD regional analyses are performed, including the max BMD contained within a 10mm diameter focal region of interest and the average BMD contained within the anterior, central and posterior compartments of each plateau (*F*). Reprinted with permission from Elsiever.

2.3.2.2.3 Alignment

In order to minimize artifacts due to partial volume effects, CT-TOMASD surface projection analyses require the subchondral bone surface to be relatively flat and oriented approximately parallel with each projection image*. We addressed these requirements by realigning and reconstructing the imaged proximal tibia relative to best-fit planes fit to each medial and lateral plateau (Matlab 2007a). We

* Computational simulations (Appendix A) revealed that density artifacts associated with surface inclination are minimal (< 3% density overestimation) if inclination is less than 20°. If inclination is greater than 20°, density artifacts linearly increase to 17% density overestimation at 40° inclination.

derived the best-fit planes from manually selected boundary points which outlined prominent anterior (n=1) and posterior (n=1) points, the outer periphery (n=5), and inner region (n=5) of each plateau (Figure 2-1-C). We used commercial software (Analyze 8.1) to manually select the 3D points from sagittal, coronal and axial CT images. Three of the 5 inner region points were located on the tibial spine at approximately 50% of the height from the flattest region of each plateau to the superior tip of the tibial spine. For each plateau, we used singular value decomposition (Matlab 2007a) to match selected boundary points with best-fit planes (Figure 2-1-D). We then realigned and reconstructed (cubic interpolation) imaged proximal tibiae and segmentations relative to the respective medial and lateral plateaus (Matlab 2007a). The medial-lateral axis served as the x-axis, which was defined using the prominent anterior points of each plateau.

2.3.2.2.4 Surface Projection

Beginning at the superior segmented joint surface, we averaged proximal tibial bone density in increments of 0.5 mm to a depth of 6.5 mm beyond the defined segmented subchondral surface. We projected average density to a 2D image to create a surface projected CT-TOMASD rendered image of subchondral BMD, expressed in relation to depth from the subchondral surface (Figure 2-1-E). We then semi-automatically segmented the 2D projection images of the medial and lateral plateaus using natural cubic splines fit to the previously selected boundary points (Matlab 2007a) while permitting manual adjustment of knot points (Figure 1E). Care was taken to ensure that the segmented 2D regions did not overlay high density cortical edges of the proximal tibia, the tibial spine or osteophyte locations. The average areas of the medial and lateral segmentations were 11.22 and 10.75 cm^2, respectively.

2.3.2.2.5 Normalization

To account for differences in physical size and allow for subject-to-subject comparisons, we controlled the depth measure for each subject using relative tibial volume and plateau areas and a user-defined normalized depth (i.e., 5 mm). We calculated proximal tibial volume superior to the lateral inferior ridge of the proximal fibular head (repeatable landmark) after aligning the tibia in a neutral physiologic orientation (tibial plateau angled posteriorly 10° in sagittal plane; tibial long axis vertically oriented in coronal plane). We determined subject- specific depths using the following equation:

$$\frac{d_{ss} \cdot area_{ss}}{d \cdot \overline{area}} = \frac{volume_{ss}}{\overline{volume}}$$

Solving for d_{ss}:

$$d_{ss} = \frac{d \cdot \overline{area}}{\overline{volume}} \cdot \frac{volume_{ss}}{area_{ss}}$$

where d_{ss} is the actual subject-specific depth corresponding to the user-defined normalized depth, d is the desired user-defined normalized depth (i.e., 5 mm), $\overline{area}$ is the mean plateau area (both medial and lateral) for all subjects, $\overline{volume}$ is the mean volume of all subjects, $volume_{ss}$ is the subject-specific proximal tibial volume, and $area_{ss}$ is the subject-specific plateau area of both medial and lateral plateaus. For this analysis, we selected normalized depths of 2.5 and 5.0 mm for density analyses. Average density values were computed as the average of a series of 0.5 mm incremental 2D surface projection images, starting at the superior surface and ending at the specific normalized depth. Fractional depths (i.e., 4.7 mm) were computed by incorporating the percentage of a specific distal surface projection (i.e., for above case; 0.2 multiplied by the surface projection corresponding to 4.5 - 5.0 mm depth).

The volume normalization measure was selected in place of linear measures (e.g., proximal tibial medial:lateral and anterior:posterior widths) because the volume measure offered greater repeatability (0.5% vs 1.4% for linear measures), smaller differences between left:right paired knees

(1.9% versus 2.5% for linear measures), and was less influenced by landmark uncertainties due to osteophyte presence. The area measure offered similarly small repeatability errors (2.2%). Therefore, the combination of tibial volume and area served as a conservative normalization measure with nominal uncertainties due to disease severity.

2.3.2.2.6 Regional Analyses

We performed a series of regional analyses on each projection image (2.5 and 5.0 mm depths), including: (a) Total average BMD of both the medial and lateral plateaus combined, (b) average BMD of each plateau, (c) Anterior / Central / Posterior compartment BMD, assessed by dividing the plateaus into three equal height compartments portioned relative to the anterior/posterior width of each plateau, (d) medial:lateral BMD ratio and (e) average BMD of a 10 mm diameter core or 'focal spot' which searched each plateau for a maximum value (Figure 2-1-F). We included focal analyses to locate small regions of high density bone possibly masked by whole compartment analyses. The 10 mm diameter size was selected because it provided the smallest region of interest with the highest precision (CV%: 4.2%) when compared against 5 mm (9.74%), 7.5 mm (6.13%), and 15 mm (4.7%) diameter regions of interest.

2.3.3 OA Assessment

Each knee was assessed for OA severity using a variation of the original Kellgren-Lawrence (KL) scoring system [57] from axial, coronal and sagittal CT reconstructions and fluoroscopic radiography (Table 2-1). Our modified Kellgren-Lawrence (mKL) system was primarily based upon radiographic evidence of osteophytes and sclerosis with minimal consideration of joint space narrowing. Measures of joint space width, which are unreliable from non-weight bearing images, were not considered unless near bone-on-bone contact was observed. OA assessments were performed by a qualified orthopaedic

surgeon (Dr. Bassam Masri) who routinely performs Kellgren-Lawrence grading of OA knees. We subdivided the subjects into three OA categories: normal (mKL = 0), early-OA (mKL = 1,2) or late-OA (mKL = 3,4). The participating orthopaedic surgeon provided an estimation of varus/neutral/valgus knee alignment from CT images based upon knee orientation, presence of joint space narrowing, near bone-on-bone contact and ligament soft tissue laxity.

Table 2-1. Kellgren Lawrence [57] grading of radiographic OA.

Grade	Property
0	Normal, no osteophytes
1	Possible osteophytic lipping
2	Definite osteophytes; possible joint space narrowing
3	Moderate or multiple osteophytes; definite joint space narrowing; some sclerosis and possible bony attrition
4	Large osteophytes; marked joint space narrowing; severe sclerosis and definite bony attrition

2.3.4 Precision and Comparative Analysis

We assessed the precision of CT-TOMASD measures using three separate assessments for eight specimens by root-mean-square coefficients of variation (CV%), according to procedures outlined by Glüer et al [133]. Precision was assessed for measures of HMH values, proximal tibia volume, subchondral surface area, and average BMD values. Due to the methodological and descriptive nature of this study, combined with a limited sample size, statistical analyses gauging the validity of observed differences between OA and normal knees were largely avoided. For large sample sizes (≥10), we provided basic descriptive statistics with data expressed as mean ± standard deviations (SD). We evaluated isolated differences between OA and normal knees using standard z-scoring, which presents differences as the number of SD above or below normal mean values. We performed sample size calculations (alpha level = 0.05, power = 0.90) to determine the sample sizes necessary for a full-scale

study to detect significant differences in subchondral bone density between OA and normal tibiae. We performed sample size calculations for early-OA and OA (pooled early- & late-OA) groups using peak focal density as the primary outcome variable. We also performed effect size calculations using peak focal density as the primary outcome variable. We report effect sizes using Cohen's *d* [134]. For context, we considered a Cohen's *d* above 0.8 to be a large effect size [134] with statistical/clinical significance [135].

2.4 Results

2.4.1 Methodological Precision

Precision errors associated with the CT-TOMASD methodology were small. Coefficients of variation were 2.8% for HMH values, 2.3% and 2.1% for the medial and lateral surface area measures, respectively, and 0.5% for the proximal tibia volume measure. Precision errors for CT-TOMASD measurement of bone density were also small (Table 2-2). Coefficients of variation for mean BMD in the entire medial and lateral tibial plateaus were about 1.5%, and regional analyses reached a maximum CV% of 3.5%.

Table 2-2. Precision results for the CT-TOMASD analysis expressed as CV%.

Depth	M&L	Medial Plateau					Lateral Plateau					M:L
(mm)	Total	Total	Ant	Cent	Post	Focal	Total	Ant	Cent	Post	Focal	Ratio
2.5	1.1	1.1	2.5	1.2	3.0	1.6	1.8	3.5	1.9	3.0	1.3	1.9
5.0	0.9	1.0	2.3	1.1	2.5	1.5	1.1	2.8	2.1	3.5	1.2	1.9

2.4.2 OA versus Normal Subchondral Bone Density

OA was identified in eight compartments of six knees using CT, including two cases of late OA (OA1 & OA2) and four cases of early OA (OA3-OA6). CT images demonstrated that knee OA1 (mKL = 3) was in valgus alignment and showed osteophytes and sclerosis in the lateral compartment and osteophytes

in the medial compartment. Knee OA2 (mKL = 3) was in varus alignment and showed medial sclerosis and osteophyte presence. Knee OA3 (mKL = 1-2) was in neutral alignment and showed osteophytic lipping in the anterior lateral compartment and possible lipping in the anterior medial compartment. Knee OA4 (mKL = 1) was in neutral alignment and demonstrated medial lipping. Knee OA5 (mKL = 1) was in neutral alignment and showed lipping in the medial and lateral compartments. Knee OA6 (mKL = 1) was in neutral alignment and demonstrated lipping in the medial posterior compartment. Only one case of late OA (mKL = 3) was identified using fluoroscopic imaging (Knee OAI). Nine cases of possible early OA (mKL = 1) were identified using fluoroscopy with three closely matching CT-based mKL characterizations (Knees OA3, OA4 & OA6). The remaining ten knees were categorized as normal (mKL = 0).

Substantial qualitative differences were noted between the osteoarthritic and normal knees at both the normalized 2.5 mm and 5.0 mm depths (Figures 2.2 and 2.3). In general, the bone in normal knees was most dense anteriorly/centrally in the medial compartment and posteriorly/centrally in the lateral compartment. These patterns were not observed in the early- and late-OA subjects, who tended to have more high dense bone than normal knees (Figures 2.2 and 2.3).

Regional analyses demonstrated large quantitative differences between normal and OA knees, particularly for the 5.0 mm depth with the late-OA knees (Table 2.3). The M:L BMD ratio—a measure related to OA disease severity [21, 24] and varus/valgus alignment [24]—was 1.19 in normal knees while OA1 demonstrated a M:L BMD Ratio of 0.77, which was 4.9 SD lower than normals. The focal spot in knee OA1 was 4.7 SD higher than normals.

At the 5 mm depth the varus aligned knee OA2 demonstrated a M:L BMD Ratio 3.1 SD higher than normals. The focal spot at this depth was 3.3 SD higher than normals. Similar differences were noted at the 2.5 mm depth between knees OA1 and OA2 with the normal knees, but the differences were not as pronounced.

Early-OA knee OA3, which was in neutral alignment, demonstrated a similar M:L BMD ratio to normal knees at both the 2.5 and 5.0 mm depths, as well as a similar peak focal density at the 5.0 mm depth. The peak focal analysis at the 2.5 mm depth, however, revealed a BMD 3.5 SD higher than normals and higher than both late-OA knees. Knees OA4 through OA6 demonstrated moderately higher M:L BMD ratios and peak focal densities when compared with normals, though less pronounced than other OA knees.

Statistical power analyses (α = 0.05, power = 0.90) using peak focal densities estimated that six subjects, per group, are required to differentiate between OA (pooled early- & late-OA) and normal tibial subchondral bone density. Eight subjects, per group, are however required to differentiate between early-OA and normal knees. Cohen's *d* effect sizes ranged from 1.6 (early-OA & normals) to 4.3 (late-OA & normals).

Table 2-3. Average bone mineral density measures (K_2HPO_4) in osteoarthritic and normal cadaver knees. Mean and standard deviations (SD) reported for the ten normal subjects. Results pertain to average density measures across depths of 2.5 and 5.0 mm, measured relative to the defined subchondral surface. Regional analyses were performed for the total average density of both the medial and lateral plateaus, each individual plateau, anterior/central/posterior regions of each plateau, and a 10 mm diameter 'focal density which searched each plateau for a maximum average density contained within the 'focal' region of interest.

Depth		M&L	Medial Plateau				Lateral Plateau				M:L	Focal
(mm)		Total	Total	Ant	Cent	Post	Total	Ant	Cent	Post	Ratio	Spot
2.5	OA1	454	408	363	467	373	505	435	617	420	0.81	796L
	OA2	435	498	415	577	474	369	259	440	370	1.35	755M
	OA3	414	421	427	502	266	408	260	473	431	1.03	806L
	OA4	394	438	493	502	282	348	265	403	344	1.26	631M
	OA5	426	464	476	549	336	375	336	407	369	1.24	690M
	OA6	404	455	476	529	310	345	330	376	318	1.32	633M
	Norm	356	411	383	449	262	332	264	381	329	1.14	579
	n=10	(55)	(46)	(65)	(61)	(52)	(57)	(47)	(69)	(69)	(0.08)	(64)
5.0	OA1	370	324	275	380	297	420	348	536	330	0.77	727L
	OA2	325	383	312	439	381	263	181	308	273	1.46	641M
	OA3	302	307	313	359	203	298	209	338	309	1.03	531L
	OA4	315	353	397	400	234	278	226	314	270	1.27	494M
	OA5	368	404	417	474	296	318	295	342	308	1.27	577M
	OA6	344	389	405	449	273	291	282	317	265	1.34	516M
	Norm	283	306	310	359	219	260	219	294	251	1.19	450
	n=10	(49)	(49)	(56)	(54)	(49)	(50)	(41)	(61)	(58)	(0.09)	(58)

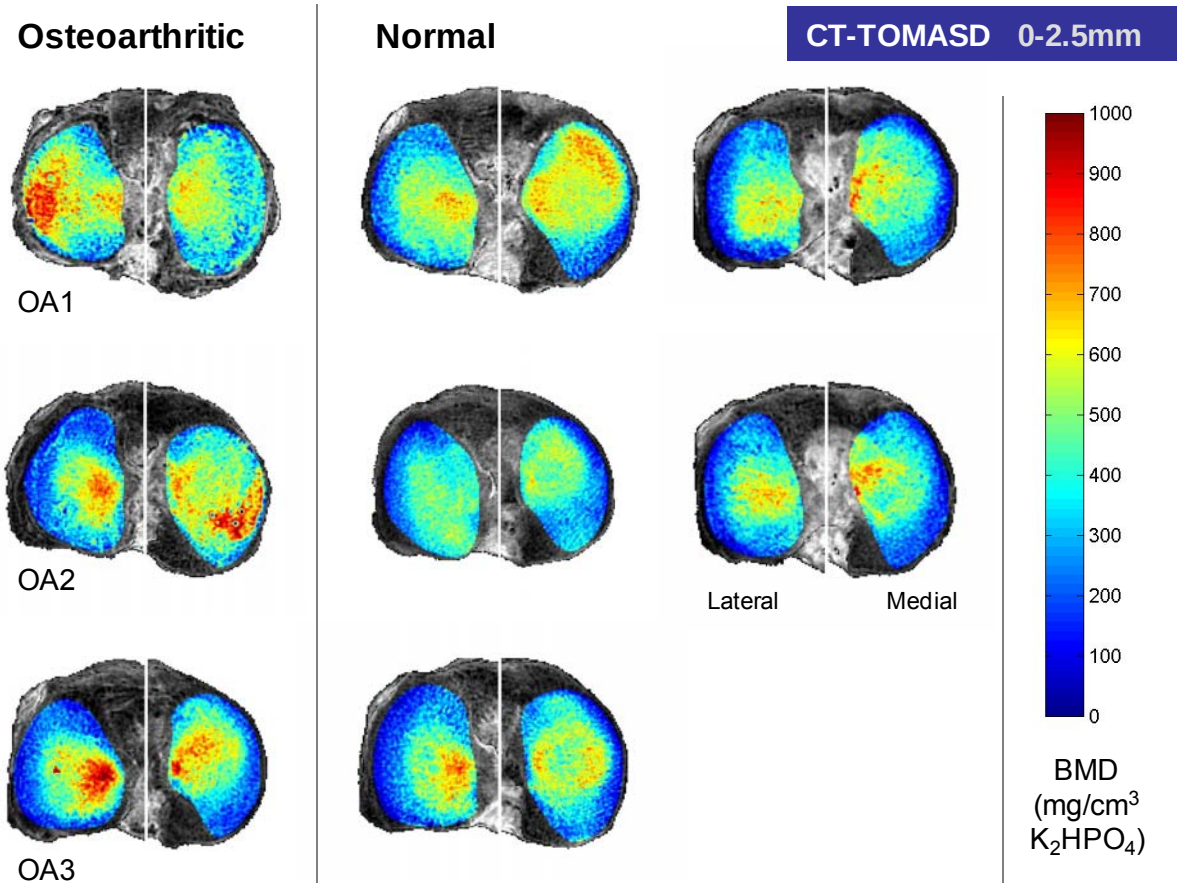

Figure 2-2. CT-TOMASD topographic density maps of proximal tibial subchondral bone using the surface projection image processing technique, assessed across a depth of 2.5mm from the subchondral surface. Results are displayed for two cases of late OA (valgus-aligned lateral OA1, varus-aligned medial OA2), one case of early OA (neutral-aligned lateral OA3), and five asymptomatic subjects displaying no radiographic evidence of OA. All knees are displayed as left knees for comparative purposes.

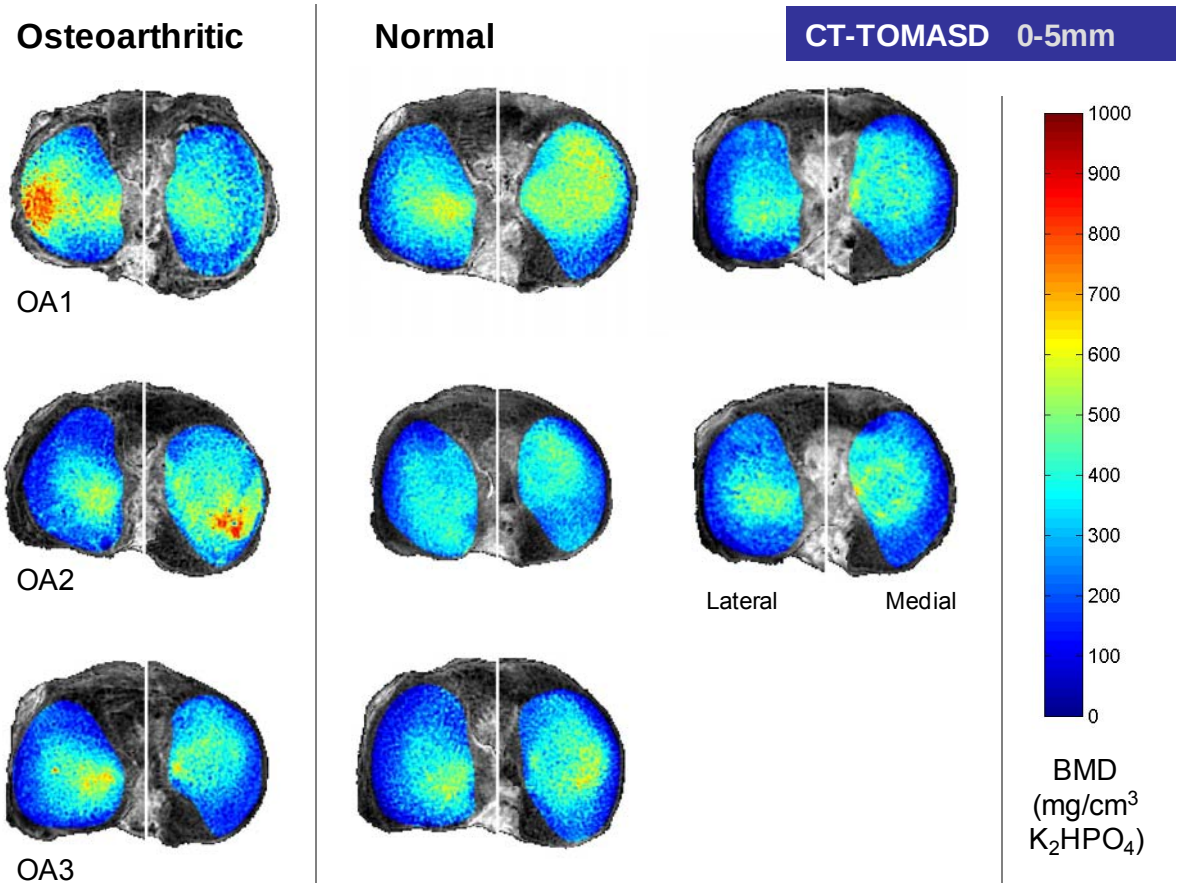

Figure 2-3. CT-TOMASD topographic density maps of proximal tibial subchondral bone using the surface projection image processing technique, assessed across a depth of 5.0mm from the subchondral surface. Results are displayed for two cases of late OA (valgus-aligned lateral OA1, varus-aligned medial OA2), one case of early OA (neutral-aligned lateral OA3), and five asymptomatic subjects displaying no radiographic evidence of OA. All knees are displayed as left knees for comparative purposes.

2.5 Discussion

CT-TOMASD measures 3D BMD to specified depths from the subchondral surface, with repeatability errors smaller than the variance in the normal population sample. The high precision is due to the 3D isotropic nature of the method, and the ensuing ability to reconstruct the imaged tibia dataset in various orientations. Using small isotropic voxel sizes, combined with digitized points defining the periphery and inner regions of the medial and lateral plateaus, the effects of patient positioning are minimized. These *ex vivo* precision results are important because they suggest that CT-TOMASD has potential usage for characterizing subchondral bone density with minimal concern that observed density changes, or differences between OA and normal knees, are due to imaging artifacts as opposed to disease processes. However, before initiating large-scale studies of subchondral bone density in people living with OA, *in vivo* precision measurement is still required to assess uncertainty associated with subject motion.

A key advantage of CT-TOMASD is its ability to image thin layers near the joint surface. This is important because there may be a variable density transition zone located somewhere between the higher density subchondral bone and lower density trabecular bone found with OA subjects. While it is accepted that both the subchondral endplate and nearby trabeculae increase in thickness and density with OA, trabeculae located more distal to the surface decrease in density—possibly due to structural 'stress shielding' by high density bone near the subchondral surface [73]. FSA studies have shown that horizontal and vertical trabeculae in regions distal to the subchondral bone surface are thinner (i.e., bone is less dense) than in knees without OA [93, 95, 136]. Similarly, animal studies simulating secondary OA have shown decreases in periarticular trabecular bone density which precede thickening of the subchondral plate [137, 138]. Based on our results and previous findings we estimate this transition zone to be between 2.5 and 5.0 mm from the subchondral surface [19, 90].

CT-TOMASD addresses some of the limitations of the DXA and QCT methods that have been used to study BMD near the joint. A key limitation of DXA is that it represents any 3D bony structure as a 2D projection image; making it prone to errors due to patient positioning and physical size. DXA studies of BMD at the knee have used a range of different sized ROIs at various locations, typically positioned away from the subchondral surface (> 10mm) or too large to obtain useful spatial information. A ROI containing both subchondral cortical bone and distal trabeculae likely contains bone experiencing both increased and decreased density; possibly cancelling one another and imaged BMD increases (or decreases) with OA are subsequently missed. Past QCT studies of subchondral bone have predominantly used a 1-4 mm slice thickness [113-115, 139-142], possibly leading to significant partial volume effects at the subchondral bone/cartilage interface and within the thin subchondral cortical bone. Usage of a large slice thickness also limits accurate data reformatting due to the large voxel size, which may lead to repeatability errors due to patient positioning. Large slices thicknesses (and related voxel sizes) may also result in a diminished ability to capture small changes associated with OA, particularly longitudinal changes occurring over short periods of time. These limitations are largely omitted with our imaging technique due to the usage of a 0.5 mm isotropic voxel size, currently one of the smallest clinically available isotropic voxel sizes.

Study parameters were chosen to minimize radiation dosage while permitting usage of a small isotropic voxel size and QCT reference phantom. Voxel size is dependent both upon CT slice thickness capabilities and the physical dimensions of the QCT reference phantom, which must be contained within each knee image. We chose the smallest available isotropic voxel based upon slice thickness capabilities of the CT machine. Single-energy QCT was utilized instead of dual-energy QCT due to the lower radiation dosage. Due to the low presence of radiosensitive tissues at the knee joint the effective dosage using the CT-TOMASD analysis is about 0.15 mSv, estimated from scan parameters (17 mGy CTDIvol dosage, 15 cm length, 255 mGy*cm dose length product) using shareware software (CT-

DOSE; National Board of Health, Herley, Denmark). CT-TOMASD dosages are comparable with Henckel et al [103], who calculated an effective dosage of 0.12 mSv at the knee joint using similar CT scanning parameters. This compares with an exposure of approximately 0.05 mSv during a transatlantic flight from Europe to North America [105], and 0.7 mSv [106, 107] for an anterior-posterior pelvic radiograph or long-leg standing radiograph.

The CT-TOMASD imaging method has possible sources of error related to partial volume effects, the selected reference phantom, the choice of single-energy QCT, surface curvature, and analysis time. First, partial volume effects are high both at the subchondral surface—due to the high density gradient between articular cartilage and subchondral bone—and through the thin subchondral cortical bone. We minimized these effects by using the smallest clinically available slice thickness (0.5 mm) and characterized the subchondral surface using patient-specific HMH threshold values combined with manual segmentation correction for each individual sagittal CT image. Second, the reference phantom used in this study was not designed for subchondral or cortical density measurements, and density values higher than those in the reference phantom were linearly extrapolated using regression equations ($r^2 > 0.99$). Phantoms containing higher density reference materials increase imaged sensitivity to x-ray scatter and beam hardening artifacts; therefore phantoms similar to ours have been widely used for the evaluation of subchondral bone [139-142]. Third, a source of error using single-energy QCT is the variable content of red marrow and marrow fat contained within trabecular bone, leading to underestimates of BMD [143-145]. However, since marrow fat content increases with age and OA subjects are from older populations, we assume that marrow content in OA subjects will show low variability and subsequent minimal associated error. Although dual-energy QCT minimizes marrow fat error and improves BMD accuracy, the technique has poorer *in vivo* precision and a higher radiation dosage than single-energy QCT [144], making single-energy QCT the favourable option [144-146] for CT-TOMASD analyses of proximal tibial bone density. Fourth, due to the 2D projection nature of CT-

TOMASD, excessive surface curvature could lead to incorrect density measures (Appendix A). This is because CT-TOMASD projection analyses require the subchondral bone surface to be oriented approximately parallel with the projection plane to obtain density measures representative of 'true' density. At inclined surfaces, density is measured along vectors obliquely aligned with the subchondral surface, leading to overestimations of true density. The technique is therefore best suited for subchondral sites such as the proximal tibia which display a relatively low degree of curvature. We attempted to minimize the effects of surface curvature by reconstructing and reorienting the imaged proximal tibia relative to best-fit planes fit to each medial and lateral plateau. After reorientation and reconstruction, curvatures across medial and lateral plateaus were generally low (< 5^{o}) but could reach maximum values of 20^{o} along the periphery and 40^{o} near the tibial spine. Computational simulations (Appendix A) revealed that artifacts associated with these maximum inclinations can lead to moderate-to-large overestimations of density (periphery: < 12%; tibial spine: < 17%). However, density measures from the periphery and tibial spine are lower in magnitude than measures from central regions of each plateau. Density measures from the periphery and tibial spine also account for a portion of total compartment BMD, resulting in "worst case scenario" increases in total compartment BMD of < 4%. The focal measure, on the other hand, could be moderately affected by inclination artifacts. However, instances of inclination along the periphery and tibial spine were typically less than 10^{o} and 30^{o}, respectively. Errors associated with these inclinations would result in small overestimations of density (periphery: < 5%; tibial spine: < 8%). For these reasons we believe the overall effects of curvature on CT-TOMASD measures are small. Fifth, the entire CT-TOMASD analysis for each knee takes 30-45 minutes to complete. The most time intensive portion of the procedure pertains to the segmentation process, which occupies ~80% of the analysis time. The remaining time pertains to loading and converting CT images to BMD images (~15% of analysis time) and the CT-TOMASD analysis (~5% of

analysis time). We are presently developing new tools to automate the segmentation procedure, aiming to reduce the analysis time to 10-15 minutes per knee.

Lastly, the accuracy of CT-TOMASD measures of BMD requires consideration. CT-TOMASD measures are obtained using QCT, a validated technique used to assess trabecular, cortical [147, 148], and subchondral BMD [28, 113-115, 139-142]. Since a QCT reference phantom of *known* bone mineral densities is contained within each image, direct conversions from image intensity to physical density can be made. Human and animal studies have verified that QCT density measures are accurate representations of true BMD [141, 144, 149-153]. The BMD accuracy of an individual voxel, or a thin structure less than 2mm thick, is however questionable [154-156]. Importantly, analyses which average numerous individual density measures contained within large ROIs do not necessarily suffer these inaccuracies [156]. While it is probable that QCT density is inaccurately represented at the subchondral surface due to partial volume effects, our usage of relatively large ROIs (~1700 voxels within 10mm peak core, 2.5mm depth) are expected to minimize such inaccuracies. Further, the use of identical imaging parameters (same CT machine, settings, operator, QCT reference phantom, image analysis technique) does permit comparisons between OA and normal knees as we have shown a high precision for all CT-TOMASD measures.

2.6 Conclusions

We have developed a precise 3D imaging technique which measures subchondral BMD in relation to depth from the subchondral surface, projecting results to a 2D topographical density map directly at the joint surface. Our preliminary results demonstrate qualitative and quantitative differences and large effect sizes between OA and normal knees. This method has the potential to identify and quantify changes in subchondral BMD that may be associated with OA disease progression.

3 Comparison of CT-OAM and CT-TOMASD

3.1 Synopsis

This chapter describes our comparisons of the proficiency of CT-TOMASD layer analyses to CT-OAM maximum intensity projections for distinguishing OA from normal proximal tibial bone density patterns. This chapter also describes technical and methodological differences between the two imaging methods. Both CT-TOMASD and CT-OAM identified higher medial compartment density in OA tibiae compared with normal tibiae. CT-TOMASD identified focal density differences between normal and OA knees.

3.2 Introduction

The few applications of QCT to subchondral bone imaging have used CT-OAM to characterize subchondral bone density [111, 113]. CT-OAM employs maximum intensity projection image processing to identify the highest (maximum) density within the subchondral bony region. The only reported application of CT-OAM to quantify subchondral bone density distribution in OA joints was in the patella [117]. CT-OAM has not yet been used to identify subchondral bone density differences between OA and normal proximal tibiae.

We recently developed the novel imaging tool CT-TOMASD to characterize OA and normal subchondral bone density. Our preliminary analyses of OA and normal proximal tibiae characterized, but did not compare, average subchondral bone density from the subchondral surface to defined depths (i.e., 0–2.5, 0–5 mm) [157]. We have further developed CT-TOMASD to measure density across depth-specific 'layers' (e.g., 0–2.5, 2.5–5, 5–10 mm) from the subchondral surface.

It is currently unknown whether CT-OAM maximum intensity analyses and CT-TOMASD 'layer' analyses detect comparable differences in subchondral bone density between OA and normal proximal tibiae. The objective of this current study was to compare the proficiency of CT-TOMASD layer

analyses to CT-OAM maximum intensity projections for distinguishing OA from normal proximal tibial bone density patterns.

3.3 Methods

3.3.1 Specimens

For this study we used the same cadaver knees described in the previous study (Chapter 2).

3.3.2 OA Assessment

We pooled together all six knees previously classified as OA since all six exhibited signs of medial OA (five mKL=1; one mKL=3; age: 76.7 ± 6.5 years). Two of these six knees with medial OA also exhibited lateral OA with similar severity (one ML mKL=1; one ML mKL=3). The remaining ten knees were classified as normal (mKL=0; age: 77.7 ± 7.2 years).

3.3.3 Imaging Methodology

We previously described the CT-TOMASD methodology in detail (Chapter 2). For this study, we used the same QCT images and segmentations from the previous study (Chapter 2). The new features of CT-TOMASD, along with differences between CT-OAM and CT-TOMASD are described in the subsequent sections.

3.3.3.1 CT-OAM: Maximum Intensity Projection Analysis

Using previously described QCT images and segmentations (Chapter 2), we performed CT-OAM maximum intensity projection analyses [111, 113] by selecting the highest (maximum) density voxels within the subchondral bone to a depth of 10 mm from the subchondral surface (Figure 3-1). The subchondral region contained subchondral cortical, subchondral trabecular and epiphyseal trabecular

bone. CT-OAM selected the highest density voxel within each (parallel) ray originating at the subchondral surface (Matlab 2007a). Each parallel ray contained a column of 3D voxels (10.0 mm length, 20 voxels) oriented perpendicular to the medial or lateral plateau. We projected the maximum density of each ray to a 2D image to create a CT-OAM rendered image of subchondral BMD (Figure 3-1). The medial and lateral plateau regions in the 2D CT-OAM images were then segmented using natural cubic splines fit to the previously selected boundary points (Matlab 2007a). The splines were manually adjusted to ensure that the segmented 2D regions did not overlap high density cortical edges of the proximal tibia, tibial spine, or osteophyte locations.

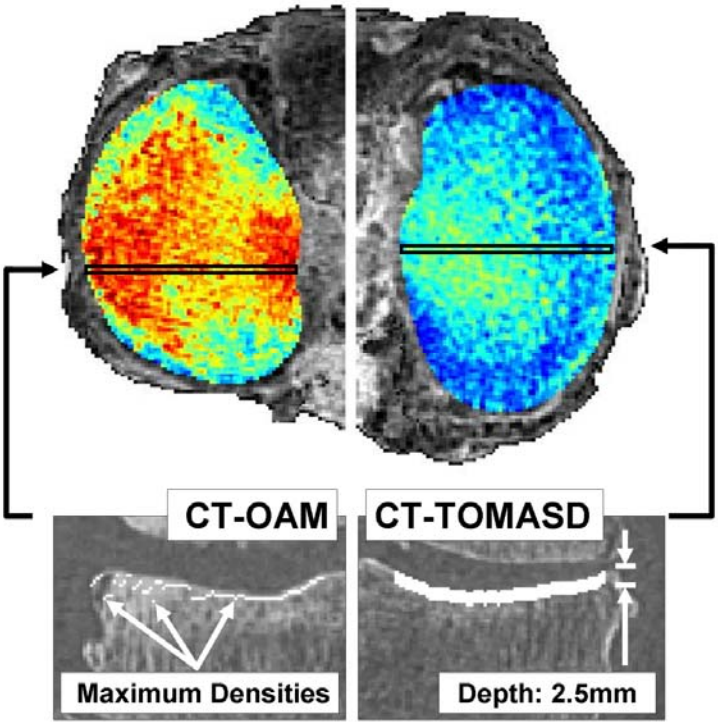

Figure 3-1. Demonstration of how the CT-OAM and CT-TOMASD image processing techniques function. CT-OAM selects maximum subchondral bone densities contained within the subchondral bony region, ignoring less dense bone located above or below the maximum BMD, and projects maximum density results to a 2D maximum intensity projection image (left). CT-TOMASD averages subchondral bone densities across depths originating from the subchondral surface (e.g., 0-2–5 mm layer) and projects average density results to a 2D surface projection image (right).

3.3.3.2 CT-TOMASD: Depth-Specific 'Layer' Analysis

We performed the CT-TOMASD depth-specific 'layer' analysis by averaging density across three layers (0–2.5, 2.5–5 and 5–10mm) measured in relation to depth from the subchondral surface (Matlab 2007a). CT-TOMASD averages portions of each previously described parallel ray (Matlab 2007a). We projected average density of portions of each ray to a 2D image to create a surface projected CT-TOMASD rendered image of subchondral BMD, expressed in relation to depth from the subchondral surface (Figure 3-1). To account for differences in physical size, we controlled the depth measure for each subject using relative tibial volumes and plateau areas and a user-defined normalized depth. We used the same 2D segmentations of the medial and lateral plateaus for both CT-OAM and CT-TOMASD analyses.

3.3.3.3 Regional Analyses and Precision

We performed a series of regional analyses on each projection image, including: (a) Medial plateau BMD; (b) Lateral plateau BMD; and (c) average BMD of a 10 mm diameter area or 'focal spot' which searched each medial and lateral plateau for the highest focal density present within each knee. Regional analyses were performed for each CT-OAM maximum intensity image and each of the three CT-TOMASD depth-specific layer images (0–2.5, 2.5–5 and 5–10 mm). We assessed the precision of CT-TOMASD and CT-OAM density measures by re-analyzing eight cadaver knees with repositioning and rescanning each knee three times.

3.3.4 Statistical Analysis

We report mean and standard deviation (SD) for density outcomes for both CT-TOMASD and CT-OAM. Precision errors were assessed using coefficients of variation (CV%) according to Glüer et al [133]. We verified equality of variances with Levene's test and normality of data distribution with Q-Q plots.

We tested the statistical hypothesis that subchondral bone density was higher in OA knees than in normal knees using simple contrasts (OA vs. normal) with generalized linear model (GLM) for each type of density analysis (CT-OAM and CT-TOMASD at each depth). We included group (OA vs. normal) as a fixed factor. Age was included as a covariate. We selected Bonferroni method to adjust for multiple comparisons. We report pair-wise contrasts with corresponding 95% confidence intervals (CI) to identify the method, depth, and region of the between-group differences. For all tests, we considered an α-level less than 5% ($p < 0.05$) statistically significant. Statistical analyses were performed using commercial software (Matlab 2007a and SPSS 15.0; SPSS Inc, Chicago, I L, USA).

3.4 Results

CT-OAM demonstrated 17% greater whole medial compartment density in OA than normal knees (mean difference: 95 mg/cm^3; 95% CI: 21–169 mg/cm^3, p=0.016) (Table 3-1, Figure 3-2). No density differences were noted in the lateral compartment or with focal regional analyses using CT-OAM. Precision errors associated with CT-OAM varied from 1.6–2.3% (Table 3-1).

CT-TOMASD showed an average 17% greater whole medial compartment density in OA knees than normal knees across the 0–2.5 mm layer (mean difference: 66 mg/cm^3; 95% CI: 16–117 mg/cm^3, p=0.014) (Table 3-1, Fig. 2). No density differences between OA and normal knees were noted in the medial compartment at the 2.5–5 and 5–10 mm layers. Similarly, no differences were observed in lateral compartment densities between OA and normal knees across all depths from the subchondral surface. Focal regional analyses revealed 24% greater density in the 0–2.5mm layer (mean difference: 139 mg/cm^3; 95% CI: 58–220 mg/cm^3, p=0.003) and 36% greater density in the 2.5–5 mm layer in OA knees when compared with normal knees (mean difference: 142 mg/cm^3; 95% CI: 13–272 mg/cm^3, p=0.034). Focal density did not differ between the groups at the 5–10 mm layer. Precision errors associated with CT-TOMASD varied from 1.1–4.2% (Table 3-1).

Table 3-1. Mean ± standard deviation (SD) measures of bone mineral density (BMD) in osteoarthritic and normal cadaver knees using the CT-OAM and CT-TOMASD imaging techniques. CT-OAM selects maximum subchondral bone densities contained within the subchondral bony region. CT-TOMASD averages subchondral bone densities across depths originating from the subchondral surface (e.g., 0–2.5 mm layer).

			BMD (mg/cm^3 K_2HPO_4)		Precision (%)
			Osteoarthritis (n=6)	Normal (n=10)	Normal + OA (n = 8, 3x)
Region	Method		Mean ± SD	Mean ± SD	CV%
Medial plateau	CT-OAM	Maximum	663 ± 45	564 ± 82	1.6
	CT-TOMASD	0-2.5mm	447 ± 33	378 ± 55	1.1
		2.5-5mm	335 ± 67	291 ± 55	1.1
		5-10mm	197 ± 55	164 ± 38	2.0
Lateral plateau	CT-OAM	Maximum	604 ± 98	520 ± 91	1.7
	CT-TOMASD	0-2.5mm	392 ± 60	333 ± 57	1.8
		2.5-5mm	284 ± 74	233 ± 55	1.9
		5-10mm	171 ± 49	144 ± 36	2.3
Focal spot	CT-OAM	Maximum	996 ± 112	883 ± 113	2.3
	CT-TOMASD	0-2.5mm	719 ± 78	580 ± 64	1.6
		2.5-5mm	541 ± 167	390 ± 94	3.6
		5-10mm	279 ± 120	216 ± 44	4.2

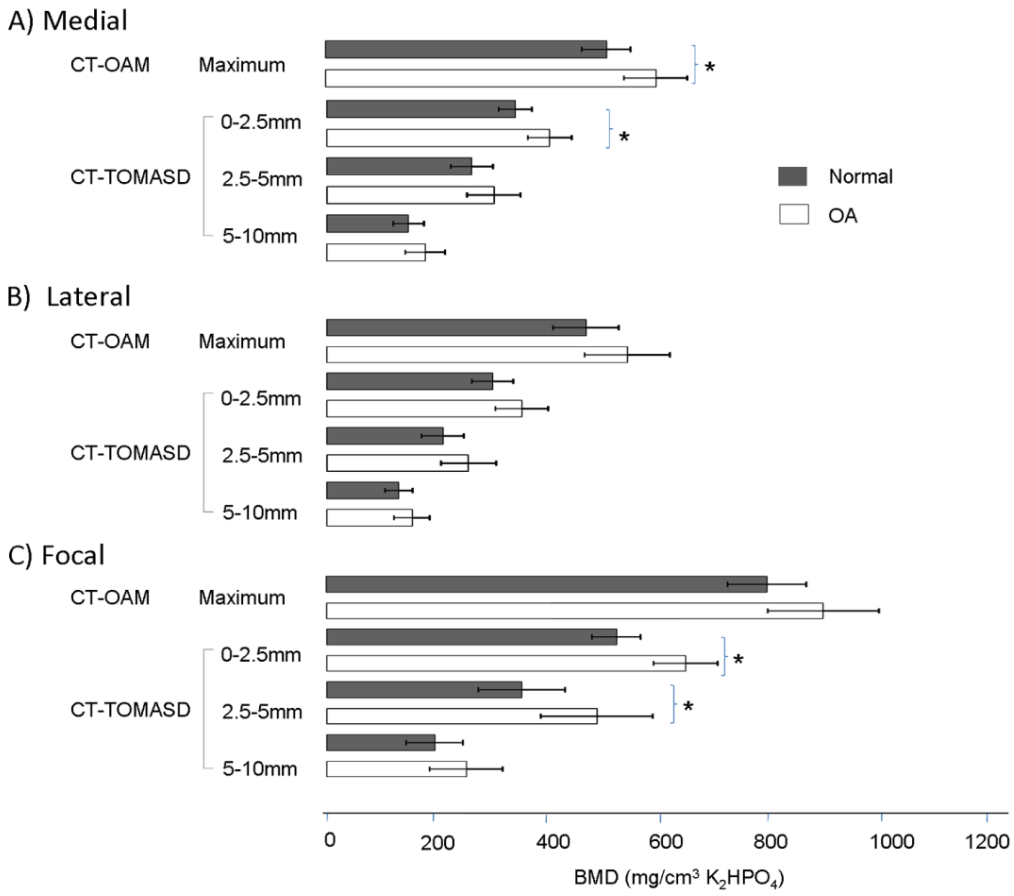

Figure 3-2. Region-specific (medial, lateral, and focal) comparison of subchondral densities using CT-OAM (maximum density) and CT-TOMASD (average density across depths from subchondral surface). Normal knee BMD is expressed with solid bars; OA knee BMD is expressing with open bars. Error bars represent 95% Confidence Intervals.

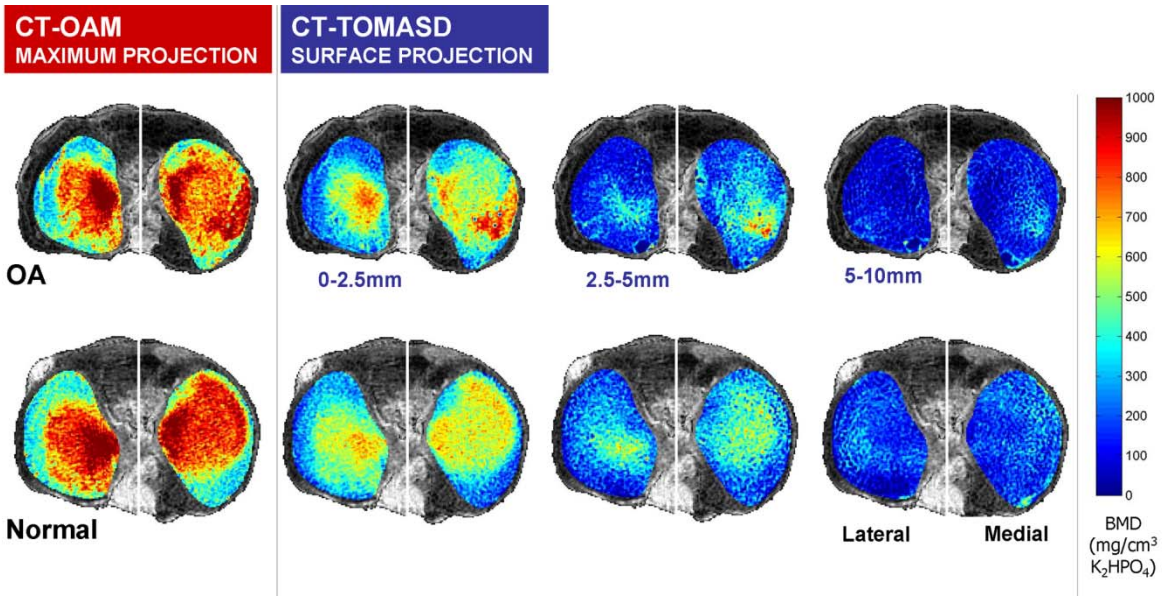

Figure 3-3. Density maps of proximal tibial subchondral bone using CT-OAM, which assess maximum density contained within subchondral bone, and CT-TOMASD, which averages density in relation to depth from the surchondral surface (e.g., 0-2.5mm depth). Results are displayed for 1 knee demonstrating medial OA and 1 normal knee demonstrating no radiographic OA evidence.

3.5 Discussion

This study is the first to report differences in subchondral bone density distributions between normal and OA cadaver knees (normal and with radiographic OA) using an established maximum intensity projection technique (CT-OAM) and a new method that allows average bone density to be computed in relation to depth from the subchondral surface (CT-TOMASD).

Both CT-OAM maximum intensity analyses and CT-TOMASD 0–2.5 mm layer analyses identified an average 17% greater subchondral density in the whole medial compartment of OA knees when compared to normal knees. The comparable findings between CT-OAM and CT-TOMASD at the 0–2.5mm layer was not surprising since both techniques mainly quantify the density of the same component of subchondral bone: subchondral cortical bone. Subchondral cortical bone varies in thickness from 1.5–3.3 mm at the joint centers [16, 72] to 0.1–0.3 mm at the periphery [72]. The CT-

OAM technique selected ~90% of maximum density values from bone located less than 1.5 mm from the subchondral surface. CT-OAM, therefore, primarily characterizes subchondral cortical bone density. In the same manner, CT-TOMASD analyses across the 0–2.5 mm layer primarily characterize subchondral cortical bone density and underlying subchondral trabecular bone density. Neither CT-OAM nor CT-TOMASD (all layers) recognized density differences between OA and normal knees in the lateral compartment. However, only two of the six knees demonstrated evidence of lateral OA, likely explaining the lack of density differences at the lateral plateau.

Results of the focal regional analyses differed between the two techniques. Focal analyses of subchondral bone density did not differ between OA and normal knees using CT-OAM. This could be related to CT-OAM primarily characterizing highly dense subchondral cortical bone. Focal analyses search for the highest average density contained within a 10 mm diameter 'focal spot'. These high density focal analyses within naturally dense subchondral bone may not provide sufficient contrast to recognize differences between OA and normal subchondral bone. CT-TOMASD depth-specific focal analysis, however, revealed significantly greater focal BMD in OA subchondral bone at the 0–2.5 layer (+24%) and 2.5–5 mm layer (+36%) when compared to normal knees. This could be related to CT-TOMASD combining subchondral cortical *and* trabecular bone density across these depths, which may provide sufficient contrast between OA and normal subchondral bone.

CT-TOMASD uses small isotropic voxel sizes and the subchondral surface as a reference point to measure subchondral density in relation to depth from the subchondral surface. Thus, CT-TOMASD can approximate the density of subchondral cortical + subchondral trabecular bone (0–2.5 mm layer), subchondral trabecular bone (2.5–5.0 mm layer), and epipyseal trabecular bone (5–10 mm layer) within the proximal epiphysis. The proficiency of CT-TOMASD at identifying differences between OA and normal medial compartment and focal densities can likely be attributed to the method's approximation of subchondral trabecular density. Subchondral trabecular bone demonstrates high bone

turnover and is more metabolically active and adaptive compared to cortical bone [158, 159] due primarily to increased bone surface area [158]. Detectable changes in trabecular bone may also precede detectable changes in cortical bone during the OA disease process [137].

In contrast with CT-TOMASD, CT-OAM primarily focuses on subchondral cortical bone density and ignores adjacent bone with lower density. Subsequently, OA-related changes in subchondral trabecular bone density are likely missed by CT-OAM. In all fairness, CT-OAM results at the proximal tibia are directly dependent upon imaged slice thickness (current: 0.5 mm) and in-plane resolution. A larger slice thickness (e.g., 2.5 mm) may capture the density of both subchondral cortical and subchondral trabecular bone, and offer density differences comparable with CT-TOMASD results at the 0–2.5 mm layer. However, a larger slice thickness should be avoided as this will limit accurate image reformatting and lead to significant partial volume effects at the bone/cartilage interface and within the thin subchondral endplate, resulting in underestimates of bone density.

Previous research studies examining direct associations between proximal tibial BMD and knee OA have offered conflicting results [10-12, 22, 24, 26]. This may be due to selected analysis regions containing subchondral cortical, subchondral trabecular and/or epipyseal trabecular bone, which may all be affected differently by OA [17, 28, 29]. Subchondral cortical bone demonstrates altered cortical thickness and density with OA [74, 137]. Subchondral trabecular bone demonstrates increased trabecular thickness [14, 75], volume [14, 49, 75], and apparent density [49] with OA; possibly in relation to different stages of OA disease progression [17, 29]. Subchondral trabecular bone transitions to epiphyseal trabecular bone, which evidences reduced trabecular thickness [27, 73, 93, 94] and reduced apparent density with OA [28, 137, 138, 160], to the point of being labeled osteoporotic [73]. The exact location of this trabecular transition zone is unknown, though estimated to be approximately 5.0 mm from the subchondral surface. These variations highlight the importance of an imaging technique capable of distinguishing density at specific depths from the subchondral surface.

The only comparable study assessing volumetric proximal tibial subchondral density was conducted by Bennell et al [28] using pQCT at distances of ~6.4–8.6 mm (~2% site) and ~12.7–17.1 mm (~4% site) from the subchondral surface. Comparisons between OA and normal knee densities at the 2% site by Bennell et al [28] are in accordance with CT-TOMASD findings at the 5–10 mm layer: neither study reported differences in whole medial or lateral compartment density. Sub-compartment regional analyses by Bennell et al [28] did, however, demonstrate lower posterior density at the 2% site in OA knees [28]. Our analyses did not incorporate comparable regional analyses (i.e., anterior/central/posterior compartment density) required for comparison to this finding.

While unable to directly quantify bone mineral density, MRI has been used to assess OA-related changes in proximal tibial subchondral bone, specifically trabecular bone [96-99]. Contrasting with this study, these studies generally showed reductions in trabecular bone quantity (e.g., bone volume fraction, trabecular thickness) with OA progression and disease severity [96-99]. However, in these studies trabecular bone appeared to be from epiphyseal regions [96-99]. MRI observed reductions in bone quantity therefore agree with radiographic studies showing reduced epiphyseal trabecular density with OA [28, 137, 138, 160]. In contrast to QCT, MRI has the ability to simultaneously image subchondral bone and articular cartilage. While QCT cannot directly image cartilage, the recent introduction of contrast-enhanced CT techniques capable of imaging cartilage biochemistry [161-163] make both QCT and MRI appealing for assessing links between subchondral bone and cartilage [164].

This study has specific strengths. First, we used identical imaging data, in identical 3D orientations, for both CT-OAM and CT-TOMASD density analyses. The same parallel rays (column of 3D voxels, length: 20 voxels, 10 mm) were used for both CT-OAM (maximum density contained within each ray) and CT-TOMASD analyses (average density of portions of each ray). Therefore, this study design permits unbiased comparisons between CT-OAM and CT-TOMASD analysis methods. Second,

we aligned all knees in similar 3D orientations relative to landmark boundary points and best-fit planes. This minimized density differences due to dissimilar orientations, thereby permitting reliable comparisons between OA and normal subchondral density from both medial and lateral plateaus. Third, in addition to average CT-OAM and CT-TOMASD density measures, we provide precision errors for each outcome. The observed CT-TOMASD density differences between OA and normal knees were on average 10 times greater than the precision errors, and therefore trustworthy.

This study has specific limitations requiring consideration. First, our small samples of normal (n=10) and OA (n=6) cadaveric knees. We previously determined (Chapter 2) that a sample size of 6 knees, per group, provided over 90% power to distinguish density differences between normal and OA knees using CT-TOMASD focal analyses. CT-OAM comparisons, however, may have been underpowered. As indicated by wide 95% CIs, a larger sample size may have been required to detect significant focal density differences between normal and OA knees with CT-OAM. However, this requirement may also indicate a greater sensitivity of CT-TOMASD at capturing focal density differences. Second, the use of *ex vivo* cadaveric specimens prevented us from linking density measures with relevant OA symptoms such as joint space narrowing or pain. Third, we used radiographic KL scoring to categorized OA severity according to CT evidence of osteophytes and sclerosis. Although Kellgren-Lawrence scoring is a commonly used clinical radiographic tool for OA assessments, the technique is imperfect because it combines osteophytes with sclerosis and joint space narrowing. Separate analyses of radiographic OA features, including subchondral cysts, may have offered alternative OA characterizations to composite Kellgren-Lawrence grades [165] . However, radiographic evidence of osteophyte presence has shown strong associations with knee OA, specifically knee pain [166]. All of our six OA knees demonstrated evidence of osteophyte presence. Fourth, as previously stated we used CT evidence of osteophytes and sclerosis to categorize OA severity. Sclerotic evidence directly increases CT-OAM and CT-TOMASD density measures. It would

therefore appear that CT-OAM or CT-TOMASD analyses do not necessarily offer supplementary information to existing qualitative OA scoring methods such as Kellgren-Lawrence. However, five of the six knees with medial OA were classified by the participating orthopaedic surgeon as having minimal OA presence (mKL=1) with no evidence of sclerosis. Despite minimal sclerotic evidence, CT-TOMASD analyses showed significantly higher density (39%) in OA knees than normal knees, suggesting CT-TOMASD potential for OA identification. Fifth, we did not assess cartilage degeneration—which may have impacted subchondral bone remodeling—with subchondral bone density measures.

Both CT-OAM and CT-TOMASD techniques have specific limitations requiring consideration. First, the presence of air pockets and subchondral bone cysts—a feature of OA—may lower subchondral densities. These reductions would not influence CT-OAM maximum intensity measures. These reductions would, however, influence CT-TOMASD whole compartment density measures. Focal regional analyses, on the other hand, would be relatively unaffected by these reductions since they search for local high density bone and avoid low density bone. Second, clinical QCT imaging is generally limited to isotropic resolutions between 0.5 and 0.625 mm. With currently available resolutions—and associated partial volume effects—it is difficult to conduct separate analyses of subchondral cortical, subchondral trabecular and epiphyseal trabecular bone. In fact, along the thin cortical periphery (0.1–0.3 mm thickness [72]) we cannot separate subchondral cortical from subchondral trabecular bone. For these reasons, we used CT-TOMASD to categorize density across predefined depths from the subchondral surface corresponding to approximations of these subchondral regions [16, 72, 90, 157, 167]. However, CT-TOMASD layer analyses likely truly represent the combined density of two or more constituents of subchondral bone. Third, although the use of different depth measures for different sized subjects by CT-TOMASD permits subject-to-subject comparisons, the depth measure may be influenced by the OA disease process. Subchondral bone surface area (which includes osteophyte area) has been shown to increase with OA [168-171], which would lead to

smaller depth measures and overestimations of density. As previously stated (Chapter 2 – Methods), the subject-specific depths were determined using the following equation (after reorganization):

$$d_{ss} = \frac{d \cdot \overline{area}}{\overline{volume}} \cdot \frac{volume_{ss}}{area_{ss}}$$

This equation was created with the assumption that large persons have large subchondral surface areas and proximal tibial volumes, and vice versa for small persons. If, however, $area_{ss}$ increased with OA the subject-specific depth (d_{ss}) would be reduced using this equation (assuming $volume_{ss}$ remained constant). CT-TOMASD measures would therefore be prone to overestimates of density with OA because bone closest to the surface has the highest density. However, comparisons of OA and normal knees showed no differences in CT-TOMASD assessed proximal tibial $volume_{ss}$ (p=0.18) or $area_{ss}$ (p=0.21). This is likely due to CT-TOMASD segmentations not incorporating osteophyte volume or area. Therefore, we believe the subject-specific depth equation is applicable during stages of OA disease progression, particularly since it is reasonable to presume that changes in area and volume with be minimal at early stages of OA disease onset. Fourth, as previously discussed (Chapter 2 - Discussion), the 2D projection nature of CT-TOMASD can lead to overestimations of density near regions displaying large curvature (e.g., 17% error with 40^{o} inclination). However, the net effects of surface curvature on proximal tibial BMD measures are small (< 4% for whole compartment BMD). Given that measured inclination from coronal and sagittal reconstructed CT images showed no apparent differences between OA and normal proximal tibiae, it is unlikely that surface inclination accounted for a large proportion of the observed differences between OA and normal proximal tibial subchondral bone density. Fifth, an inherent limitation of any QCT-based approach is that the participant is exposed to ionizing radiation (0.15 mSv for this study). Although not a concern with current cadaveric specimens, the ultimate goal of this research is to develop tools for *in vivo* clinical usage. While CT-TOMASD and CT-OAM analyses induce higher dosages than DXA (0.012 mSv

[172]), pQCT (0.0015 mSv [173]), and MRI (nonionizing), excellent volumetric 3D capabilities and ability to characterize both subchondral cortical and trabecular bone density near the joint surface make clinical QCT a viable option for studying OA-related subchondral bone changes.

3.6 Conclusions

Both CT-OAM and CT-TOMASD identified comparably higher medial compartment densities in OA tibiae when compared to normal tibiae. In addition, CT-TOMASD identified greater focal density differences between normal and OA knees with increasing depth from the subchondral surface. Depth-specific density analyses may help identify and quantify small changes in subchondral BMD associated with OA disease initiation and progression.

4 *In Vivo* Precision of CT-TOMASD

4.1 Synopsis

This chapter describes our test of the precision of CT-TOMASD measures, *in vivo*, in knees with and without evidence of OA. *In vivo* precision errors were 9x smaller than previously observed differences between OA and normal density, which suggests substantial utility for identifying and quantifying changes in subchondral BMD in people living with OA.

4.2 Introduction

The exact role of subchondral bone in the etiology of OA is unclear. To date, much of our understanding of OA-related subchondral bone changes has come from animal models or cadaveric specimens as opposed to *in vivo* assessments of people living with OA.

Quantitative computed tomography (QCT) has potential to identify and quantify OA-related changes in subchondral bone density *in vivo*. Recently, peripheral QCT (pQCT) has been used to study trabecular bone density in the proximal tibia of patients living with knee OA [28]. pQCT scanners, however, are not widely available and are often limited to a single axial CT scan of fixed slice thickness (typically 2.3 mm) and long scanning times (minutes for a single pQCT scan). pQCT density results—and related precision / repeatability errors—are subsequently closely dependent upon correct patient positioning and motion artifacts. QCT, on the other hand, offers wide availability using clinical CT scanners, shorter acquisition times (seconds for hundreds of QCT scans) and small isotropic voxel sizes (0.5–0.625 mm) [30, 31]. To date, clinical QCT has not yet been applied for *in vivo* assessment of both subchondral cortical and subchondral trabecular bone density in people with knee OA.

To help elucidate the role of subchondral bone in OA we developed the novel 3D imaging tool CT-TOMASD. CT-TOMASD regional analyses of cadaveric proximal tibiae, using one of the more advanced clinical CT scanners currently available (Toshiba Aquilion 64-slice, selected voxel size: 0.5

mm isotropic), demonstrated precision errors less than 3.5%. Compared to the scanner used in the previous study, 4-slice CT scanners are also widely available for clinical QCT research but offer poorer image resolution (i.e., larger 3D voxels), lower tube currents (which increase image noise), and longer scanning times (which can contribute to patient movement artifacts). It is not clear how precise CT-TOMASD regional density measures are *in vivo* when there is (plausible) subject motion, and it is not clear how precise CT-TOMASD will be when imaging is carried out using 4-slice CT scanners.

The objective of this prospective study was to conservatively test the precision of CT-TOMASD for measurement of both subchondral cortical and trabecular bone density *in vivo* using a 4-slice clinical CT scanner (GE Lightspeed 4-slice CT, selected voxel size: 0.625 mm isotropic).

4.3 Methods

4.3.1 Subjects

We recruited fourteen study participants (3 males and 11 females; ages ranging from 23 to 71 years (mean ± standard deviation (SD): 49.9 ± 11.9 years)); including 5 left and 9 right knees. We did not pre-select participants with or without knee OA, although some participants informed us that they were afflicted with diagnosed knee OA or undiagnosed knee pain. We randomly selected left or right knees unless the participant had knee pain, in which case the more painful knee was studied. Retrospectively, we systematically analyzed all knees for OA presence using the KL scoring system [57] with axial, coronal and sagittal CT reconstructions. Seven of the 14 knees exhibited evidence of osteophytes and sclerosis, and were classified as OA (1 male and 6 females; 52.4 ± 8.7 years, one KL=1-2, three KL=2, two KL=3, one KL=4). The remaining seven participants exhibited no evidence of OA and were classified as normal (KL=0) (47.3 ± 14.8 years). IRB approval was obtained and informed consent was provided by all participants prior to study involvement.

4.3.2 Imaging Methodology

4.3.2.1 QCT Image Acquisition

We performed single-energy QCT using a clinical CT scanner (Lightspeed 4-slice, General Electric, Milwaukee, WI, USA). We scanned the knee of interest with an image volume that included the patella, distal femur and proximal tibia, though only proximal tibial images were used in this analysis. CT scanning parameters included: standard bone reconstruction kernel (BONE), axial scanning plane, 120 kVp tube voltage, 150 mA tube current, ~90 second scan time, ~240 slices, 0.625 mm isotropic voxel size (0.625 mm slice thickness, 0.625 x 0.625 mm in-plane pixel size). Each participant was oriented supine with the knee of interest centrally located within the CT gantry. We included a solid QCT reference phantom (Model 3T; Mindways Software Inc, Austin, TX, USA) located below the knee to transform CT HU to equivalent volumetric BMD (mg/cm^3 K_2HPO_4). Each participant was scanned three times over two consecutive days (maximum two scans per day) with repositioning in-between scanning. This protocol met conservative recommendations by Glüer et al [133] for measuring the reproducibility of bone densitometry techniques, specifically 28 degrees of freedom (DOF) using 14 subjects and 3 repeated measures. These recommendations are considered sufficient to establish reliable precision errors with small confidence intervals (30% higher than mean precision errors) [133].

4.3.2.2 CT-TOMASD Image Analysis

We previously described the CT-TOMASD methodology in detail (Chapter 2). Briefly, we converted grayscale HU to equivalent volumetric BMD (mg/cm^3 K_2HPO_4) using linear regression equations derived from known densities contained within the reference phantom ($r^2 > 0.99$) (Matlab 2007a, MathWorks, Natick, MA, USA) (Figure 4-1-A). We segmented the proximal tibia using a combination of manual correction and region growing segmentation techniques with commercial segmentation software (Analyze8.1; Mayo Foundation, Rochester, MN, USA) (Figure 4-1-B). To guide the

segmentation process, we determined optimal threshold values for defining the subchondral bone surface, for each individual knee, using the HMH method [131, 132]. To accelerate the segmentation process, we smoothed the QCT images using ITK open-source software (National Library of Medicine; http://www.itk.org) with the Binary Min/Max Curvature Flow filter (Iterations: 10, Time Step: 0.125, Radius: 1, Threshold: density of soft tissue previously found using HMH). We realigned and reconstructed each imaged proximal tibia relative to best-fit planes fit to each medial and lateral plateau, which were derived from manually selected boundary points outlining the outer periphery and inner region of each plateau (Matlab 2007a) (Figures 4-1-C and 4-1-D). We performed CT-TOMASD analyses across three layers (0–2.5 mm, 2.5–5 mm, and 5–10 mm) measured in relation to depth from the subchondral surface (Matlab 2007a). We projected average density of each layer to a 2D image to create a surface projected rendered image of subchondral BMD, expressed in relation to depth from the subchondral surface (Figure 4-1-E). To account for differences in physical size, we controlled the depth measure for each subject using the previously discussed user-defined normalized depth. We performed a series of regional analyses on each 2D projected image (0–2.5 mm, 2.5–5 mm, and 5–10 mm layers), including: (a) medial plateau BMD; (b) lateral plateau BMD; (c) anterior/central/posterior compartment BMD (Figure 4-1-E); (d) medial:lateral (M:L) BMD ratio; and (e) average BMD of a 10-mm diameter core or 'focal spot' which searched each medial and lateral plateau for the *highest* focal densities present within each plateau (Figure 4-1-E).

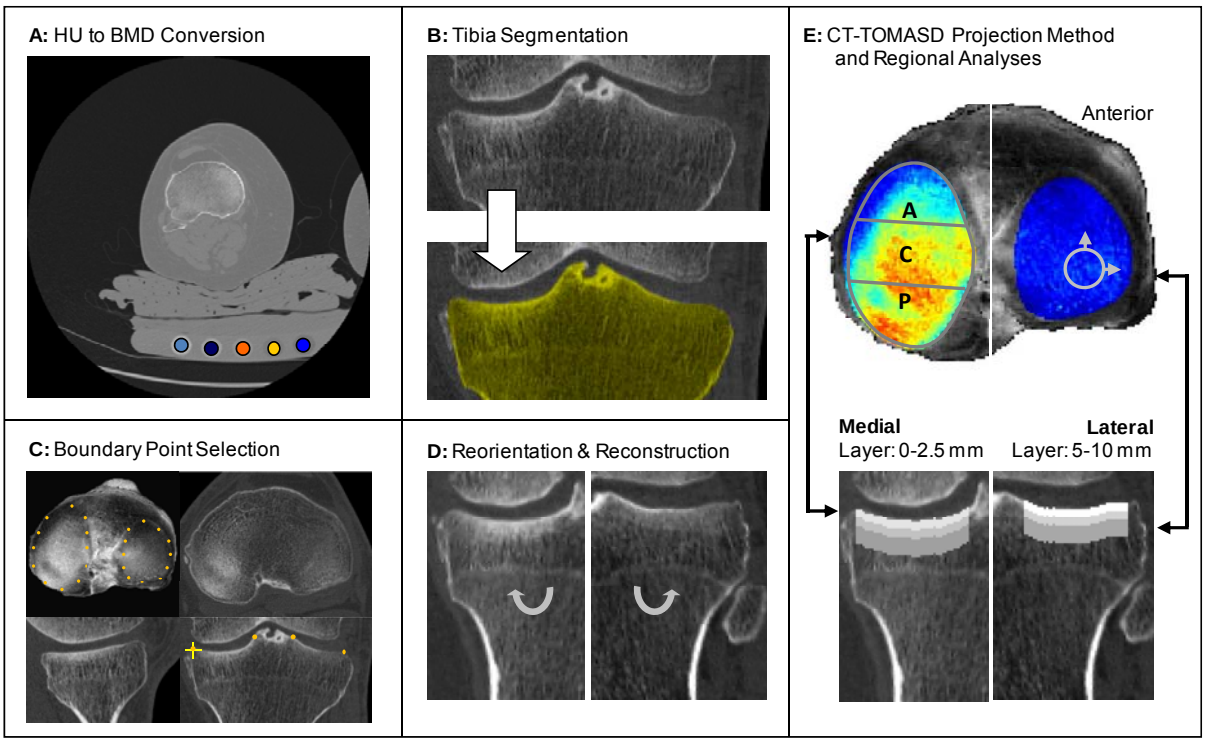

Figure 4-1. Methodological sequence for CT-TOMASD analyses of proximal tibiae consists of converting CT grayscale intensity to BMD using a QCT reference phantom (*A*), followed by segmentation (*B*). Peripheral and inner boundary points are manually selected (*C*) to define the medial and lateral plateaus, with each plateau reoriented and reconstructed relative to 'best-fit' planes passing through plateau boundary points (*D*). Surface projection image processing is performed to map 3D subchondral density measured in relation to depth from the subchondral surface (i.e., 0-2.5 mm) directly at the joint surface (*E*). CT-TOMASD regional analyses are performed, including the max BMD within a 10 mm diameter focal region of interest and the average BMD contained within the anterior, central and posterior compartments of each plateau (*E*).

4.3.3 Statistical Analysis

According to procedures outlined by Glüer et al [133], we assessed the short-term *in vivo* precision of CT-TOMASD regional density measures using fourteen participants who were scanned three times each (42 total scans, 28 DOF). We report mean values for each regional analysis for comparison with related precision errors. We report the repeatability of each regional analysis using both absolute values (root mean square standard deviation - SD_{RMS}) and as a percentage using root mean square coefficients of variation ($CV\%_{RMS}$) [133]. We also assessed the repeatability of CT-TOMASD measures

using intraclass correlation coefficients (ICC), which relate inter-subject variance to population variance [174]. We used a two-way mixed ICC model [174, 175]. Statistical analyses were performed using commercial software (Matlab 2007a and SPSS 18.0; SPSS Inc, Chicago, IL, USA).

4.4 Results

In vivo precision errors associated with the CT-TOMASD method were small. For both OA and healthy participants, average $CV\%_{RMS}$ precision errors were 2.3%; reaching a maximum $CV\%_{RMS}$ of 3.9% (Table 4-1). ICC showed a high repeatability ranging from 0.98 to 1.00. For healthy participants, average $CV\%_{RMS}$ precision errors were 2.0%; reaching a maximum $CV\%_{RMS}$ of 4.2% (Table 4-2). For OA participants, average $CV\%_{RMS}$ precision errors were 2.4%; reaching a maximum $CV\%_{RMS}$ of 4.3% (Table 4-3). Sample *in vivo* images of CT-TOMASD analyses for one healthy and one OA knee are presented in Figure 4-2.

Table 4-1. Precision results for CT-TOMASD average BMD measures (mg/cm^3 K_2HPO_4) in healthy and osteoarthritic knees (14 participants, 3 scans each, 28 degrees of freedom). Mean density results are reported from regional analyses across three layers (0–2.5 mm, 2.5–5 mm and 5–10 mm) measured relative to the subchondral surface. For each medial and lateral plateau, regional analyses included total average BMD, anterior/central/posterior compartment BMD, and average BMD of a 10 mm diameter 'focal spot' which searched each plateau for the highest focal density. The mean medial:lateral BMD ratio, derived by dividing total medial plateau BMD by total lateral plateau BMD, is also reported. Precision is reported using root mean square standard deviations (SD_{RMS}), coefficients of variation ($CV\%_{RMS}$), and intraclass correlation coefficients (ICC). $CV\%_{RMS}$ also includes range of (Min-Max) $CV\%_{RMS}$ values.

Regional Analysis		Layer: 0–2.5 mm				Layer: 2.5–5 mm				Layer: 5–10 mm			
		Mean	SD_{RMS}	$CV\%_{RMS}$	ICC	Mean	SD_{RMS}	$CV\%_{RMS}$	ICC	Mean	SD_{RMS}	$CV\%_{RMS}$	ICC
Medial Plateau	Total	495	5.5	1.2 (0.1-3.2)	1.00	339	5.3	1.6 (0.1-3.1)	1.00	204	3.3	1.5 (0.6-2.4)	1.00
	Anterior	467	14.4	3.4 (0.4-6.9)	0.98	315	7.5	3.0 (0.1-6.5)	0.99	209	4.1	2.2 (0.5-4.2)	1.00
	Central	566	5.8	1.0 (0.2-1.9)	1.00	384	6.8	2.0 (0.2-4.4)	0.99	206	5.0	2.3 (0.3-4.1)	0.99
	Posterior	421	13.1	2.9 (0.3-6.2)	0.99	298	11.4	3.4 (1.3-8.8)	0.98	196	5.7	3.0 (0.5-6.5)	0.98
	Focal Spot	690	5.8	0.9 (0.3-1.5)	1.00	517	9.5	1.8 (0.1-2.7)	0.99	323	6.7	2.0 (0.2-3.1)	1.00
Lateral Plateau	Total	392	6.0	1.6 (0.5-3.7)	0.99	238	5.4	2.5 (0.3-4.8)	0.99	144	2.7	1.9 (0.4-3.3)	1.00
	Anterior	279	11.1	3.9 (0.4-8.3)	0.98	181	7.6	4.0 (0.9-8.7)	0.98	129	3.5	2.9 (0.8-5.1)	0.99
	Central	439	7.7	1.8 (0.8-3.8)	0.99	269	6.4	2.6 (0.5-5.5)	0.99	151	3.0	2.2 (0.5-4.0)	0.99
	Posterior	426	10.5	2.4 (0.3-4.2)	0.99	246	8.5	3.7 (1.0-8.2)	0.99	147	4.0	2.6 (0.3-4.5)	0.99
	Focal Spot	638	7.5	1.1 (0.3-1.6)	0.99	394	12.5	3.8 (0.2-9.7)	0.99	210	4.2	2.0 (0.1-3.5)	0.99
M:L BMD Ratio		1.27	0.024	1.8 (0.3-3.5)	0.98	1.47	0.030	1.9 (0.5-4.2)	0.99	1.49	0.020	1.5 (0.4-2.7)	1.00

Table 4-2. Precision results for CT-TOMASD average BMD measures (mg/cm^3 K_2HPO_4) in healthy knees (7 participants, 3 scans each, 14 degrees of freedom). Mean density results are reported from regional analyses across three layers (0–2.5 mm, 2.5–5 mm and 5–10 mm) measured relative to the subchondral surface. For each medial and lateral plateau, regional analyses included total average BMD, anterior/central/posterior compartment BMD, and average BMD of a 10 mm diameter 'focal spot' which searched each plateau for the highest focal density. The mean medial:lateral BMD ratio, derived by dividing total medial plateau BMD by total lateral plateau BMD, is also reported. Precision is reported using root mean square standard deviations (SD_{RMS}), coefficients of variation ($CV\%_{RMS}$), and intraclass correlation coefficients (ICC). $CV\%_{RMS}$ also includes range of (Min-Max) $CV\%_{RMS}$ values.

Regional Analysis		Layer: 0–2.5 mm				Layer: 2.5–5 mm				Layer: 5–10 mm			
		Mean	SD_{RMS}	$CV\%_{RMS}$	ICC	Mean	SD_{RMS}	$CV\%_{RMS}$	ICC	Mean	SD_{RMS}	$CV\%_{RMS}$	ICC
Medial Plateau	Total	467	5.7	1.3 (0.2-3.2)	0.99	328	3.9	1.2 (0.3-2.6)	1.00	189	3.1	1.4 (0.5-2.6)	0.99
	Anterior	462	11.4	2.6 (0.4-5.2)	0.98	323	6.3	2.0 (0.4-3.8)	0.99	195	3.5	1.8 (0.7-2.8)	1.00
	Central	535	4.7	0.9 (0.3-1.3)	0.99	368	6.8	1.9 (0.7-3.8)	0.99	190	4.8	2.1 (0.4-3.5)	0.99
	Posterior	368	8.8	2.4 (1.0-3.6)	0.97	275	6.0	2.3 (0.9-2.9)	0.99	183	3.6	2.0 (0.8-2.7)	0.98
	Focal Spot	672	5.6	0.8 (0.3-1.2)	0.99	496	8.9	1.6 (0.4-2.4)	0.99	284	5.7	1.9 (0.4-3.7)	1.00
Lateral Plateau	Total	379	5.4	1.6 (0.5-3.6)	0.99	247	4.6	2.1 (0.7-4.1)	0.99	154	2.3	1.6 (0.9-2.3)	0.99
	Anterior	257	9.3	3.7 (0.4-8.2)	0.95	183	7.5	4.2 (0.8-8.2)	0.96	134	3.3	2.7 (0.7-4.6)	0.99
	Central	424	7.5	1.8 (0.8-3.7)	0.97	272	5.3	1.9 (0.3-2.9)	0.99	158	3.0	2.0 (0.3-3.2)	0.99
	Posterior	422	8.9	2.2 (0.6-3.3)	0.99	267	7.3	2.8 (0.6-4.3)	0.99	164	3.9	2.3 (0.1-3.5)	0.99
	Focal Spot	638	6.4	1.0 (0.3-1.4)	0.99	415	9.9	2.4 (1.0-3.5)	0.99	223	4.7	1.8 (0.5-3.0)	0.99
M:L BMD Ratio		1.24	0.022	1.8 (0.6-3.4)	0.95	1.35	0.027	2.0 (0.5-4.2)	0.95	1.24	0.016	1.3 (0.4-1.8)	0.99

Table 4-3. Precision results for CT-TOMASD: average BMD measures (mg/cm^3 K_2HPO_4) in osteoarthritic knees (7 participants, 3 scans each, 14 degrees of freedom). Mean density results are reported from regional analyses across three layers (0–2.5 mm, 2.5–5 mm and 5–10 mm) measured relative to the subchondral surface. For each medial and lateral plateau, regional analyses included total average BMD, anterior/central/posterior compartment BMD, and average BMD of a 10 mm diameter 'focal spot' which searched each plateau for the highest focal density. The mean medial:lateral BMD ratio, derived by dividing total medial plateau BMD by total lateral plateau BMD, is also reported. Precision is reported using root mean square standard deviations (SD_{RMS}), coefficients of variation ($CV\%_{RMS}$), and intraclass correlation coefficients (ICC). $CV\%_{RMS}$ also includes range of (Min-Max) $CV\%_{RMS}$ values.

Regional Analysis		Layer: 0–2.5 mm				Layer: 2.5–5 mm				Layer: 5–10 mm			
		Mean	SD_{RMS}	$CV\%_{RMS}$	ICC	Mean	SD_{RMS}	$CV\%_{RMS}$	ICC	Mean	SD_{RMS}	$CV\%_{RMS}$	ICC
Medial Plateau	Total	525	5.1	1.0 (0.2-1.2)	1.00	351	5.7	1.7 (0.3-3.2)	1.00	218	3.1	1.4 (0.1-2.3)	1.00
	Anterior	475	17.5	4.1 (0.4-7.0)	0.98	306	8.6	3.8 (0.1-6.5)	0.99	221	4.5	2.6 (1.1-4.1)	1.00
	Central	597	6.8	1.1 (0.1-1.9)	1.00	402	6.4	1.9 (0.5-3.7)	1.00	222	4.4	2.0 (0.6-2.9)	1.00
	Posterior	474	15.6	3.3 (0.5-6.4)	0.99	323	14.6	4.2 (1.4-8.6)	0.98	209	7.3	3.7 (0.8-6.4)	0.99
	Focal Spot	708	5.5	0.8 (0.4-1.6)	1.00	538	9.1	1.7 (0.4-2.6)	1.00	359	7.6	2.0 (0.8-2.7)	1.00
Lateral Plateau	Total	405	5.6	1.3 (0.5-2.2)	1.00	231	5.8	2.5 (0.3-4.5)	0.99	134	3.2	2.1 (0.6-3.4)	1.00
	Anterior	302	12.4	4.0 (1.6-6.5)	0.98	181	7.7	3.7 (1.2-5.8)	0.99	125	3.8	3.0 (1.5-4.9)	1.00
	Central	455	6.7	1.5 (0.3-1.9)	0.99	268	6.8	2.8 (0.2-4.6)	0.99	144	2.7	2.0 (0.3-4.0)	1.00
	Posterior	432	11.0	2.3 (0.3-3.9)	0.98	225	9.6	4.3 (0.4-7.7)	0.98	128	4.5	2.9 (0.3-4.6)	0.99
	Focal Spot	640	7.1	1.1 (0.6-1.4)	1.00	374	13.4	4.1 (1.1-8.5)	0.98	195	3.4	2.0 (0.2-3.2)	1.00
M:L BMD Ratio		1.30	0.025	1.9 (0.3-3.2)	0.98	1.59	0.033	1.9 (1.0-2.7)	1.00	1.73	0.022	1.5 (0.2-2.7)	1.00

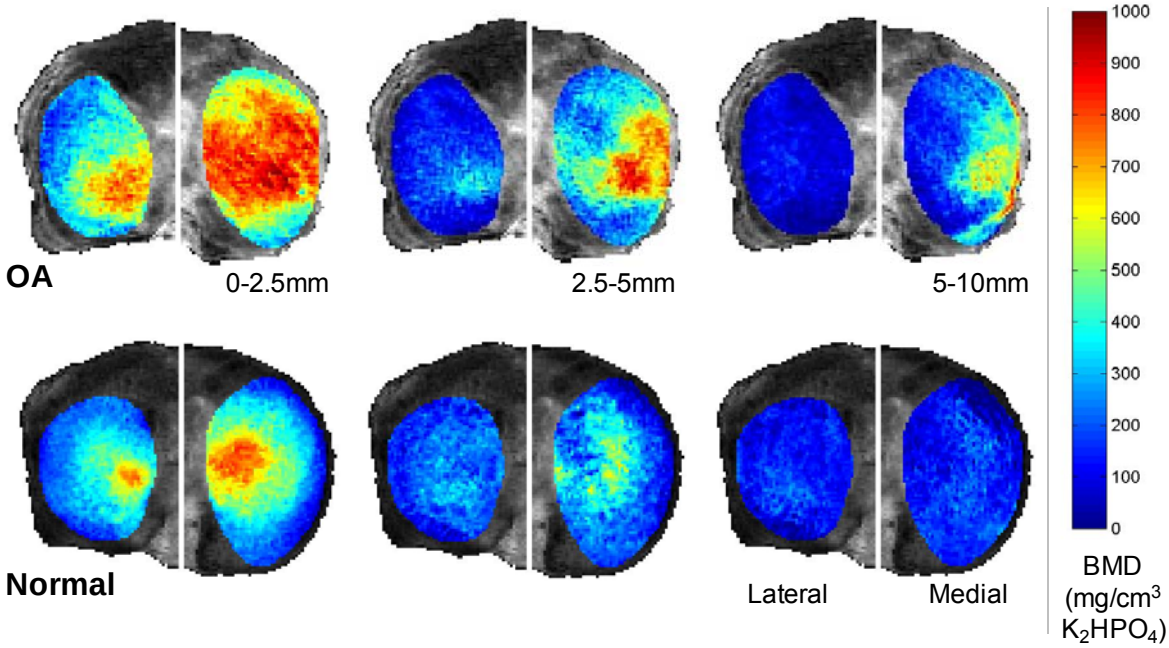

Figure 4-2. Density maps of proximal tibial subchondral bone using CT-TOMASD, which averages bone mineral density (BMD) in relation to depth from the subchondral surface (e.g., the 0- to 2.5-mm layer). Results are displayed for one knee demonstrating OA and one healthy knee demonstrating no evidence of radiographic OA.

4.5 Discussion

This study tested the *in vivo* precision of CT-TOMASD measures of proximal tibial subchondral density from the knees of healthy individuals and those with knee OA. This is the first *in vivo* study to use clinical QCT to assess proximal tibial subchondral cortical and subchondral trabecular vBMD from OA and normal knees.

CT-TOMASD provided precise ($CV\%_{RMS}$ less than 3.9%) *in vivo* measures of subchondral cortical and trabecular bone density, measured in relation to depth from the subchondral surface. In general, these *in vivo* precision errors were much less than our previously observed density differences (>36%) between OA and normal cadaver knees, and can therefore be considered trustworthy. The high precision of CT-TOMASD is due to the use of isotropic voxels and the resulting ability to reliably reconstruct the 3D image volume in various orientations. By combining isotropic voxels with boundary

points defining each medial and lateral plateau, we are able to reconstruct the imaged proximal tibia in repeatable orientations, and thereby minimize the effects of patient positioning. The high precision of CT-TOMASD measures may also be attributed to rapid scanning times (~90 seconds for +240 images) which minimized the effects of patient movement.

Our *in vivo* precision results compare favorably with our previous *ex vivo* studies [157, 176] using a clinical 64-slice CT scanner (Toshiba Aquilion, Toshiba Medical Systems, Tokyo, Japan) with eight cadaver knees, scanned three times each (24 total scans, 16 DOF). Scanning parameters with the 64-slice scanner included: 120 kVp tube voltage, 300 mA tube current, 0.5 mm isotropic voxel size, ~300 slices, ~3.4 second scan time. A standard bone kernel (FC 30) was used for postprocessing of the CT images. *Ex vivo* $CV\%_{RMS}$ results were less than 3.5%, which suggests that the effects of patient movement artifacts due to a longer scanning time (*in vivo*: ~90 seconds, *ex vivo*: ~3.4 seconds) are small and that the larger *in vivo* voxel size (0.625 vs. 0.5 mm) and lower tube current (150 mA vs. 300 mA) have small effects on CT-TOMASD precision errors. However, it is important to note that the larger voxel size may diminish our ability to capture small changes associated with OA, particularly longitudinal changes occurring over short periods of time.

The precision of CT-TOMASD compares favorably to *in vivo* volumetric proximal tibial subchondral density measurements made using pQCT [28]. ICCs for pQCT regional analyses located 6.4–8.6 mm from the subchondral surface ranged from 0.86 to 0.99 [28], which compare to 0.99–1.00 for CT-TOMASD in the 5–10 mm layer. Lower ICCs for pQCT density measures may be due to long scanning times (~15 minutes for 4 axial pQCT slices) and associated motion artifacts, as well as operator error in positioning the participant in a repeatable orientation. ICC differences between pQCT and QCT density measures may also be due to smaller regional analyses used with the pQCT study. As opposed to CT-TOMASD analyses of anterior/central/posterior regions (3 ROIs per plateau), the

pQCT study subdivided similar ROIs into middle and peripheral regions (6 ROIs per plateau) [28]. Smaller ROIs will likely have reduced ICCs and greater associated $CV\%_{RMS}$ precision errors.

CT scanning parameters used with this study were derived from preliminary cadaver work comparing proximal tibial BMD with different tube voltages (120, 100 kVp) and tube currents (200, 150, 100 mA) (Appendix B). These analyses revealed that the 120 kVp tube voltage and 150 mA tube current settings offered minimal noise and density deviations from those obtained with higher tube voltage and current, and included the added advantage of lower radiation dosage to the patient. These conclusions agree with previous findings [177, 178], in particular Patel et al [178] who reported that calcaneus bone properties assessed with 120 kVp and 150 mA did not differ substantially from those obtained with 120 kVp and 300 mA. Our voxel size was based upon 1) a need to use isotropic voxels for CT-TOMASD analyses 2) recommendations by the QCT phantom manufacturer that the z-dimension of the 3D voxel match the slice thickness capabilities of the CT machine (0.625 mm), and 3) physical dimensions of the object of interest (i.e., knee) and the appropriately sized QCT reference phantom, which must be contained within each image. With our chosen voxel size we were able to meet recommendations by the QCT manufacturer and simultaneously image the QCT reference phantom along with both knees of our most obese study participant. Given that OA is strongly associated with obesity [179], we believe this to be a sufficient voxel size for imaging numerous individuals afflicted with knee OA.

The strengths of this study relate to our appropriate number of subjects and scans to establish reliable precision errors, the inclusion of both healthy and OA knees, as well as reported ICC and $CV\%_{RMS}$ precision errors for *each* individual density measure and ROI. First, we met conservative recommendations for number of subjects and scans by Glüer et al [133], specifically 28 DOF with 14 subjects and 3 repeated measures. These recommendations are considered sufficient to establish reliable precision errors with small confidence intervals (30% higher than mean precision errors) [133].

Second, we determined CT-TOMASD precision using both healthy and OA knees. Analyses of only healthy or only OA knees may have offered misrepresentative precision errors for future comparisons between normal and OA subchondral bone density. Third, our comprehensive analysis of precision using both $CV\%_{RMS}$ and ICC allows us to judge the reliability of observed density differences between OA and normal knees for each individual density measure. It is worthwhile to note that although ICCs provide a measure of reliability for density measures, they do not provide any information required for interpreting differences between OA and normal bone density. In order to ensure that observed density differences are due to OA and not technical limitations (e.g., precision errors), the quantity of the difference must be carefully interpreted in relation to corresponding quantitative precision errors such as SD_{RMS} or $CV\%_{RMS}$. In general, at least two SD_{RMS} or $CV\%_{RMS}$ above mean normal values should provide enough confidence (95% confidence) that a real difference or change exists. Our previous *ex vivo* results comparing normal and OA knees (Chapter 3) demonstrated BMD differences ~9x greater than observed *in vivo* precision errors.

This study has specific limitations relating to our study population and OA classification. First, though we have met recommendations by Glüer et al [133], our sample population contained seven OA (14 DOF) and seven normal knees (14 DOF). Our population also primarily contained middle-aged adults between 39 and 61 years of age. We had two younger females (23 and 34 years) and one older female (71 years) participant in this study. Establishing precision values for OA and normal populations independently would have doubled our sample population and unduly inflict radiation on additional participants. In our study we deliberately combined OA and normal knees to increase the variability of CT-TOMASD density measures. Our reported $CV\%_{RMS}$ and ICC precision errors therefore represent conservative assessments of CT-TOMASD precision for both OA and normal knees. Separate analyses of OA and healthy populations did, however, offer comparable precision errors and we believe our decision to combine both OA and healthy participants to meet recommendations by Glüer

et al [133] is warranted. A second limitation is that our OA categorization was not based upon clinical OA diagnosis but retrospective analyses of CT reconstruction images using KL grading [57]. Unfortunately, information regarding OA presence or severity was unavailable at the time of scanning. Clinical diagnoses were not included with this study because OA assessments typically require the participant to undergo a long-leg standing anteroposterior radiograph to define joint space width, which would increase effective radiation dosage on participating volunteers.

The CT-TOMASD technique has specific limitations that should be considered. First, the entire CT-TOMASD analysis for each knee takes 30-45 minutes to complete. We are presently developing new tools to automate the segmentation procedure, aiming to reduce the analysis time to 10-15 minutes per knee. Second, an inherent limitation of any QCT-based approach is that the participant is exposed to ionizing radiation. However, due to the low presence of radiosensitive tissues at the knee joint, QCT analyses at the knee joint result in a low effective dosage of ~0.073 mSv (estimated using shareware software: CT-DOSE; National Board of Health, Herley, Denmark). We were able to lower the *in vivo* dosage from 0.15 mSv (*ex vivo* dosage) by lowering the tube current to 150 mA.

4.6 Conclusions

In vivo CT-TOMASD regional density measures demonstrated $CV\%_{RMS}$ precision errors less than 3.9%, which suggests that the technique has the potential to identify and quantify changes in subchondral BMD associated with OA *in vivo*.

5 Predicting Subchondral Bone Stiffness using CT-TOMASD

5.1 Synopsis

This chapter describes our tests of the ability of CT-TOMASD layer analyses to predict, non-invasively, subchondral bone structural stiffness in OA and normal proximal tibiae. CT-TOMASD measures nearest the subchondral bone surface (0-2.5 mm) were significantly correlated with bone stiffness. Cartilage damage had no effect on stiffness-density relationships.

5.2 Introduction

OA-related subchondral bone changes are thought to initiate and accelerate cartilage degeneration by increasing the stiffness of subchondral bone. A stiffened subchondral bone will be less able to deform under dynamic impact loading (i.e., transfer strain energy), leading to more energy being transferred through the overlying cartilage. This would lead to higher internal cartilage stresses, cartilage breakdown, and eventual OA [2-4]. Cadaveric studies investigating the role of bone in OA have however offered conflicting findings, with one finding that OA subchondral bone is stiffer than normal [49], some finding it is less stiff than normal [48, 50, 51] and still others showing it is as stiff as normal subchondral bone [50, 52-55]. Unfortunately, subchondral bone stiffness cannot be measured directly from living bone. In order to better understand how mechanical properties change with OA disease progression and treatment, a surrogate *in vivo* measure of subchondral bone stiffness is required. This information could help explain the mechanical role of subchondral bone in OA initiation and progression and assist with treatment methods aimed at preventing or delaying OA onset.

One potential surrogate marker of subchondral bone stiffness is our CT-TOMASD imaging technique; a 3D imaging tool that characterizes and maps subchondral cortical and trabecular apparent BMD in relation to depth from the subchondral surface. Previous research has shown direct relationships between apparent density and bone material stiffness (modulus of elasticity, E) using

excised trabecular bone specimens from the proximal tibia [79, 82, 83, 89]. These stiffness-density relationships are typically characterized by the nonlinear power law function $E \propto BMD^{\gamma}$, with γ being approximately equal to 2 [79, 82, 83, 89]. Noninvasive estimates of subchondral bone stiffness could help explain the mechanical role of subchondral bone with OA more effectively than bone density alone. Currently, the relationship between the overall structural stiffness of subchondral bone with density measures that can be characterized *in vivo* with tools such as CT-TOMASD is not clear. It is also not clear how the disease state of the joint affects the relationship between apparent density and stiffness given that previous research has shown dissimilar stiffness-density relationships between OA and normal trabecular bone [49].

The primary objective of this study was to determine whether CT-TOMASD derived density measures could predict proximal tibial subchondral bone stiffness values obtained using *in situ* indentation testing. The secondary objective was to assess whether overlying cartilage degeneration (an indicator of OA) affected these predictions.

5.3 Methodology

5.3.1 Specimens

We obtained 13 intact fresh-frozen human cadaver knee specimens from 10 male donors (mean age ± standard deviation (SD): 73.2 ± 10.6, range: 51-88), including 3 left:right pairs, 1 right and 6 left knees. We previously used the cadaveric knees in related imaging studies whereby intact knees were thawed and imaged using QCT (Chapters 2 and 3). Following QCT imaging we exposed the knee joint and removed all soft tissue structures except cartilage and menisci. We transversely cut the proximal tibia 35 mm distal to the cartilage surface, then sagittally cut through the tibial spine to divide each proximal tibia into individual medial:lateral compartments. We selected one compartment from each knee which exhibited evidence of both normal and degenerated cartilage without erosion to the subchondral

surface, leaving 4 medial and 9 lateral compartments. We kept the compartments hydrated using phosphate buffered saline (PBS) (Sigma-Aldrich Inc., St. Louis, MO) during excision and sample preparation. Following excision we wrapped each compartment in PBS soaked towels, sealed them and stored them at −20 °C prior to testing.

5.3.2 Cartilage Degeneration Scoring

Cartilage degeneration was clinically evaluated by the participating surgeon (BAM) prior to sectioning tibiae into medial and lateral compartments using International Cartilage Repair Society (ICRS) recommendations based upon the Outerbridge score [58, 59] (Table 5-1). Each compartment had both normal regions (ICRS Grade 0) and regions with partial degeneration (ICRS Grades 1-3), though none exhibited complete cartilage erosion to subchondral bone (ICRS Grade 4) (Figure 5-1). There was no indication of submeniscal cartilage degeneration. We categorized cartilage status as normal (ICRS ≤ 1) or degenerated (ICRS > 1).

Table 5-1. International Cartilage Repair Society (ICRS) grading [58] based on Outerbridge score [59].

Grade	Property
0	Normal cartilage
1	Superficial lesions, fissures and cracks; softening
2	Fraying and fissuring; lesions extending <50% cartilage depth; lesions <0.5" diameter
3	Fraying and fissuring; lesions extending >50% cartilage depth; lesions >0.5" diameter
4	Erosion of cartilage down to bone

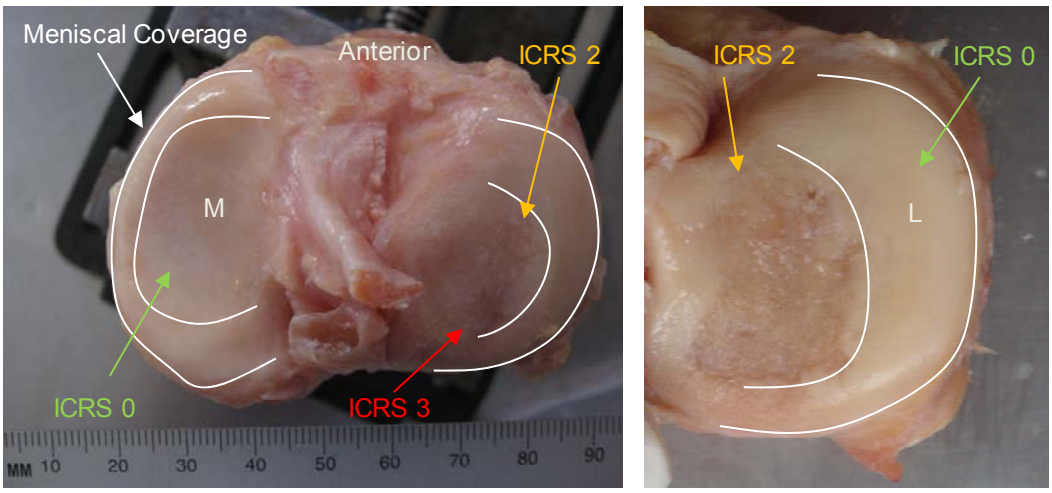

Figure 5-1. Examples of different cartilage gradings using the ICRS scoring system.

5.3.3 Specimen Preparation

We thawed a single compartment for 12 hours at 20 °C. We sealed the excised surfaces of the bone with a layer of polymethyacrylate bone cement (PMMA) (Fastray, Bosworth, Chicago, IL). We embedded (potted) the compartment in a potting system composed of an outer shell made of polyvinylchloride (PVC), a support base made of gypsum potting material (Denstone, Modern Materials Inc, South Bend, IN) and a layer of PMMA. While the gypsum was initially setting, we horizontally aligned the compartment cartilage surface using levels. We embedded the compartment in the potting material, leaving ~25 mm of exposed proximal tibial tissue. To mimic the structural support of the excised contralateral compartment we created a custom 'phantom' compartment out of PMMA, which was rigidly fixed to the PMMA potting layer and sealed surfaces of the tibial compartment (Figure 5-2).

To relate stiffness properties with CT-TOMASD measures of density, we set stainless steel fiducial markers (1 mm diameter) into the outer PVC shell [180]. We used a 1 mm diameter ball end-mill to create concave holes (~0.5 mm depth) within the PVC for the fiducials, and applied a temporary adhesive for fiducial fixation. We positioned the fiducials distal to the proximal tibia to prevent metal streaking artifacts from distorting imaged density. Following specimen preparation each potted tibial compartment was again sealed, then stored at 2 ^{o}C for a maximum period of 24 hours before testing.

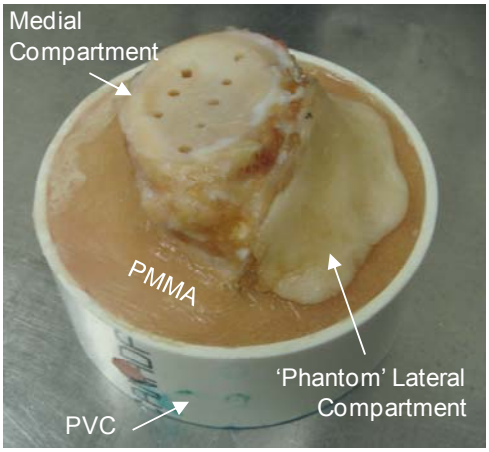

Figure 5-2. Photograph of potting system, including 'phantom' contralateral compartment.

5.3.4 QCT Image Acquisition

We imaged potted proximal tibial compartments using clinical CT (64-slice helical Aquilion 64, Toshiba Medical Systems, Tokyo, Japan) according to a previously validated QCT method [176, 181] (Figure 5-3). We included a solid QCT phantom (Model 3T; Mindways Software Inc, Austin, TX) within each CT image to convert CT grayscale intensity (Hounsfield units, HU), to equivalent volumetric apparent BMD (mg/cm^3 K_2HPO_4). Tibial compartments were centrally positioned within the CT gantry in a supine orientation. CT scanning parameters included: 120 kVp tube voltage, 300 mA tube current, bone standard reconstruction algorithm, axial scanning plane, 0.5 isotropic voxel size (0.5 mm slice thickness, 0.5 x 0.5 mm in-plane pixel resolution).

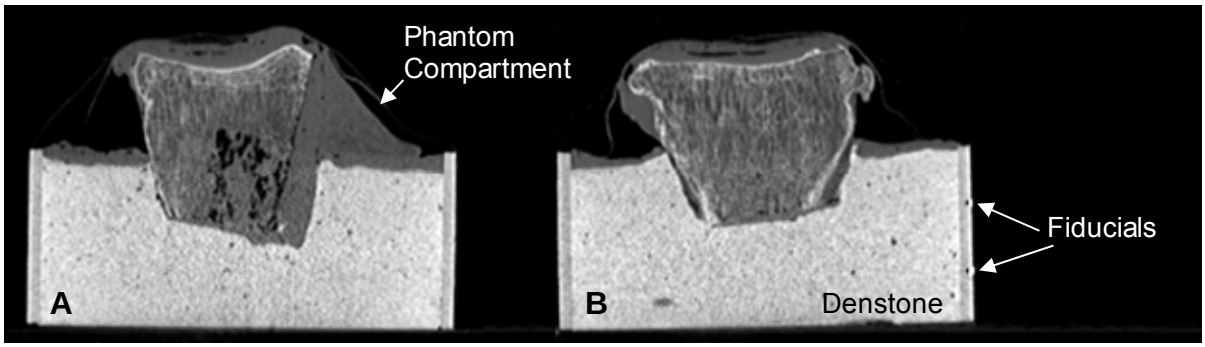

Figure 5-3. *A*, Coronal reconstruction of QCT imaged medial compartment + phantom lateral compartment. *B*, Sagittal reconstruction of QCT imaged medial compartment, illustrating placement of fiduciary markers distal to the proximal tibial compartment to prevent metal streaking artifacts from affecting imaged density.

5.3.5 Mechanical Indentation Testing

We obtained subchondral bone mechanical properties using a novel mechanical indentation test (Figure 5-4). The mechanical indentation testing apparatus was comprised of a right angle drill and loadcell (250 N, accuracy: ± 0.1 N, LC101-50, Omega Engineering, Stamford, CT) mounted to a material testing system (Instron 8874, Instron Corp., Canton, MA). The material testing system provided computer-controlled vertical displacement of the indentor while load was continuously monitored at 1000 Hz using custom analysis software (LabView, National Instruments, Austin, TX). The right angle drill was required for iterative milling. A 5 degree-of-freedom (DOF) stage was used to control tibial compartment rotation and translation. We rigidly attached the potted tibial compartment to the 5 DOF positioning stage and horizontally oriented the cartilage surface. We removed the fiducials from the PVC shell and physically located the concave fiducial holes, indentor tip and xyz axes of the test setup using an optoelectronic motion tracking system (NDI, Waterloo, ON, Canada) and 3D digitizer fit with a 1 mm diameter spherical tip (± 0.100 mm accuracy). A re-circulating drip containing 37^{o}C PBS hydrated the potted tibial compartment.

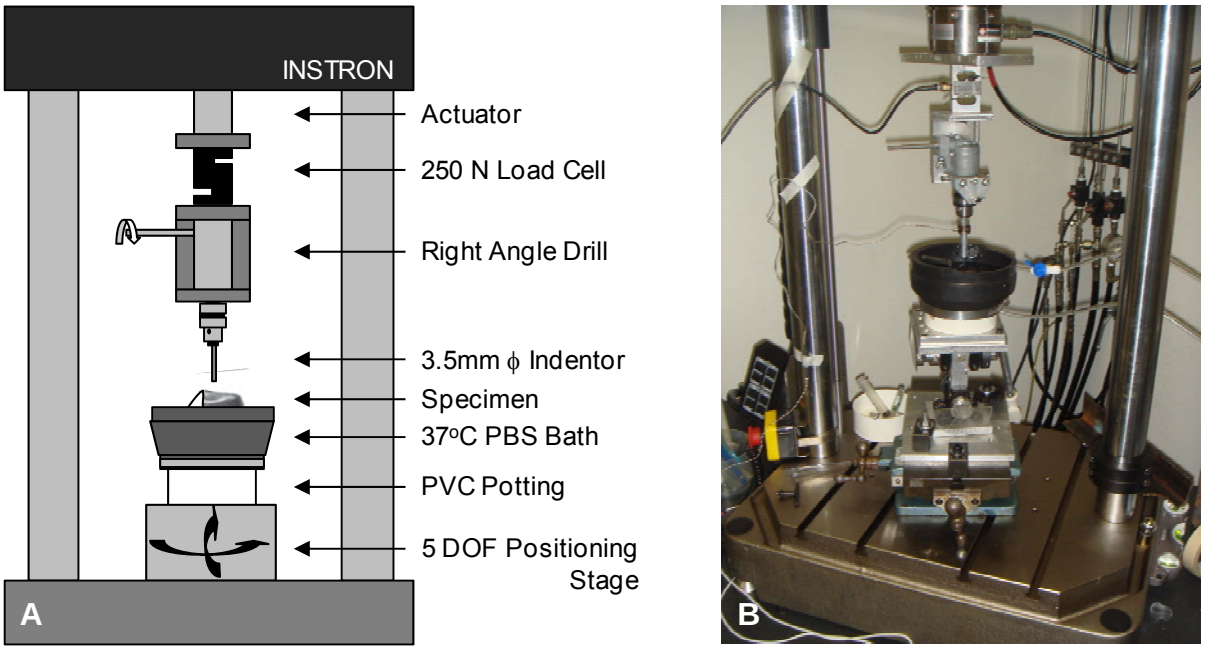

Figure 5-4. *A*, Schematic diagram of material testing setup. The test combines compressive indentation with iterative milling to characterize subchondral bone stiffness. The testing apparatus was comprised of a right angle drill and 250 N loadcell mounted to an Instron material testing system. The right angle drill permitted iterative milling while the accompanying chuck allowed indentors and end mill bits to be quickly interchanged. A 5 degree-of-freedom (DOF) stage was used to control tibial compartment rotation and translation. A re-circulating drip containing 37°C phosphate buffered saline (PBS) provided constant hydration during testing. *B*, Photograph of the material testing setup. In this photo a cartilage indentor is mounted to the right angle drill instead of a 3.5 mm diameter indentor. For reference, the total distance between the actuator and the indentor tip was 24.9 cm.

We defined test sites on each compartment according to anterior-posterior and central-peripheral dimensions (Figure 5-5). The spacing between test sites and the peripheral edge was > 7 mm, which allowed at least 3 mm clearance between adjacent test sites to avoid interference arising from damage to surrounding bone [120]. For this study we focused our analyses on sites not completely covered by the meniscus since there was no evidence of submeniscal cartilage degeneration. At the medial plateau our analyses were focused anteriorly and centrally (6 sites / compartment). Of the 24 medial test sites, 2 were excluded due to high surface curvature (> 10^{o} inclination). From the remaining 22 test sites, 11 exhibited normal to minimal cartilage degeneration (ICRS 0-1); 11 exhibited moderate degeneration (ICRS 2-3). At the lateral plateau our analyses were focused centrally (4 sites / compartment). Of the 36 test sites, 2 were excluded due to high surface curvature; 5 were excluded due to meniscal coverage. From the remaining 29 test sites, 15 exhibited normal to minimal cartilage degeneration; 14 exhibited moderate degeneration.

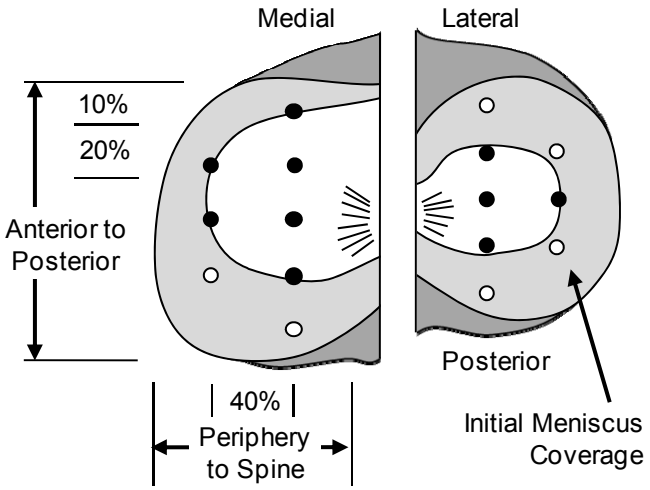

Figure 5-5. Schematic diagram of the test site locations. The test sites coordinates were defined based on the anterior-posterior and peripheral-spine dimensions of the compartment. The anterior-posterior dimension was divided into increments of 20%, leaving 10% at the ends. The central-peripheral dimension was divided into increments of 30, 40 and 30%. This left a minimum 7 mm center-to-center between test sites and a minimum 3 mm between the edges of the test holes. For this study only the black test sites were included in the analysis. The white test sites correspond to submeniscal locations.

At each test site we determined the depth of the subchondral bone surface using a compressive needle indentation test [182] (Figure 5-6-A). Starting at the cartilage surface, we slowly lowered the needle (0.1 mm/s) while monitoring the load response and identified the subchondral surface as the position where the load-time curve increased abruptly (Figure 5-6-B). On average, the load at test stoppage was -5 N. Needle displacement beyond our defined subchondral surface did not exceed 0.1 mm. We determined the repeatability of the defined subchondral surface location by defining the location of the subchondral surface at 4 sites around the initial test site, ± 1 mm in the anterior-posterior and medial-lateral directions [182], at ten sites from three specimens. Precision errors associated with the defined subchondral surface location were less than 5% (CV%). We estimated a maximum cartilage thickness error of +0.1 mm based upon pilot tests comparing needle-defined cartilage thickness with physical caliper measures after sectioning.

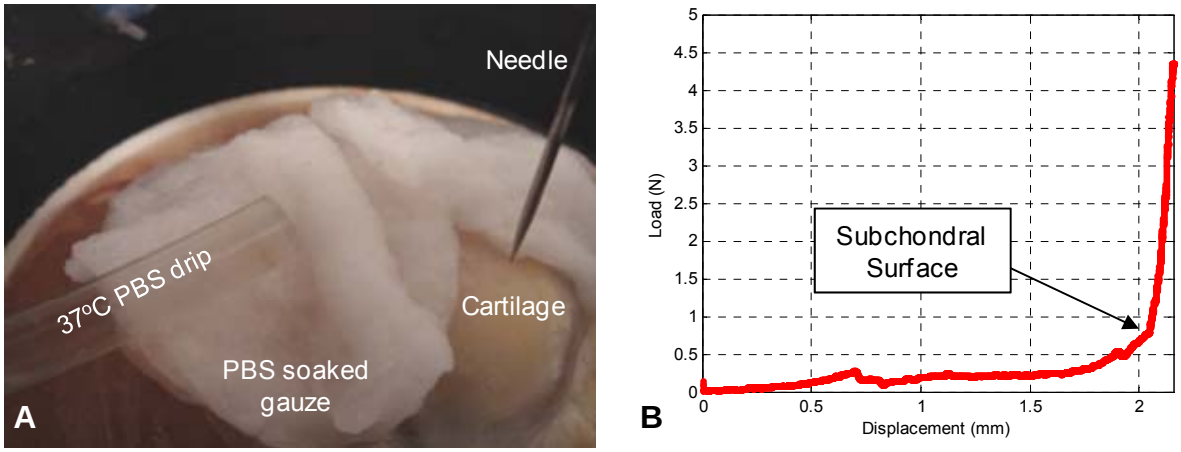

Figure 5-6. A, Photograph of specimen prior to needle indentation test. B, Typical load-displacement curve during needle indentation testing. An abrupt change in load indicates that the subchondral bone surface has been reached.

We milled with a 4 mm diameter flat endmill from the cartilage surface to 0.100 mm beyond our defined subchondral surface to create a flat indentation test surface. Displacement of the endmill was controlled by the testing machine while the drill was manually operated (1500 rpm). We minimized endmill deviation using a mill guide rigidly attached to the material testing system with a 4 mm diameter hole in line with the milling axis (Figure 5-7). During milling we temporarily increased the flow rate of our re-circulating drip to provide a constant supply of PBS at the milling site. Following milling, we used suction to remove bone and cartilage remnants.

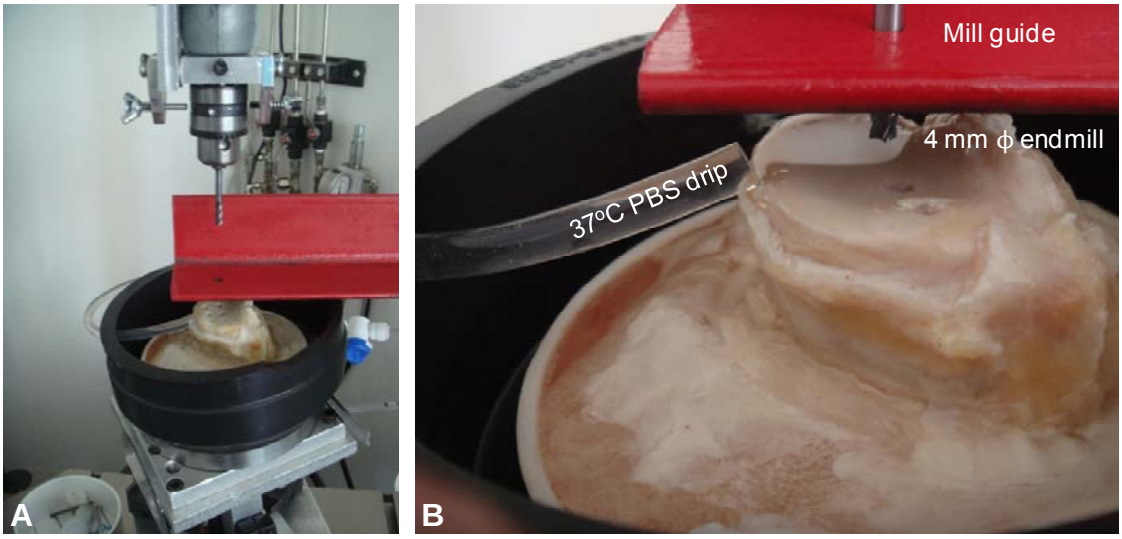

Figure 5-7. *A*, Photograph of material testing system with 4 mm diameter endmill and mill guide. *B,* Magnified view of endmill within the mill guide, which is rigidly attached to the frame of the Instron testing machine.

We performed indentation testing with a 3.5 mm diameter flat-ended nonporous indentor at 2 mm/minute, and stopped the test when indentor displacement reached 0.500 mm or load reached 250 N. We report structural stiffness using the Timoshenko-Goodier equation for indentation [129] commonly used for studies of subchondral bone stiffness [55, 120, 122, 127, 128]. The Timoshenko-Goodier equation is expressed as:

$$E = k \cdot \frac{(1 - v^2)}{2r}$$

where ν is Poisson's ratio (υ = 0.3 [120, 183]), *r* is the radius of the indentor (1.75 mm), *k* is the slope of the load-displacement curve (N/mm), and *E* is the local modulus of elasticity (MPa) which we refer to as structural stiffness. We measured the slope from the most linear portions of the load-displacement curve prior to test stoppage using custom algorithms (Matlab). The linear region included approximately 0.125 to 0.225 mm of displacement data (3750-6750 data points) with an $r^2 > 0.99$ (Figure 5-8). The recorded deformation used to define stiffness included the deformation of subchondral cortical, subchondral trabecular and epiphyseal trabecular bone. Therefore, although we define stiffness using the modulus of elasticity *E,* which is generally regarded as a definition for material stiffness, our results pertain to the overall structural stiffness of subchondral bone.

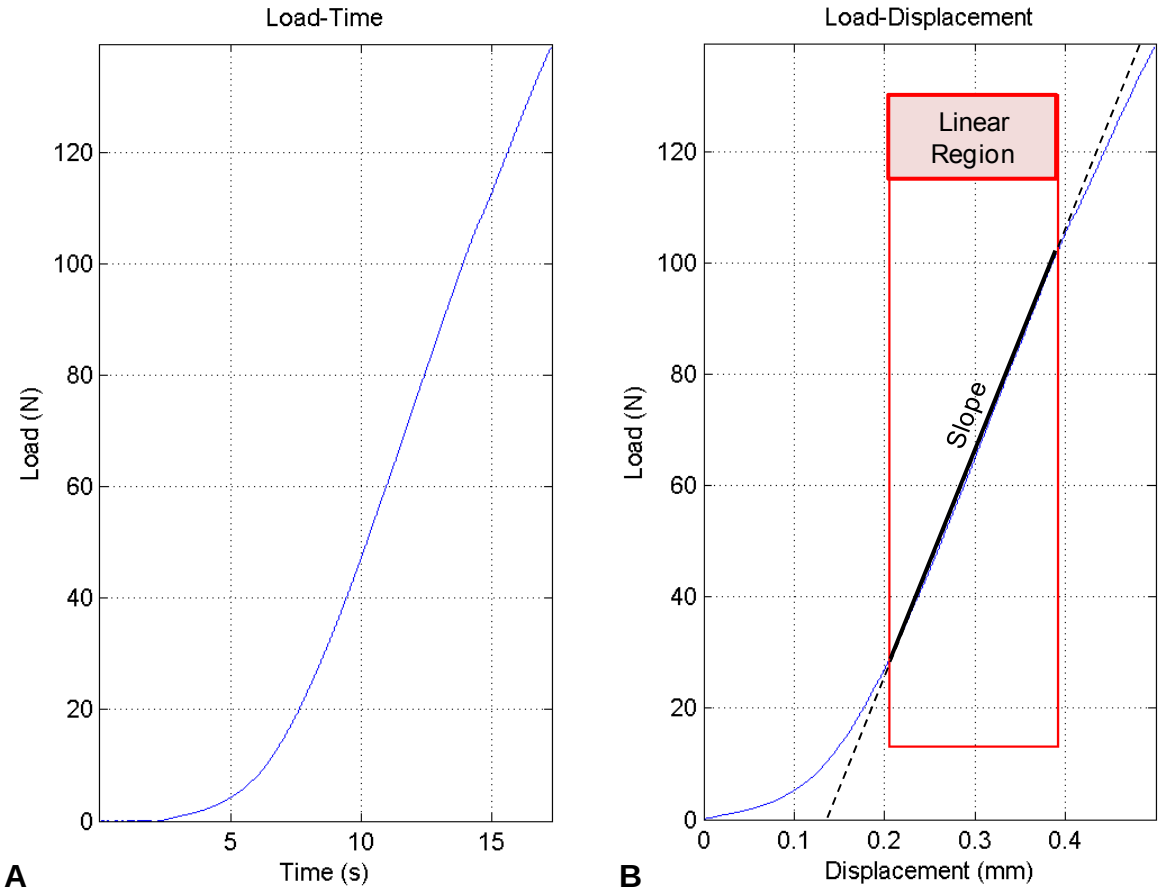

Figure 5-8. *A*, Matlab plot of a typical load-time curve during subchondral bone indentation testing. *B*, Matlab plot of a typical load-displacement curve during indentation testing. The data within the linear region was used to define the slope of the load-displacement curve.

5.3.6 Registration of Indentation and Imaging Data

Following mechanical testing we registered (matched) the imaged fiducial coordinates and physical fiducial coordinates [180], then reconstructed the imaged potted compartment using cubic interpolation to match the physical orientation within the material testing apparatus (Matlab). Using the previously defined digitized coordinates of the indentor tip and axes of the mechanical test setup, we replicated the mechanical indentation test setup within the imaged 3D space. Using the known coordinates of the indentor at each test location, we directly related QCT imaged subchondral bone density with structural stiffness. The overall cumulative error associated with the registration process was less than 0.25 mm, which was smaller than our CT voxel.

5.3.7 CT-TOMASD Image Analysis

At each indentation test site we performed CT-TOMASD depth-specific layer analyses using a 3.5 mm diameter region of interest matching the indentor size (Matlab) (Figure 5-9). We determined average density across various layers measured in relation to depth from the subchondral surface (0-2.5, 0-5, 0-10, 2.5-5, 5-10 mm). To account for differences in physical size, we controlled the depth measure for each subject using relative tibial volumes, plateau areas, and a user-defined normalized depth. To account for registration errors we tested the precision of CT-TOMASD measures by comparing results with neighboring densities ±1 voxel (±0.5 mm) in the anterior-posterior and central-peripheral directions. For all indentation test sites, precision errors associated with CT-TOMASD measures were less than 6%.

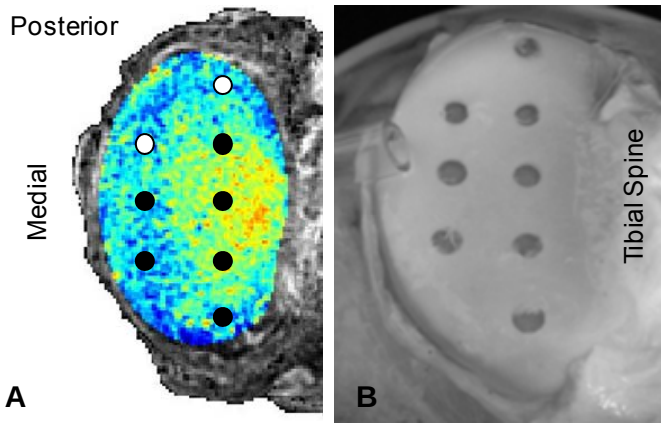

Figure 5-9. *A*, CT-TOMASD depth-specific layer analyses to a depth of 2.5mm from the subchondral surface using a 3.5 mm diameter region of interest matching the indentor size. Density colormap pertains to high (red) and low (blue) measures of BMD. For this study only the black test sites were included in the analysis. *B*, Indentation test sites at the medial plateau used for co-registration with CT-TOMASD layer analyses.

5.3.8 Statistical Analysis

We verified equality of variances with Levene's test and normality of data distribution with Q-Q plots. We used hierarchical nonlinear power-law regression models to examine the relationship between CT-TOMASD measures of density and structural stiffness. We characterized associations between density and stiffness using scatter plots and report coefficients of determination (r^2) for the regression models. For Objective 1 the model included age and side (medial:lateral) as fixed factors. For Objective 2 we added cartilage status (normal or degenerated) as a fixed factor to the model. If cartilage degeneration had no effect on model predictions, we also tested the overall coincidence of separate regression models using F test statistics [184]. This analysis tests whether fitting separate stiffness-density regression curves to normal and OA datasets more effectively predicts stiffness than a single stiffness-density curve fit to both datasets. Statistical analyses were performed using commercial software (Matlab 2007a and SPSS 18; SPSS Inc, Chicago, IL).

5.4 Results

Statistical analyses indicated that side did not affect stiffness or density measures; therefore we pooled results from medial:lateral compartments. The mean, SD and range of structural stiffness were 452 ± 275 MPa (range: 75-1140 MPa).

CT-TOMASD measures nearest the subchondral bone surface (0-2.5 mm) were most effective at predicting subchondral bone stiffness (r^2 = 0.67, $p < 0.001$), and the predictive ability decreased when density was averaged across larger depths (Table 5-2). CT-TOMASD measures across layers distal to the subchondral surface also explained less variance in stiffness (Table 5-2). For all depths and layers, adjusting for side and age did not improve model predictions.

Inclusion of cartilage status had no effect on model predictions. An overall test for coincidence revealed that a single stiffness-density curve explained more variation in stiffness values than separate curves for normal and damaged tissue ($p > 0.05$) (Figure 5-10).

Table 5-2. Mean ± SD measures of BMD proximal tibial compartments using the CT-TOMASD imaging technique. Density results pertain to 51 total measures from 13 proximal tibial compartments (4 medial, 9 lateral) from 10 male subjects. Density measures were correlated with subchondral bone structural stiffness measures using non-linear power-law regression, with determination coefficients (r^2) and p-values reported.

		BMD (mg/cm^3 K_2HPO_4)	Stiffness-BMD Relationships	
CT-TOMASD		Mean ± SD	r^2	p-value
Proximal Measure	0 - 2.5 mm	432 ± 111	0.67	< 0.001
	0 - 5 mm	348 ± 95	0.63	< 0.001
	0 - 10 mm	237 ± 76	0.48	< 0.001
Distal Measure	2.5 - 5 mm	263 ± 88	0.41	< 0.001
	5 - 10 mm	131 ± 63	0.10	0.017

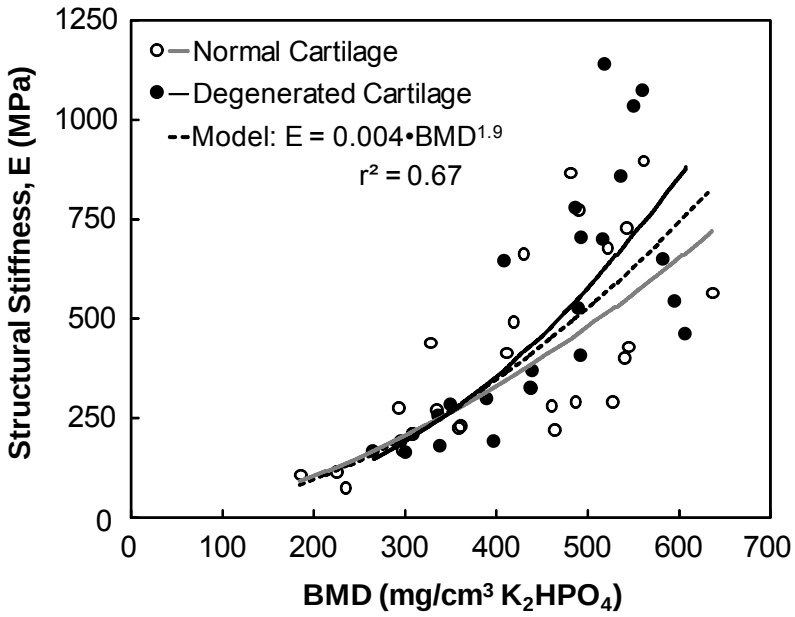

Figure 5-10. Nonlinear power-law regression relationships between subchondral bone structural stiffness and CT-TOMASD measures of bone density to a depth of 2.5 mm from the subchondral surface. The stiffness-density relationship is provided for all measures of density and stiffness (51 test sites from 13 compartments). Separate stiffness-density relationships are plotted for subchondral bone underlying normal (grey) and degenerated cartilage (black) regions. F-test statistics showed that normal and degenerated curves did not significantly differ from the single curve (dashed) representing both datasets.

5.5 Discussion

The structural stiffness of subchondral bone depends upon subchondral cortical and subchondral trabecular bone material density and related material stiffness properties, cortical bone thickness, trabecular bone volume and trabecular bone architecture. Thus, the proficiency of CT-TOMASD at predicting stiffness is likely due to apparent BMD measures combining bone material density, bone volume and thickness. Apparent BMD (bone mass / total volume) reflects both the degree of mineralization (material density = bone mass / bone volume) and quantity of bone within a fixed total volume (bone volume fraction = bone volume / total volume). Apparent BMD will increase in response to either an increase in tissue mineralization or an increase in bone volume. By measuring apparent BMD in relation to depth from the subchondral surface (i.e., thickness), CT-TOMASD pools numerous

individual factors associated with stiffness into a single imaged structural measure able to predict a large variation of our structural stiffness measures.

Our finding that CT-TOMASD measures near the subchondral surface (0-2.5, 0-5 mm) were most effective at predicting subchondral bone structural stiffness are consistent with earlier findings. An indentation test at the proximal tibia showed that bone located less than 5 mm from the subchondral surface offered maximum resistance to failure loading [90]. Penetration tests immediately below subchondral cortical bone showed that the most proximal bone offered the greatest resistance to penetration loading [92, 110, 167]. These findings suggest that subchondral cortical and subchondral trabecular bone located nearest the subchondral surface (< 5 mm) are the primary constituents comprising the structural stiffness of subchondral bone.

It is not surprising that CT-TOMASD measures distal to the subchondral surface (0-10, 2.5-10, 5-10 mm layers) were less effective at predicting subchondral bone structural stiffness. The most likely explanation is that epiphyseal trabecular bone distal to the subchondral surface (> 5 mm) simply has little direct effect on overlying structural stiffness. This may be particularly evident with OA because epiphyseal trabecular bone exhibits reduced trabecular thickness [27, 73, 93, 94] and reduced apparent density with OA [28, 137, 138, 160], to the point of being labeled osteoporotic [73]. Epiphyseal trabecular bone changes observed with OA are believed to result from a 'stress shielding' effect caused by stiffer overlying subchondral bone [27, 93]. It has been suggested that a stiffened subchondral bone would transmit less load to the underlying epiphyseal trabecular bone, leading to bone resorption and localized osteoporosis.

Our finding that cartilage damage does not have an effect on CT-TOMASD derived stiffness-density relationships is important because it suggests that we can noninvasively estimate subchondral bone stiffness for both healthy and OA individuals (clinical and subclinical) to better understand the role of bone in OA. This finding differs from research of late-OA femoral heads where the slope of the

material stiffness-density curve for OA trabecular bone was less that of normal bone [49]. Differing stiffness-density relationships were explained by an accelerated bone turnover rate for OA trabecular bone resulting in hypomineralization [48, 49, 74] and a reduced material density [18, 77]. However, these changes may be offset by greater cortical bone thickness [73] and trabecular bone volume [14, 15, 54, 75] consistent with OA, resulting in a structural stiffness meeting or exceeding normal values [18, 48]. The net effects of possible altered material density, bone volume and thickness appear to be pooled together by CT-TOMASD, leading to similar stiffness-density relationships for both OA and normal bone.

A key strength of this study is that we used a clinical QCT imaging protocol to measure subchondral bone density and relate with physical measures of structural stiffness, which allows assessments to be made *in vivo*. A second strength is that our novel *in situ* indentation test measured the structural stiffness of subchondral bone directly at the bone surface, likely producing a measure of bone stiffness most relevant in studies of OA progression. Compared with compression testing of isolated specimens of subchondral cortical or trabecular bone, *in situ* indentation testing is more representative of the *in vivo* condition [119] and may more accurately reflect bone's response to articular cartilage loading. A third strength is that we compared subchondral bone stiffness and density from sites underlying normal and degenerated cartilage from the same sample group, thereby minimizing variability between different individuals. A fourth strength is that we compared the effects of cartilage degeneration on model predictions using both hierarchical regression models and F test statistics, therefore strengthening our observation that cartilage degeneration had no effect on stiffness-density relationships.

This study has limitations related to OA categorizations and sample population sizes. First, we were unable to obtain tissue from joints completely unaffected by OA. We were therefore unable to develop separate stiffness-density curves for OA and normal tissue from entirely different sample

populations. To separate normal and OA bone, we selected compartments exhibiting both normal and damaged cartilage and interpreted the damaged cartilage to be representative of an early-OA to moderate-OA population. Similarly, we interpreted regions with no apparent cartilage damage to be representative of healthy cartilage. These interpretations are reasonable given that knee OA is generally regarded as a localized disease [185] and it is unlikely that all cartilage and subchondral bone tissues will be equally affected by the disease in early stages. By comparing normal and damaged samples from the same subjects, we were able to avoid variability between different subjects and focus solely on the effects of cartilage damage upon stiffness-density relationships. In cadaver studies there will always be doubt as to how "normal" or "OA" samples truly are because OA is a clinical diagnosis in a living patient. Therefore, we believe our comparison of normal and damaged cartilage from same subjects was justified. Though unlikely, it is however possible that the reason why cartilage degeneration had no effect on stiffness-density relationships was because our entire sample population represented either purely normal or purely OA tissue. Comparisons of OA and normal stiffness-density relationships from completely different sample populations may reveal that cartilage degeneration does have an effect on stiffness-density relationships. Second, many of our medial compartments had end-stage OA (ICRS = 4), therefore our sample primarily included lateral compartments. However, we had good variability of density and material properties for forming associations between density and stiffness. It is possible, however, that a larger sample population containing equal quantities of medial and lateral compartments may have led to side having an effect on model predictions, particularly since previous studies have shown stiffness, strength and density to be greater in the medial compartment [11, 26, 55, 90, 167, 186, 187].

The mechanical test has potential limitations related to the use of a needle test to define the subchondral surface, the type and depth of testing, surface inclination, test site spacing, and machine stiffness corrections. First, our rationale for using a compressive needle indentation test [182]—as

opposed to complete removal of the cartilage surface—was that we wished to maintain as much joint integrity as possible and in particular keep the articular cartilage structure intact for associated studies assessing links between bone and cartilage. This was because, in addition to characterizations of subchondral bone structural stiffness, the mechanical indentation test was used to characterize the stiffness of overlying cartilage and underlying trabecular bone at staged depths from the subchondral surface (medial compartments only)†. There is some potential for error associated with this choice, specifically regarding incorrect surface definition due to bone porosity and/or weak bone stiffness, though we believe these errors are minimal. To address this issue, during testing we verified cortical surface presence both visually and manually using tactile feedback (e.g., "poking" with needle; "knocking" with blunt-ended forceps) and reviewed the position of the indentor in the reconstructed CT images. In all instances the indentor was located directly above CT voxels with the highest density or contained within voxels noticeably influenced by partial volume effects, indicating that the cortical surface was correctly defined. Precision errors associated with the defined subchondral surface location were less than 5%; therefore possible bone porosity did not appear to have a large effect on surface definition. Pilot tests indicated that needle-measured thickness was within 0.100 mm of caliper measured thickness; therefore bone stiffness did not appear to have a large effect on surface definition. Although sectioning could have been used to verify bone surface position, we decided against sectioning due to anticipated future research assessing lateral compartment stiffness at staged depths from the subchondral surface. Although it is possible that some stiffness measures were improperly estimated due to incorrect surface definition, stiffness-density relationships should not be significantly affected. This is because we directly related the position of our indenter, regardless of correct or incorrect surface definition, with imaged subchondral bone densities. We also used multiple tests (n=51) to define stiffness-density relationships and relatively large regions of interest to define density

† Results of cartilage testing and staged depth testing are outside the scope of this thesis.

(185 voxels within the 3.5 mm diameter ROI; 2.5 mm depth). Incorrect surface definition could however help explain the large variability in stiffness measures, although large variability is a finding common with mechanical tests of bone (Chapter 1 - Table 1-7). Second, the needle test may have damaged the subchondral bone surface due to delayed test stoppage after the surface had been reached, leading to plastic damage and mechanically altered stiffness. However, the average load at test stoppage was about 5 N, which was within the nonlinear "toe" region of the load-deformation curve and plastic damage would therefore be minimal. Any incurred plastic damage would be highly localized around the small needle tip and primarily limited to depths beyond the subchondral surface (< 0.100 mm). By milling 0.100 mm beyond the defined subchondral surface we aimed to eliminate possible plastic damage acquired during needle testing and simultaneously create a flat surface for macro indentation testing. Third, we did not indent to failure because a limited number of our specimens underwent further indentation testing at staged depths from the subchondral surface (results not reported). Failure testing would have induced plastic damage at these depths. However, other subchondral bone indentation studies have indented to a depth of 0.5 mm [55, 122, 124]. Fourth, the subchondral bone surface was not aligned perfectly perpendicular with the indentation axis of the material testing system due to natural curvature. We attempted to minimize negative effects of excessive surface inclination by excluding stiffness results from sites exhibiting inclinations greater than 10^{o}, as measured from sagittal and coronal CT reconstructions. Fifth, indentation testing of numerous test sites on each compartment could have detrimental effects on stiffness values obtained from adjacent sites. However, published histological observations have shown that sideways disturbances are contained within 0.2 mm of the side of the indentor [120]; much less than our minimum 3 mm clearance between test sites. Sixth, because recorded test deformation included deformation of the proximal tibia, testing apparatus and load cell, estimates of bone stiffness had to be corrected using the following "series of springs" relationship:

$$\frac{1}{k_{TEST}} = \frac{1}{k_{BONE}} + \frac{1}{k_{APPARATUS}} + \frac{1}{k_{LOAD\ CELL}}$$

where k_{TEST} is the measured test stiffness, k_{BONE} is the stiffness used to determine the structural stiffness of subchondral bone, $k_{APPARATUS}$ is the stiffness of the indentation testing apparatus (~6950 N/mm) and $k_{LOAD\ CELL}$ is the stiffness of the load cell (875 N/mm). Load cell stiffness was not markedly greater than measured test stiffness, and this had a major effect on corrected bone stiffness. As an example, the maximum measured k_{TEST} was 660 N/mm which provided a corrected k_{BONE} equal to 4383 N/mm (E_{BONE} = 1140 MPa). If k_{TEST} was incorrectly overestimated by 1% (k_{TEST} = 666.6 N/mm), the corrected bone stiffness would change by 7% (corrected k_{BONE} = 4692 N/mm; E_{BONE} = 1220 MPa). However, precision errors associated with measured test stiffness were less than 1% and the majority of k_{TEST} measures were focused between 350 and 550 N/mm, which would have less impact on corrected bone stiffness (e.g., 1% overestimation in k_{TEST} from 350 to 353.5 N/mm or 550 to 555.5 N/mm would change k_{BONE} by 1.8% and 3.5%, respectively). Given that our structural stiffness measures were comparable with previous findings for proximal tibia subchondral cortical bone and trabecular bone, we are confident that reported stiffness measures reflect the mechanical properties of subchondral bone at the proximal tibia. Our rationale for using a 250 N S-type load cell was because 1) we required a load cell with high accuracy over a loading range of 0–250 N for both needle and bone indentation testing, 2) the load cell could be rigidly fixed for milling by inserting spacers within the gaps of the "S" load-cell ($k_{LOAD\ CELL} = \infty$), and 3) the load-cell was readily available in the research laboratory. For future research, 500 N (e.g., Omega LC101-100; $k_{LOAD\ CELL} \approx$ 1750 N/mm) or 1000 N (e.g., Omega LC101-250; $k_{LOAD\ CELL} \approx$ 4400 N/mm) S-type load cells may be more appropriate choices due to greater stiffness. However, greater load cell stiffness would require reduced load accuracy‡ and surface

‡ Load cell accuracy generally pertains to a percentage of full scale load (e.g., ±0.03% of 250 N). The greater the loading range, the poorer the accuracy.

overshooting during needle testing due to reduced proficiency at detecting when the subchondral bone surface had been reached.

Limitations pertaining to the CT-TOMASD imaging method have been discussed in detail previously (Chapters 2-4). For this study, the primary limitations pertain to imaged resolution and air presence. Our imaged 0.5 mm isotropic voxel resolution, which is currently one of the best clinically available isotropic resolutions for QCT imaging of bone, is relatively large. We aimed to replicate a clinical QCT imaging scenario with the knee in a supine position, and are therefore limited by the slice thickness capabilities of the CT machine. Due to this constraint there is some inherent inaccuracy in the imaged density at the subchondral surface due to partial volume effects. Air pocket presence near the subchondral surface may have distorted CT-TOMASD measured density, thereby affecting stiffness-density relationships. However, nearly all air pockets observed in QCT images (Figure 5-3-A) were located distal to the subchondral surface (> 10 mm) in metaphyseal trabecular bone regions, and were therefore not included in CT-TOMASD layer analyses. Of the 51 test sites used to establish stiffness-density relationships, minimal-to-moderate air presence was observed at 3 test sites. However, exclusion of these 3 test sites from the analysis did not affect stiffness-density relationships, and were therefore retained in this study.

5.6 Conclusions

CT-TOMASD measures nearest to the subchondral surface (0-2.5 mm) were most effective at predicting subchondral bone stiffness. The predictive ability of CT-TOMASD decreased as density was averaged across larger depths and layers deep to the subchondral surface. Cartilage damage did not affect stiffness-density relationships. CT-TOMASD has potential use as an *in vivo* imaging tool for characterizing subchondral bone density and estimating stiffness. This information could help explain the role of subchondral bone in OA initiation and progression.

6 Discussion

6.1 Overview of Findings

Subchondral bone is intricately involved in the progression of OA [2, 4, 17, 18, 29]. However, the exact role of subchondral bone with OA is unclear. It is believed that mechanical and morphological bone changes near the subchondral bone surface play a role in OA onset and progression [2-4, 13, 15, 17-20, 29]. Currently, much of our understanding of OA-related subchondral bone changes has come from animal models or cadaveric tissues instead of people living with OA. There is a need for a non-invasive tool to assess subchondral bone changes in living people. Previous *in vivo* studies examining direct associations between proximal tibial BMD—a surrogate measure of subchondral bone stiffness—and knee OA and offer conflicting conclusions [10, 12, 21-28]. We believe these conflicting conclusions are due to the limitations of available imaging techniques and selected analysis regions containing subchondral cortical, subchondral trabecular and/or epiphyseal trabecular bone; each of which may be affected differently by OA. CT-TOMASD is capable of precisely imaging thin layers near the subchondral bone surface for separate analyses of subchondral cortical, subchondral trabecular and epiphyseal trabecular bone density. The 3D CT-TOMASD imaging method does not suffer the limitations of currently available imaging techniques such as DXA (limited to 2D analyses, unable to distinguish trabecular from cortical bone), pQCT (limited to single CT slices, imaged density dependent upon subject positioning), MRI (unable to depict bone mineralization) or CT-OAM (limited to analyses of subchondral cortical bone density). In addition to density, CT-TOMASD can be used to non-invasively predict subchondral bone structural stiffness directly at the subchondral surface, which is most relevant to the OA disease process. Non-invasive stiffness predictions can be used to directly test hypotheses regarding the mechanical role of subchondral bone in OA. CT-TOMASD characterizations of OA and normal bone density and stiffness may help explain the role of

subchondral bone in the initiation, progression and treatment of OA. This information is vital to improving OA prevention, diagnosis and treatment.

A key accomplishment of Chapter 2 – CT-TOMASD Methodological Development and Preliminary Findings was that we developed a new non-invasive imaging tool for characterizing proximal tibial subchondral bone density patterns. This development was important because it provided a means to characterize the 3D density of thin subchondral layers near the subchondral surface to better understand bone changes occurring with OA. In particular, CT-TOMASD offers an alternative to existing subchondral bone imaging tools largely limited to 2D analyses (e.g., DXA and FSA), assessments of epiphyseal trabecular bone regions (e.g., pQCT, MRI and FSA) and an imaged dependence upon correct patient positioning (almost all existing subchondral bone imaging tools are influenced by patient positioning errors, including DXA, FSA, MRI and pQCT). A second key accomplishment of Chapter 2 was that we demonstrated that CT-TOMASD offers small precision errors (CV% < 3.5 %) for measures of proximal tibial subchondral bone density many times smaller than variability in the normal population and many times smaller than observed differences between normal, early-OA and late-OA density. This *ex vivo* precision study was important because it helped us test the potential usefulness of CT-TOMASD for distinguishing OA and normal density by proving that observed density differences between OA and normal knees were due to OA processes, not imaging artifacts. A third key accomplishment of Chapter 2 was that we demonstrated the ability of CT-TOMASD to discriminate between OA and normal subchondral bone density patterns using isolated comparisons of normal, early-OA and late-OA knees. This is an important aspect of this study because it demonstrated potential for assessing subchondral bone density in individuals living with OA. Without this information, there would be little reason to consider using CT-TOMASD to assess and compare OA and normal proximal tibial subchondral bone density.

A key accomplishment of Chapter 3 – Comparison of CT-OAM and CT-TOMASD was that we presented, for the first time, a comparison of OA and normal proximal tibial subchondral density obtained using clinical QCT. A second key accomplishment of Chapter 3 was that we demonstrated CT-TOMASD layer analyses were more proficient than CT-OAM maximum intensity projections for distinguishing OA from normal density. This study was required to 1) test the proficiency of CT-TOMASD at differentiating OA from normal density, 2) test the proficiency of CT-OAM at differentiating OA from normal density, 3) distinguish the CT-TOMASD imaging technique from CT-OAM, and 4) verify speculation that CT-OAM analyses of proximal tibial bone density focus on subchondral cortical bone density. Without this knowledge, the CT-TOMASD technique would only offer 'promise' as an imaging tool capable of differentiating OA from normal bone density and researchers would have little reason to use CT-TOMASD in place of the existing CT-OAM technique for assessments of OA and normal proximal tibial subchondral bone density. A second accomplishment of Chapter 3 was that we demonstrated OA bone density nearest the subchondral surface (< 5 mm) was markedly higher than normal. This is an important finding because it highlights the importance of imaging distinct layers and ROIs near the subchondral surface as opposed to large ROIs containing subchondral cortical, subchondral trabecular and epiphyseal trabecular bone density. Large ROIs containing all three bony tissues will have a diminished proficiency at recognizing density differences between OA and normal proximal tibial subchondral bone, which could partially explain conflicting findings in the literature.

The key accomplishment of Chapter 4 – *In Vivo* Precision of CT-TOMASD was that we demonstrated CT-TOMASD could be used to measure, *in vivo*, proximal tibial subchondral bone density in OA and normal knees with precision errors many times smaller than differences between OA and normal density (~9x smaller). This is an important finding because we can now assess subchondral bone density in individuals living with OA with minimal concern that observed density changes, or differences between OA and normal knees, are due to imaging artifacts as opposed to

disease processes. *Ex vivo* precision measurement was conducted before *in vivo* measurement because it would be unethical to expose study participants to (nominal) CT radiation without first gauging the potential usefulness of CT-TOMASD for distinguishing OA and normal density. Once we established that CT-TOMASD measures of subchondral density were markedly greater in OA knees (+36%) and precision errors were much smaller than observed differences between OA and normal density (~9x smaller), *in vivo* precision assessment was required to assess uncertainty associated with subject motion. *Ex vivo* and *in vivo* precision studies were also required to determine which depths offered repeatable density measures for predicting subchondral bone structural stiffness. The *in vivo* precision study represented a "worst case" scenario involving imaging moving living knees using a common, widely available clinical CT. Conversely, the *ex vivo* precision study represented a "best case" scenario involving imaging motionless cadaver knees with one of the fastest, most advanced clinical CT machines currently available. Since *in vivo* and *ex vivo* precision studies offered similar precision errors, CT-TOMASD has potential use both *in vivo* and *ex vivo* using nearly[§] every available clinical CT machine (e.g., 4, 16, 32, 64-slice CT).

A key accomplishment of Chapter 5 – Predicting Subchondral Bone Stiffness using CT-TOMASD was that we confirmed that CT-TOMASD can be used to predict, non-invasively, the structural stiffness of OA and normal proximal tibial subchondral bone. This is an important finding because we can now estimate subchondral bone stiffness in individuals living with OA to better understand the role of subchondral bone stiffness in OA initiation and progression. This research was required to test the structural stiffness of subchondral bone directly at the subchondral surface, which is most relevant to the OA disease process. Although bone density is generally regarded as being related to bone stiffness, this research was required to quantify the predictive ability of CT-TOMASD and establish whether or not OA affected stiffness-density predictions. Without this knowledge CT-

[§] Toshiba has recently released a 320-slice clinical CT machine.

TOMASD stiffness predictions would be unreliable given that previous research has shown dissimilar stiffness-density relationships for normal and OA trabecular bone from late-OA hips [49]. A second key accomplishment of Chapter 5 was that we found CT-TOMASD measures of density and stiffness to be related by a nonlinear power law function $E \propto BMD^{1.9}$. This is an important relationship because a small change in density would result in a large change in stiffness. This relationship could help explain the role of subchondral bone in OA more effectively than bone density alone.

6.2 Comparisons to Existing Findings

Comparisons between CT-TOMASD BMD measures and existing findings are difficult given that CT-TOMASD analyses of cadaveric and living proximal tibiae represent the only 3D measures of subchondral cortical and trabecular BMD located near the joint surface (< 5 mm). CT-TOMASD measures of proximal tibial epiphyseal density at distal sites (5-10 mm layer) are, however, comparable with existing measures using pQCT [28] and QCT [108] (Table 1-11).

CT-TOMASD analyses of normal and OA proximal tibial BMD revealed that medial subchondral BMD from OA knees was significantly higher than normal at sites near the subchondral bone surface (0-2.5, 2.5-5 mm layers). These results are in agreement with BMD studies using DXA [10, 12] (Table 1-9). These results do, however, disagree with one DXA study which found no medial compartment differences between OA and normal subchondral BMD at sites near the subchondral surface [22]. We believe these conflicting results may be due to the limitations of DXA and previously selected analysis regions containing subchondral cortical, subchondral trabecular and epiphyseal trabecular bone.

CT-TOMASD measures at the proximal tibia demonstrated *ex vivo* and *in vivo* precision errors < 5%. CT-TOMASD CV% precision errors were comparable with DXA measures of areal BMD (CV%:

1.4-7% [10-12, 24, 26]) and MRI measures of bone volume fraction (CV%: 3.4-4.0% [96, 98]). ICCs for CT-TOMASD measures were superior to pQCT measures of proximal tibial volumetric BMD [28].

CT-TOMASD predicted 67% of variance in subchondral structural stiffness measures at the proximal tibia, which is in agreement with previous findings [79, 84, 85, 88] (Table 1-12). The stiffness-density relationship between CT-TOMASD measures of density and stiffness was characterized by the nonlinear power law function $E = 0.004 \cdot BMD^{1.9}$. The exponent value of 1.9 is comparable with existing findings [79, 82, 83, 85, 89] (Table 1-12).

CT-TOMASD predictions of proximal tibial subchondral bone stiffness were not affected by the presence of overlying cartilage degeneration. This finding is in disagreement with previous research which has shown dissimilar stiffness-density relationships for normal and OA trabecular bone from late-OA hips [49]. However, the previous study assessed the stiffness of isolated bone samples obtained from sites distal to the subchondral surface, not overall structural stiffness. Our results demonstrate that OA does not affect stiffness-density relationships for predictions of overall structural stiffness.

Mean subchondral bone stiffness was 452 MPa, which is in agreement with stiffness measures of proximal tibial subchondral cortical bone (average E: 1150 MPa [188]) and subchondral trabecular bone (average E range: 131-610 MPa [50, 52-55]) (Tables 1-7 & 1-8). This is not surprising given that our structural stiffness test combines the stiffness properties of subchondral cortical and trabecular bone. The range of stiffness values (75–1140 MPa) was similar to observed values typically encountered during mechanical testing of proximal tibial bone [79, 82, 84-88, 110, 189] (Table 1-7). Our results are most comparable with studies of OA and normal subchondral trabecular bone using indentation (average E range: 178-397 MPa [55]) and compression testing (average E range: 131-610 MPa [50, 52-54]).

6.3 Strengths and Limitations

This thesis research has various strengths and limitations related to selected imaging methods, details of the mechanical indentation test, and study designs which require further explanation or have not yet been discussed.

A key strength of the CT-TOMASD technique is the ability to characterize the density of thin bony layers near the joint surface. Through use of small 3D voxel sizes and an optimum HMH threshold value, we were able to carefully define the location of the subchondral bone surface which permitted thin layer analyses. This is important because it is the bone located closest to the subchondral bone surface which has the greatest potential to negatively affect the overlying cartilage [19]. This is also important because the subchondral cortical, subchondral trabecular and epiphyseal trabecular bone regions may undergo distinct and different changes in density at different stages of OA progression [17, 28, 29]. Without the ability to image thin bone layers near the joint surface, OA-related density changes occurring across these regions may be missed. As CT technologies and spatial resolutions improve, CT-TOMASD could be used to characterize even smaller layers near the subchondral surface. A second strength of the CT-TOMASD technique is the ability to reconstruct the imaged tibia dataset in various orientations through use of 3D isotropic voxels. Using small voxel sizes, combined with digitized boundary points, the effects of patient positioning are minimized. Reliable comparisons of OA and normal subchondral bone density can therefore be made without concern that observed density differences are due to dissimilar image orientations. The use of small isotropic voxel sizes and digitized boundary points is also the primary reason why we observed small precision errors both *in vivo* and *ex vivo*. A third strength pertains to the use of adjusted depth measures for each subject, which enabled comparisons to be made between OA and healthy subjects without concern that observed density differences were simply due to different physical sizes (e.g., density across the 0-2.5 mm layer would be much higher in a large person than a small person due to thicker cortical bone).

A fourth strength pertains to CT-TOMASD regional analyses—particularly the 'focal spot' analysis—which detected alterations in BMD occurring with OA. It is unlikely that all cartilage and subchondral bone tissues will be equally affected by OA, therefore CT-TOMASD regional analyses may demonstrate significant proficiency at recognizing early signs of disease onset.

The key strength of our novel *in situ* indentation test is that we measured the stiffness of subchondral bone directly at the subchondral bone surface. This is important because it is this overall stiffness which will have the most influence on overlying cartilage integrity and relevance regarding the role of subchondral bone in OA initiation and progression. Bone response to loading during *in situ* indentation testing is also representative of the *in vivo* condition [119]. The mechanical properties of tissues distal to the subchondral surface may not accurately reflect the overall stiffness of subchondral bone, particularly if theories regarding "stress-shielding" effects [73] are true. A second strength was that we used fiducials for relating image density and bone stiffness. By carefully locating and registering the physical coordinate positions of fiducials found in the images and testing environment, we were able to relate the position of our indenter with imaged subchondral bone densities to within 1 voxel (0.5 mm) of the determined position. We were therefore able to relate subchondral bone stiffness with CT-TOMASD outcomes with confidence.

This research has limitations related to inherent limitations of imaged BMD, surface curvature, gender imbalance and OA categorizations. First, as previously stated, CT-TOMASD measures of apparent BMD reflect both the degree of mineralization (material density) and quantity of bone (bone volume fraction) present within the proximal tibia. Unfortunately, QCT cannot distinguish alterations in material density from alterations in bone volume fraction occurring with OA. This is an important limitation because material density and/or bone volume fraction of subchondral cortical, subchondral trabecular and epiphyseal trabecular bone may undergo specific alterations at different stages of OA progression [17, 28, 29]. It is possible that bone volume fraction increases while material density

decreases with OA (or vice versa), and the net effect would show no BMD changes. This is an inherent limitation of all current QCT technologies and spatial resolution does not alleviate this problem. Second, as previously discussed (Chapters 2), the 2D projection nature of CT-TOMASD can lead to overestimations of density near regions displaying large degrees of curvature. Due to the effects of curvature, the current technique is best suited for sites displaying minimal-to-moderate inclination such as the proximal tibia or patella. Application of CT-TOMASD layer analyses for sites exhibiting large curvature (e.g., distal or proximal femur) is possible, but requires CT-TOMASD to be modified to compute average density in relation to vectors oriented perpendicular (normal) to the curved subchondral bone surface (i.e., "surface normals"). This is a direction of ongoing research using techniques from a previously developed image registration algorithm [190]. Third, there was an imbalance between genders for both *ex vivo* and *in vivo* studies. Results from the *ex vivo* imaging research (Chapters 2, 3) primarily pertained to male subjects (8 male: 2 female). Likewise, results from the *ex vivo* indentation research (Chapter 5) strictly pertained to male subjects (10 male: 0 female). Subsequently, higher than normal BMD at sites nearest the subchondral bone surface (0-5 mm) and associations between BMD and stiffness may only pertain to male populations. Similarly, small *in vivo* precision errors may only be possible with female populations given that results from the *in vivo* imaging research (Chapter 4) primarily pertained to female subjects (3 male: 11 female). Therefore, caution must be taken when extrapolating study results to both sexes. Further research is required, using balanced male:female populations, to verify study findings. However, given that the *ex vivo* male-focused and *in vivo* female-focused precision studies offered comparable precision errors, we are confident that the CT-TOMASD technique will offer precise measures of subchondral bone density for both male and female populations. Fourth, OA categorizations using KL [57] and ICRS [58, 59] were performed by only one clinician (Dr. Bassam Masri). We did not assess the repeatability of Dr. Masri's classifications, and categorizations by other clinicians or radiologists and rheumatologists may have

offered different conclusions. Also, categorizations of varus-valgus alignment for cadaver knees without weight-bearing are questionable. However, Dr. Masri is a highly experienced orthopaedic surgeon who routinely performs KL gradings of OA knees and assessments of cartilage degeneration during joint replacement surgery.

6.4 Conclusions

1. The QCT-based CT-TOMASD imaging technique is capable of characterizing the patterns of density and thickness of subchondral bone for both healthy and OA proximal tibiae. CT-TOMASD provides 3D measures of subchondral density, which characterize both the amount of tissue and mineralization content present in bone, across thin layers near the subchondral surface thereby permitting separate analyses of subchondral cortical, subchondral trabecular and epiphyseal trabecular bone. This method is distinct from existing subchondral bone imaging tools which are largely limited to 2D analyses, individual bony regions (i.e., only epiphyseal or subchondral cortical bone), and an imaged dependence on correct patient positioning.
2. CT-TOMASD demonstrated *ex vivo* and *in vivo* precision errors many times smaller than observed density differences between OA and normal density (~9x smaller).
3. CT-TOMASD layer analyses demonstrated greater proficiency at distinguishing OA from normal subchondral bone density when compared alongside the existing CT-OAM maximum intensity imaging technique.
    a. CT-TOMASD demonstrated an average 17% greater whole medial compartment density in OA knees. CT-TOMASD focal region analyses revealed an average 24% greater density in the 0–2.5mm layer and 36% greater density in the 2.5–5 mm layer in OA knees.

b. CT-OAM demonstrated an average 17% greater whole medial compartment density in OA knees. CT-OAM did not distinguish focal density differences between OA and normal knees.

4. CT-TOMASD measures nearest the subchondral bone surface (0-2.5 mm depth) predicted, non-invasively, the structural stiffness of OA and normal proximal tibial subchondral bone (r^2 = 0.67).

6.5 Contributions

This thesis research has generated many 'firsts' (listed below) and has strong potential to move subchondral bone analysis from the 2D realm (i.e., DXA) to the 3D realm (i.e., QCT) and from the bench (i.e., histology using cadaver subjects) to the bedside (i.e., non-invasive measures using living subjects).

1. Developed the novel 3D imaging tool CT-TOMASD, which is the first non-invasive, clinically applicable technique to measure bone density separately in the distinct subchondral layers, including subchondral cortical, subchondral trabecular and epiphyseal trabecular bone.
2. First study to show the effect of OA on patterns of subchondral bone density in the proximal tibia.
3. First studies to show that widely available clinical QCT can be used to define proximal tibial subchondral bone density patterns, bone both *ex vivo* and *in vivo,* with precision errors many times smaller than observed density differences between OA and normal density (~9x smaller).
4. First study to show the depth dependence of OA-related bone changes. In particular, OA bone density nearest the subchondral surface (< 5 mm) was markedly higher than normal (+17-36%).

5. First study to show that OA-related bone changes were most pronounced across subchondral trabecular bone regions (2.5-5 mm layer).
6. First study to show that a layered surface projection approach is more effective than maximum intensity projections for distinguishing OA from normal density.
7. First study to assess the structural stiffness of proximal tibial subchondral bone directly at the subchondral surface.
8. First study to link structural stiffness properties with clinical QCT measures of BMD from proximal tibial subchondral bone.

6.6 Clinical Significance

There is no cure for OA and the exact cause is unknown. Current tools do not appear to detect the disease early enough for successful clinical intervention and OA is usually not detected until after significant cartilage damage. CT-TOMASD measures across different regions and depths may be associated with clinically relevant symptoms such as pain or disability. This could lead to earlier OA detection, which will improve treatment of this debilitating disease. For people living with OA, CT-TOMASD could be used to help monitor the success of treatments such as joint distraction, braces or bone-modifying drugs which try to delay OA progression. Combined with MRI or contrast-enhanced CT measures of cartilage biochemistry and morphology, CT-TOMASD could be used to determine whether bone changes occur prior to, simultaneously with, or secondary to articular cartilage degeneration. Simultaneous investigations of bone and cartilage properties could also be used to determine whether cartilage degeneration is spatially dependent upon the stiffness of underlying subchondral bone. This information could help better explain the role subchondral bone plays in the initiation and progression of OA.

6.7 Future Research

1) CT-TOMASD layer analyses will be performed on 60 individuals with clinical symptoms of early knee OA. CT-TOMASD layer analyses will be performed and linked with clinical measures, including age, body mass index (BMI), KL grading [57], individual radiographic features (osteophytes and JSN score from OARSI atlas [191]), pain using the Western Ontario and McMaster Universities Arthritis Index (WOMAC) [192], medication use and comorbidity. Identifying imaging features of OA associated with clinical diagnoses and symptoms could lead to earlier OA detection and improved treatment. This work is being conducted in collaboration with researchers from the New England Baptist Hospital (Hunter). To date, all 60 participants have undergone QCT scans of both knees using developed *in vivo* scanning parameters (Chapter 4). CT-TOMASD analyses of proximal tibial subchondral bone density are ongoing.

2) Finite element (FE) models (3D and 2D) of normal and OA knees will be developed using FE software (Abaqus, Abaqus Inc, Providence RI; ANSYS, ANSYS Inc, Houston, PA) and QCT scans from *ex vivo* and *in vivo* CT-TOMASD analyses. FE simulations will be used to determine whether OA-related alterations in subchondral bone thickness and material properties (predicted using stiffness-density relationships) change the overall structural stiffness of subchondral bone. This information will answer questions regarding whether or not subchondral bone stiffness increases (or decreases) with OA. FE models will also be used to estimate cartilage stresses developing as a result of altered subchondral bone properties and test hypotheses regarding the mechanical role of subchondral bone in the course of OA. QCT imaged density will be used to estimate the elastic modulus of proximal tibial bone (i.e., $E = BMD^2$). FE models will be validated using structural stiffness measures obtained from our macro indentation tests of healthy and OA knees. This work is currently being conducted in collaboration with researchers from the University of Western Ontario (Holdsworth, Milner) and

the University of Saskatchewan (Szyszkowski, Avari). To date, a 3D FE model of an OA proximal tibia has been developed using ABAQUS and a simplified 2D FE model of a generic knee is currently in development using ANSYS.

3) CT-TOMASD has been used to analyze subchondral bone properties in OA and normal patellae, but this work has only been presented as an abstract [193]. The results of this abstract, along with the *in vivo* precision of CT-TOMASD measures of patellar density, will be disseminated as a research article.

4) CT-TOMASD has potential for improving unicompartmental knee replacement (UKR) surgery by helping surgeons preoperatively define 'safe' resurfacing depths for UKR placement. Currently, some UKRs experience failure and instability, likely due to insufficient bony support at the proximal tibia. CT-TOMASD has been previously used to estimate the thickness of subchondral cortical and trabecular bone using simple thresholding [194]. Representatives from MAKO Surgical Corporation, a medical device company, have expressed interest in using this feature of CT-TOMASD to help surgeons improve surgical placement of their MAKOplasty UKR design. CT-TOMASD estimates of 'safe' resurfacing depths could help improve UKR stability and longevity.

5) We will use a modified version of CT-TOMASD to measure bone density patterns at the distal femur. The CT-TOMASD method will be modified using the previously discussed "surface normals" technique from a previously developed image registration algorithm [190]. This will permit CT-TOMASD analyses for distal femora using previously obtained QCT knee images from cadavers and living subjects.

6) Through addition of new regional analyses, we will attempt to identify early meniscal damage using CT-TOMASD. The meniscus may play a much larger role in OA initiation and development than previously hypothesized [195] and radiographically observed JSN may be

due to damaged menisci, not cartilage loss [195]. The CT-TOMASD method will be modified to measure the area of regions covered by the meniscus and central regions of each plateau using thresholding. These measures will be incorporated because many of the cadaver knees classified as OA had either degenerated or torn menisci. Qualitative analyses of CT-TOMASD images with damaged menisci suggested that density patterns differed from normal images, particularly along the peripheral, anterior and posterior regions typically covered by the meniscus. In these images the central region appeared larger than normal and the density of the medial posterior region appeared higher than normal. This information will help to design treatment methods that delay OA onset or progression.

7) We will use CT-TOMASD in combination with cartilage indentation tests to assess links between cartilage stiffness, bone stiffness and bone density. Our novel mechanical indentation test was used to test the stiffness of overlying cartilage using the classic analysis by Hayes [196]. This research will provide valuable information regarding associations between cartilage and bone.

BIBLIOGRAPHY

1. Health Canada. Arthritis in Canada: An Ongoing Challenge. 2003.
2. Radin EL, Paul IL, Rose RM. Role of mechanical factors in pathogenesis of primary osteoarthritis. Lancet. 1972; 1(7749):519-522.
3. Radin EL, Parker HG, Pugh JW, Steinberg RS, Paul IL, Rose RM. Response of joints to impact loading. 3. Relationship between trabecular microfractures and cartilage degeneration. J Biomech. 1973; 6(1):51-57.
4. Radin EL, Rose RM. Role of subchondral bone in the initiation and progression of cartilage damage. Clin Orthop Relat Res. 1986(213):34-40.
5. Hochberg MC, Lethbridge-Cejku M, Tobin JD. Bone mineral density and osteoarthritis: data from the Baltimore Longitudinal Study of Aging. Osteoarthritis Cartilage. 2004; 12 Suppl A:S45-48.
6. Belmonte-Serrano MA, Bloch DA, Lane NE, Michel BE, Fries JF. The relationship between spinal and peripheral osteoarthritis and bone density measurements. J Rheumatol. 1993; 20(6):1005-1013.
7. Sowers M, Lachance L, Jamadar D, Hochberg MC, Hollis B, Crutchfield M, et al. The associations of bone mineral density and bone turnover markers with osteoarthritis of the hand and knee in pre- and perimenopausal women. Arthritis Rheum. 1999; 42(3):483-489.
8. Hart DJ, Cronin C, Daniels M, Worthy T, Doyle DV, Spector TD. The relationship of bone density and fracture to incident and progressive radiographic osteoarthritis of the knee: the Chingford Study. Arthritis Rheum. 2002; 46(1):92-99.
9. Lethbridge-Cejku M, Tobin JD, Scott WW, Jr., Reichle R, Roy TA, Plato CC, et al. Axial and hip bone mineral density and radiographic changes of osteoarthritis of the knee: data from the Baltimore Longitudinal Study of Aging. J Rheumatol. 1996; 23(11):1943-1947.
10. Bruyere O, Dardenne C, Lejeune E, Zegels B, Pahaut A, Richy F, et al. Subchondral tibial bone mineral density predicts future joint space narrowing at the medial femoro-tibial compartment in patients with knee osteoarthritis. Bone. 2003; 32(5):541-545.
11. Clarke S, Wakeley C, Duddy J, Sharif M, Watt I, Ellingham K, et al. Dual-energy X-ray absorptiometry applied to the assessment of tibial subchondral bone mineral density in osteoarthritis of the knee. Skeletal Radiol. 2004; 33(10):588-595.
12. Madsen OR, Schaadt O, Bliddal H, Egsmose C, Sylvest J. Bone mineral distribution of the proximal tibia in gonarthrosis assessed in vivo by photon absorption. Osteoarthritis Cartilage. 1994; 2(2):141-147.
13. Lajeunesse D, Reboul P. Subchondral bone in osteoarthritis: a biologic link with articular cartilage leading to abnormal remodeling. Curr Opin Rheumatol. 2003; 15(5):628-633.
14. Bobinac D, Spanjol J, Zoricic S, Maric I. Changes in articular cartilage and subchondral bone histomorphometry in osteoarthritic knee joints in humans. Bone. 2003; 32(3):284-290.
15. Matsui H, Shimizu M, Tsuji H. Cartilage and subchondral bone interaction in osteoarthrosis of human knee joint: a histological and histomorphometric study. Microsc Res Tech. 1997; 37(4):333-342.

16. Yamada K, Healey R, Amiel D, Lotz M, Coutts R. Subchondral bone of the human knee joint in aging and osteoarthritis. Osteoarthritis Cartilage. 2002; 10(5):360-369.

17. Burr DB, Schaffler MB. The involvement of subchondral mineralized tissues in osteoarthrosis: quantitative microscopic evidence. Microsc Res Tech. 1997; 37(4):343-357.

18. Burr DB. The importance of subchondral bone in osteoarthrosis. Curr Opin Rheumatol. 1998; 10(3):256-262.

19. Brown TD, Radin EL, Martin RB, Burr DB. Finite element studies of some juxtarticular stress changes due to localized subchondral stiffening. J Biomech. 1984; 17(1):11-24.

20. Radin EL. Mechanical aspects of osteoarthrosis. Bull Rheum Dis. 1976; 26(7):862-865.

21. Lo GH, Zhang Y, McLennan C, Niu J, Kiel DP, McLean RR, et al. The ratio of medial to lateral tibial plateau bone mineral density and compartment-specific tibiofemoral osteoarthritis. Osteoarthritis Cartilage. 2006; 14(10):984-990.

22. Karvonen RL, Miller PR, Nelson DA, Granda JL, Fernandez-Madrid F. Periarticular osteoporosis in osteoarthritis of the knee. J Rheumatol. 1998; 25(11):2187-2194.

23. Clark JM, Huber JD. The structure of the human subchondral plate. J Bone Joint Surg Br. 1990; 72(5):866-873.

24. Wada M, Maezawa Y, Baba H, Shimada S, Sasaki S, Nose Y. Relationships among bone mineral densities, static alignment and dynamic load in patients with medial compartment knee osteoarthritis. Rheumatology (Oxford). 2001; 40(5):499-505.

25. Thorp LE, Wimmer MA, Block JA, Moisio KC, Shott S, Goker B, et al. Bone mineral density in the proximal tibia varies as a function of static alignment and knee adduction angular momentum in individuals with medial knee osteoarthritis. Bone. 2006; 39(5):1116-1122.

26. Hulet C, Sabatier JP, Souquet D, Locker B, Marcelli C, Vielpeau C. Distribution of bone mineral density at the proximal tibia in knee osteoarthritis. Calcif Tissue Int. 2002; 71(4):315-322.

27. Messent EA, Buckland-Wright JC, Blake GM. Fractal analysis of trabecular bone in knee osteoarthritis (OA) is a more sensitive marker of disease status than bone mineral density (BMD). Calcif Tissue Int. 2005; 76(6):419-425.

28. Bennell KL, Creaby MW, Wrigley TV, Hunter DJ. Tibial subchondral trabecular volumetric bone density in medial knee joint osteoarthritis using peripheral quantitative computed tomography technology. Arthritis Rheum. 2008; 58(9):2776-2785.

29. Burr DB. Anatomy and physiology of the mineralized tissues: role in the pathogenesis of osteoarthrosis. Osteoarthritis Cartilage. 2004; 12 Suppl A:S20-30.

30. Engelke K, Libanati C, Liu Y, Wang H, Austin M, Fuerst T, et al. Quantitative computed tomography (QCT) of the forearm using general purpose spiral whole-body CT scanners: accuracy, precision and comparison with dual-energy X-ray absorptiometry (DXA). Bone. 2009; 45(1):110-118.

31. Genant HK, Engelke K, Prevrhal S. Advanced CT bone imaging in osteoporosis. Rheumatology (Oxford). 2008; 47 Suppl 4:iv9-16.

32. Schipplein OD, Andriacchi TP. Interaction between active and passive knee stabilizers during level walking. J Orthop Res. 1991; 9(1):113-119.

33. Williams PL, Warwick R, Dyson M, Bannister LH. Gray's Anatomy. 37 ed. London: Churchill Livingstone, 1989.

34. Seedhom BB, Dowson D, Wright V. Proceedings: Functions of the menisci. A preliminary study. Ann Rheum Dis. 1974; 33(1):111.

35. Kurosawa H, Fukubayashi T, Nakajima H. Load-bearing mode of the knee joint: physical behavior of the knee joint with or without menisci. Clin Orthop Relat Res. 1980(149):283-290.

36. Walker PS, Erkman MJ. The role of the menisci in force transmission across the knee. Clin Orthop Relat Res. 1975(109):184-192.

37. Fukubayashi T, Kurosawa H. The contact area and pressure distribution pattern of the knee. A study of normal and osteoarthrotic knee joints. Acta Orthop Scand. 1980; 51(6):871-879.

38. Schreppers GJ, Sauren AA, Huson A. A numerical model of the load transmission in the tibio-femoral contact area. Proc Inst Mech Eng H. 1990; 204(1):53-59.

39. Sauren AA, Huson A, Schouten RY. An Axisymmetric Finite Element Analysis of the Mechanical Function of the Meniscus. Int J Sports Med. 1984; 5:3.

40. Ahmed AM, Burke DL. In-vitro measurement of static pressure distribution in synovial joints--Part I: Tibial surface of the knee. J Biomech Eng. 1983; 105(3):216-225.

41. Dewire P, Einhorm T. The Joint as an Organ. In: Moskowitz R, Howell D, Altman R, Buckwalter J, Goldberg V, eds. Osteoarthritis: Diagnosis and Medical/Surgical Management: W.B. Saunders; 2001.

42. Mow VC, Gu WY, Chen FH. Structure and function of articular cartilage and meniscus. In: Mow VC, Huiskes R, eds. Basic Orthopaedic Biomechanics and Mechano-Biology. Third ed. Philadelphia: Lippincott Williams and Wilkins; 2005:182-258.

43. Imhof H, Breitenseher M, Kainberger F, Rand T, Trattnig S. Importance of subchondral bone to articular cartilage in health and disease. Top Magn Reson Imaging. 1999; 10(3):180-192.

44. Radin EL, Paul IL. Importance of bone in sparing articular cartilage from impact. Clin Orthop Relat Res. 1971; 78:342-344.

45. Madry H, van Dijk CN, Mueller-Gerbl M. The basic science of the subchondral bone. Knee Surg Sports Traumatol Arthrosc. 2010; 18(4):419-433.

46. Brandt KD, Dieppe P, Radin EL. Etiopathogenesis of osteoarthritis. Rheum Dis Clin North Am. 2008; 34(3):531-559.

47. Brandt KD, Mankin HJ, Shulman LE. Workshop on etiopathogenesis of osteoarthritis. J Rheumatol. 1986; 13:35.

48. Li B, Aspden RM. Mechanical and material properties of the subchondral bone plate from the femoral head of patients with osteoarthritis or osteoporosis. Ann Rheum Dis. 1997; 56(4):247-254.

49. Li B, Aspden RM. Composition and mechanical properties of cancellous bone from the femoral head of patients with osteoporosis or osteoarthritis. J Bone Miner Res. 1997; 12(4):641-651.

50. Zysset PK, Sonny M, Hayes WC. Morphology-mechanical property relations in trabecular bone of the osteoarthritic proximal tibia. J Arthroplasty. 1994; 9(2):203-216.

51. Lereim P, Goldie I, Dahlberg E. Hardness of the subchondral bone of the tibial condyles in the normal state and in osteoarthritis and rheumatoid arthritis. Acta Orthop Scand. 1974; 45(4):614-627.

52. Day JS, Ding M, van der Linden JC, Hvid I, Sumner DR, Weinans H. A decreased subchondral trabecular bone tissue elastic modulus is associated with pre-arthritic cartilage damage. J Orthop Res. 2001; 19(5):914-918.

53. Ding M, Dalstra M, Linde F, Hvid I. Changes in the stiffness of the human tibial cartilage-bone complex in early-stage osteoarthrosis. Acta Orthop Scand. 1998; 69(4):358-362.

54. Ding M, Danielsen CC, Hvid I. Bone density does not reflect mechanical properties in early-stage arthrosis. Acta Orthop Scand. 2001; 72(2):181-185.

55. Finlay JB, Bourne RB, Kraemer WJ, Moroz TK, Rorabeck CH. Stiffness of bone underlying the tibial plateaus of osteoarthritic and normal knees. Clin Orthop Relat Res. 1989(247):193-201.

56. Felson DT. Clinical practice. Osteoarthritis of the knee. N Engl J Med. 2006; 354(8):841-848.

57. Kellgren JH, Lawrence JS. Radiological assessment of osteo-arthrosis. Ann Rheum Dis. 1957; 16(4):494-502.

58. Mainil-Varlet P, Aigner T, Brittberg M, Bullough P, Hollander A, Hunziker E, et al. Histological assessment of cartilage repair: a report by the Histology Endpoint Committee of the International Cartilage Repair Society (ICRS). J Bone Joint Surg Am. 2003; 85-A Suppl 2:45-57.

59. Outerbridge RE. The etiology of chondromalacia patellae. J Bone Joint Surg Br. 1961; 43-B:752-757.

60. Kleemann RU, Krocker D, Cedraro A, Tuischer J, Duda GN. Altered cartilage mechanics and histology in knee osteoarthritis: relation to clinical assessment (ICRS Grade). Osteoarthritis Cartilage. 2005; 13(11):958-963.

61. Mankin HJ, Dorfman H, Lippiello L, Zarins A. Biochemical and metabolic abnormalities in articular cartilage from osteo-arthritic human hips. II. Correlation of morphology with biochemical and metabolic data. J Bone Joint Surg Am. 1971; 53(3):523-537.

62. Felson DT, Lawrence RC, Dieppe PA, Hirsch R, Helmick CG, Jordan JM, et al. Osteoarthritis: new insights. Part 1: the disease and its risk factors. Ann Intern Med. 2000; 133(8):635-646.

63. Dequeker J. Inverse relationship of interface between osteoporosis and osteoarthritis. J Rheumatol. 1997; 24(4):795-798.

64. Aigner T, McKenna L. Molecular pathology and pathobiology of osteoarthritic cartilage. Cell Mol Life Sci. 2002; 59(1):5-18.

65. Blanco FJ, Guitian R, Vazquez-Martul E, de Toro FJ, Galdo F. Osteoarthritis chondrocytes die by apoptosis. A possible pathway for osteoarthritis pathology. Arthritis Rheum. 1998; 41(2):284-289.

66. Newberry WN, Zukosky DK, Haut RC. Subfracture insult to a knee joint causes alterations in the bone and in the functional stiffness of overlying cartilage. J Orthop Res. 1997; 15(3):450-455.

67. Radin EL, Paul IL, Tolkoff MJ. Subchondral bone changes in patients with early degenerative joint disease. Arthritis Rheum. 1970; 13(4):400-405.

68. Burr DB, Radin EL. Microfractures and microcracks in subchondral bone: are they relevant to osteoarthrosis? Rheum Dis Clin North Am. 2003; 29(4):675-685.

69. Bailey AJ, Mansell JP. Do subchondral bone changes exacerbate or precede articular cartilage destruction in osteoarthritis of the elderly? Gerontology. 1997; 43(5):296-304.

70. Bailey AJ, Mansell JP, Sims TJ, Banse X. Biochemical and mechanical properties of subchondral bone in osteoarthritis. Biorheology. 2004; 41(3-4):349-358.

71. Mansell JP, Bailey AJ. Abnormal cancellous bone collagen metabolism in osteoarthritis. J Clin Invest. 1998; 101(8):1596-1603.

72. Milz S, Putz R. Quantitative morphology of the subchondral plate of the tibial plateau. J Anat. 1994; 185 (Pt 1):103-110.

73. Buckland-Wright C. Subchondral bone changes in hand and knee osteoarthritis detected by radiography. Osteoarthritis Cartilage. 2004; 12 Suppl A:S10-19.

74. Grynpas MD, Alpert B, Katz I, Lieberman I, Pritzker KP. Subchondral bone in osteoarthritis. Calcif Tissue Int. 1991; 49(1):20-26.

75. Kamibayashi L, Wyss UP, Cooke TD, Zee B. Trabecular microstructure in the medial condyle of the proximal tibia of patients with knee osteoarthritis. Bone. 1995; 17(1):27-35.

76. Chappard C, Peyrin F, Bonnassie A, Lemineur G, Brunet-Imbault B, Lespessailles E, et al. Subchondral bone micro-architectural alterations in osteoarthritis: a synchrotron micro-computed tomography study. Osteoarthritis Cartilage. 2006; 14(3):215-223.

77. Fazzalari NL, Parkinson IH. Fractal properties of subchondral cancellous bone in severe osteoarthritis of the hip. J Bone Miner Res. 1997; 12(4):632-640.

78. Brown SJ, Pollintine P, Powell DE, Davie MW, Sharp CA. Regional differences in mechanical and material properties of femoral head cancellous bone in health and osteoarthritis. Calcif Tissue Int. 2002; 71(3):227-234.

79. Linde F, Hvid I, Madsen F. The effect of specimen geometry on the mechanical behaviour of trabecular bone specimens. J Biomech. 1992; 25(4):359-368.

80. Carter DR, Hayes WC. The compressive behavior of bone as a two-phase porous structure. J Bone Joint Surg Am. 1977; 59(7):954-962.

81. Ashman RB, Rho JY, Turner CH. Anatomical variation of orthotropic elastic moduli of the proximal human tibia. J Biomech. 1989; 22(8-9):895-900.

82. Anderson MJ, Keyak JH, Skinner HB. Compressive mechanical properties of human cancellous bone after gamma irradiation. J Bone Joint Surg Am. 1992; 74(5):747-752.

83. Keyak JH, Lee IY, Skinner HB. Correlations between orthogonal mechanical properties and density of trabecular bone: use of different densitometric measures. J Biomed Mater Res. 1994; 28(11):1329-1336.

84. Hvid I, Bentzen SM, Linde F, Mosekilde L, Pongsoipetch B. X-ray quantitative computed tomography: the relations to physical properties of proximal tibial trabecular bone specimens. J Biomech. 1989; 22(8-9):837-844.

85. Odgaard A, Linde F. The underestimation of Young's modulus in compressive testing of cancellous bone specimens. J Biomech. 1991; 24(8):691-698.

86. Linde F, Pongsoipetch B, Frich LH, Hvid I. Three-axial strain controlled testing applied to bone specimens from the proximal tibial epiphysis. J Biomech. 1990; 23(11):1167-1172.

87. Linde F, Hvid I. The effect of constraint on the mechanical behaviour of trabecular bone specimens. J Biomech. 1989; 22(5):485-490.

88. Linde F, Norgaard P, Hvid I, Odgaard A, Soballe K. Mechanical properties of trabecular bone. Dependency on strain rate. J Biomech. 1991; 24(9):803-809.

89. Morgan EF, Bayraktar HH, Keaveny TM. Trabecular bone modulus-density relationships depend on anatomic site. J Biomech. 2003; 36(7):897-904.

90. Harada Y, Wevers HW, Cooke TD. Distribution of bone strength in the proximal tibia. J Arthroplasty. 1988; 3(2):167-175.

91. Hvid I, Hansen SL. Subchondral bone strength in arthrosis. Cadaver studies of tibial condyles. Acta Orthop Scand. 1986; 57(1):47-51.

92. Hvid I. Trabecular bone strength at the knee. Clin Orthop Relat Res. 1988; 227:210-221.

93. Messent EA, Ward RJ, Tonkin CJ, Buckland-Wright C. Cancellous bone differences between knees with early, definite and advanced joint space loss; a comparative quantitative macroradiographic study. Osteoarthritis Cartilage. 2005; 13(1):39-47.

94. Messent EA, Ward RJ, Tonkin CJ, Buckland-Wright C. Differences in trabecular structure between knees with and without osteoarthritis quantified by macro and standard radiography, respectively. Osteoarthritis Cartilage. 2006; 14(12):1302-1305.

95. Messent EA, Ward RJ, Tonkin CJ, Buckland-Wright C. Tibial cancellous bone changes in patients with knee osteoarthritis. A short-term longitudinal study using Fractal Signature Analysis. Osteoarthritis Cartilage. 2005; 13(6):463-470.

96. Bolbos RI, Zuo J, Banerjee S, Link TM, Ma CB, Li X, et al. Relationship between trabecular bone structure and articular cartilage morphology and relaxation times in early OA of the knee joint using parallel MRI at 3 T. Osteoarthritis Cartilage. 2008; 16(10):1150-1159.

97. Lindsey CT, Narasimhan A, Adolfo JM, Jin H, Steinbach LS, Link T, et al. Magnetic resonance evaluation of the interrelationship between articular cartilage and trabecular bone of the osteoarthritic knee. Osteoarthritis Cartilage. 2004; 12(2):86-96.

98. Beuf O, Ghosh S, Newitt DC, Link TM, Steinbach L, Ries M, et al. Magnetic resonance imaging of normal and osteoarthritic trabecular bone structure in the human knee. Arthritis Rheum. 2002; 46(2):385-393.

99. Blumenkrantz G, Lindsey CT, Dunn TC, Jin H, Ries MD, Link TM, et al. A pilot, two-year longitudinal study of the interrelationship between trabecular bone and articular cartilage in the osteoarthritic knee. Osteoarthritis Cartilage. 2004; 12(12):997-1005.

100. Wolff J. Das Gesetz der Transformation der Knochen. Berlin, 1892.

101. Bauer JS, Link TM. Advances in osteoporosis imaging. Eur J Radiol. 2009; 71(3):440-449.

102. MacKay A. Personal communication. 2007.

103. Henckel J, Richards R, Lozhkin K, Harris S, Baena FM, Barrett AR, et al. Very low-dose computed tomography for planning and outcome measurement in knee replacement. The imperial knee protocol. J Bone Joint Surg Br. 2006; 88(11):1513-1518.

104. UNSCEAR 2000 Report to the General Assembly - Volume 1. Sources and Effects of Ionizing Radiation: United Nations Scientific Committee on the Effects of Atomic Radiation 2000.

105. UNSCEAR 2000 Report to the General Assembly - Annex B: Exposures from natural radiation sources Sources and Effects of Ionizing Radiation: United Nations Scientific Committee on the Effects of Atomic Radiation 2000.

106. Hart D, Hillier MC, Wall BF, Shrimpton PC, Bungay D. Doses to patients from medical x-ray examinations in the UK: 1995 review - NRPB-R289. London: HMSO 1994.

107. Wall BF, Hart D. Revised radiation doses for typical X-ray examinations. Report on a recent review of doses to patients from medical X-ray examinations in the UK by NRPB. National Radiological Protection Board. Br J Radiol. 1997; 70(833):437-439.

108. Khodadadyan-Klostermann C, von Seebach M, Taylor WR, Duda GN, Haas NP. Distribution of bone mineral density with age and gender in the proximal tibia. Clin Biomech (Bristol, Avon). 2004; 19(4):370-376.

109. Odgaard A, Pedersen CM, Bentzen SM, Jorgensen J, Hvid I. Density changes at the proximal tibia after medial meniscectomy. J Orthop Res. 1989; 7(5):744-753.

110. Bentzen SM, Hvid I, Jorgensen J. Mechanical strength of tibial trabecular bone evaluated by X-ray computed tomography. J Biomech. 1987; 20(8):743-752.

111. Müller-Gerbl M. The subchondral bone plate. Adv Anat Embryol Cell Biol. 1998; 141:III-XI, 1-134.

112. Anetzberger H, Schulz C, Pfahler M, Refior HJ, Muller-Gerbl M. Subchondral mineralization patterns of the glenoid after tear of the supraspinatus. Clin Orthop Relat Res. 2002(404):263-268.

113. Müller-Gerbl M, Putz R, Hodapp N, Schulte E, Wimmer B. Computed tomography-osteoabsorptiometry for assessing the density distribution of subchondral bone as a measure of long-term mechanical adaptation in individual joints. Skeletal Radiol. 1989; 18(7):507-512.

114. Müller-Gerbl M, Putz R, Kenn R. Demonstration of subchondral bone density patterns by three-dimensional CT osteoabsorptiometry as a noninvasive method for in vivo assessment of individual long-term stresses in joints. J Bone Miner Res. 1992; 7 Suppl 2:S411-418.

115. Eckstein F, Muller-Gerbl M, Putz R. Distribution of subchondral bone density and cartilage thickness in the human patella. J Anat. 1992; 180 (Pt 3):425-433.

116. Muhlhofer H, Ercan Y, Drews S, Matsuura M, Meissner J, Linsenmaier U, et al. Mineralisation and mechanical strength of the subchondral bone plate of the inferior tibial facies. Surg Radiol Anat. 2009; 31(4):237-243.

117. Eckstein F, Putz R, Muller-Gerbl M, Steinlechner M, Benedetto KP. Cartilage degeneration in the human patellae and its relationship to the mineralisation of the underlying bone: a key to the understanding of chondromalacia patellae and femoropatellar arthrosis? Surg Radiol Anat. 1993; 15(4):279-286.

118. Prokop M, Shin HO, Schanz A, Schaefer-Prokop CM. Use of maximum intensity projections in CT angiography: a basic review. Radiographics. 1997; 17(2):433-451.

119. McKoy BE, Kang Q, An YH. Indentation Testing of Bone In: An YH, Draughn RA, eds. Mechanical Testing of Bone and the Bone-Implant Interface. Boca Raton: CRC Press; 2000:233-256.

120. Little RB, Wevers HW, Siu D, Cooke TD. A three-dimensional finite element analysis of the upper tibia. J Biomech Eng. 1986; 108(2):111-119.

121. Yang JP, Bogoch ER, Woodside TD, Hearn TC. Stiffness of trabecular bone of the tibial plateau in patients with rheumatoid arthritis of the knee. J Arthroplasty. 1997; 12(7):798-803.

122. Aitken GK, Bourne RB, Finlay JB, Rorabeck CH, Andreae PR. Indentation stiffness of the cancellous bone in the distal human tibia. Clin Orthop Relat Res. 1985(201):264-270.

123. Katoh T, Griffin MP, Wevers HW, Rudan J. Bone hardness testing in the trabecular bone of the human patella. J Arthroplasty. 1996; 11(4):460-468.

124. Josechak RG, Finlay JB, Bourne RB, Rorabeck CH. Cancellous bone support for patellar resurfacing. Clin Orthop Relat Res. 1987(220):192-199.

125. Nakabayashi Y, Wevers HW, Cooke TD, Griffin M. Bone strength and histomorphometry of the distal femur. J Arthroplasty. 1994; 9(3):307-315.

126. Gordon KD, Duck TR, King GJ, Johnson JA. Mechanical properties of subchondral cancellous bone of the radial head. J Orthop Trauma. 2003; 17(4):285-289.

127. Anglin C, Tolhurst P, Wyss UP, Pichora DR. Glenoid cancellous bone strength and modulus. J Biomech. 1999; 32(10):1091-1097.

128. Mimar R, Limb D, Hall RM. Evaluation of the mechanical and architectural properties of glenoid bone. J Shoulder Elbow Surg. 2008; 17(2):336-341.

129. Timoskenko SP, Goodier JN. Theory of Elasticity. 3rd ed. New York: McGraw-Hill, 1970.

130. Burr DB. The importance of subchondral bone in the progression of osteoarthritis. J Rheumatol Suppl. 2004; 70:77-80.

131. Kontulainen S, Liu D, Manske S, Jamieson M, Sievanen H, McKay H. Analyzing cortical bone cross-sectional geometry by peripheral QCT: comparison with bone histomorphometry. J Clin Densitom. 2007; 10(1):86-92.

132. Spoor CF, Zonneveld FW, Macho GA. Linear measurements of cortical bone and dental enamel by computed tomography: applications and problems. Am J Phys Anthropol. 1993; 91(4):469-484.

133. Glüer CC, Blake G, Lu Y, Blunt BA, Jergas M, Genant HK. Accurate assessment of precision errors: how to measure the reproducibility of bone densitometry techniques. Osteoporos Int. 1995; 5(4):262-270.

134. Cohen J. Statistical Power Analysis for the Behavioral Sciences. 2nd ed. Hillsdale, NJ: Erlbaum, 1988.

135. Wolf FM. Meta-analysis: Quantitative Methods for Research Synthesis. Newbury, London: Sage, 1986.

136. Buckland-Wright JC, Lynch JA, Macfarlane DG. Fractal signature analysis measures cancellous bone organisation in macroradiographs of patients with knee osteoarthritis. Ann Rheum Dis. 1996; 55(10):749-755.

137. Boyd SK, Matyas JR, Wohl GR, Kantzas A, Zernicke RF. Early regional adaptation of periarticular bone mineral density after anterior cruciate ligament injury. J Appl Physiol. 2000; 89(6):2359-2364.

138. Dedrick DK, Goldstein SA, Brandt KD, O'Connor BL, Goulet RW, Albrecht M. A longitudinal study of subchondral plate and trabecular bone in cruciate-deficient dogs with osteoarthritis followed up for 54 months. Arthritis Rheum. 1993; 36(10):1460-1467.

139. Young BD, Samii VF, Mattoon JS, Weisbrode SE, Bertone AL. Subchondral bone density and cartilage degeneration patterns in osteoarthritic metacarpal condyles of horses. Am J Vet Res. 2007; 68(8):841-849.

140. Samii VF, Les Clifford M, Schulz KS, Keyak JH, Stover SM. Computed tomographic osteoabsorptiometry of the elbow joint in clinically normal dogs. Am J Vet Res. 2002; 63(8):1159-1166.

141. Drum MG, Les CM, Park RD, Norrdin RW, McIlwraith CW, Kawcak CE. Correlation of quantitative computed tomographic subchondral bone density and ash density in horses. Bone. 2009; 44(2):316-319.

142. Meirer R, Muller-Gerbl M, Huemer GM, Schirmer M, Herold M, Kersting S, et al. Quantitative assessment of periarticular osteopenia in patients with early rheumatoid arthritis: a preliminary report. Scand J Rheumatol. 2004; 33(5):307-311.

143. Laval-Jeantet AM, Roger B, Bouysee S, Bergot C, Mazess RB. Influence of vertebral fat content on quantitative CT density. Radiology. 1986; 159(2):463-466.

144. Glüer CC, Reiser UJ, Davis CA, Rutt BK, Genant HK. Vertebral mineral determination by quantitative computed tomography (QCT): accuracy of single and dual energy measurements. J Comput Assist Tomogr. 1988; 12(2):242-258.

145. Guglielmi G, Lang TF. Quantitative computed tomography. Semin Musculoskelet Radiol. 2002; 6(3):219-227.

146. Reinbold WD, Adler CP, Kalender WA, Lente R. Accuracy of vertebral mineral determination by dual-energy quantitative computed tomography. Skeletal Radiol. 1991; 20(1):25-29.

147. Cann CE, Genant HK. Precise measurement of vertebral mineral content using computed tomography. J Comput Assist Tomogr. 1980; 4(4):493-500.

148. Cann CE. Quantitative CT for determination of bone mineral density: a review. Radiology. 1988; 166(2):509-522.

149. Ciarelli MJ, Goldstein SA, Kuhn JL, Cody DD, Brown MB. Evaluation of orthogonal mechanical properties and density of human trabecular bone from the major metaphyseal regions with materials testing and computed tomography. J Orthop Res. 1991; 9(5):674-682.

150. Hayes WC, Piazza SJ, Zysset PK. Biomechanics of fracture risk prediction of the hip and spine by quantitative computed tomography. Radiol Clin North Am. 1991; 29(1):1-18.

151. Takada M, Engelke K, Hagiwara S, Grampp S, Genant HK. Accuracy and precision study in vitro for peripheral quantitative computed tomography. Osteoporos Int. 1996; 6(3):207-212.

152. Kaneko TS, Bell JS, Pejcic MR, Tehranzadeh J, Keyak JH. Mechanical properties, density and quantitative CT scan data of trabecular bone with and without metastases. J Biomech. 2004; 37(4):523-530.

153. Schneider S, Breit SM, Grampp S, Kunzel WW, Liesegang A, Mayrhofer E, et al. Comparative assessment of bone mineral measurements obtained by use of dual-energy x-ray absorptiometry, peripheral quantitative computed tomography, and chemical-physical analyses in femurs of juvenile and adult dogs. Am J Vet Res. 2004; 65(7):891-900.

154. Hangartner TN, Gilsanz V. Evaluation of cortical bone by computed tomography. J Bone Miner Res. 1996; 11(10):1518-1525.

155. Prevrhal S, Engelke K, Kalender WA. Accuracy limits for the determination of cortical width and density: the influence of object size and CT imaging parameters. Phys Med Biol. 1999; 44(3):751-764.

156. Newman DL, Dougherty G, al Obaid A, al Hajrasy H. Limitations of clinical CT in assessing cortical thickness and density. Phys Med Biol. 1998; 43(3):619-626.

157. Johnston JD, Masri BA, Wilson DR. Computed Tomography Topographic Mapping of Subchondral Density (CT-TOMASD) in osteoarthritic and normal knees: Methodological development and preliminary findings. Osteoarthritis and Cartilage. 2009; 17:1319-1326.

158. Einhorn TA. Bone strength: the bottom line. Calcif Tissue Int. 1992; 51(5):333-339.

159. Gong JK, Burgess E, Bacalao P. Accretion and exchange of strontium-85 in trabecular and cortical bones. Radiat Res. 1966; 28(4):753-765.

160. Brandt KD, Myers SL, Burr D, Albrecht M. Osteoarthritic changes in canine articular cartilage, subchondral bone, and synovium fifty-four months after transection of the anterior cruciate ligament. Arthritis Rheum. 1991; 34(12):1560-1570.

161. Silvast TS, Jurvelin JS, Lammi MJ, Toyras J. pQCT study on diffusion and equilibrium distribution of iodinated anionic contrast agent in human articular cartilage - associations to matrix composition and integrity. Osteoarthritis Cartilage. 2008.

162. Piscaer TM, van Osch GJ, Verhaar JA, Weinans H. Imaging of experimental osteoarthritis in small animal models. Biorheology. 2008; 45(3-4):355-364.

163. Taylor C, Carballido-Gamio J, Majumdar S, Li X. Comparison of quantitative imaging of cartilage for osteoarthritis: T2, T1rho, dGEMRIC and contrast-enhanced computed tomography. Magn Reson Imaging. 2009; 27(6):779-784.

164. Aula AS, Jurvelin JS, Toyras J. Simultaneous computed tomography of articular cartilage and subchondral bone. Osteoarthritis Cartilage. 2009.

165. Croft P, Cooper C, Wickham C, Coggon D. Defining osteoarthritis of the hip for epidemiologic studies. Am J Epidemiol. 1990; 132(3):514-522.

166. Spector TD, Hart DJ, Byrne J, Harris PA, Dacre JE, Doyle DV. Definition of osteoarthritis of the knee for epidemiological studies. Ann Rheum Dis. 1993; 52(11):790-794.

167. Hvid I, Hansen SL. Trabecular bone strength patterns at the proximal tibial epiphysis. J Orthop Res. 1985; 3(4):464-472.

168. Frobell RB, Nevitt MC, Hudelmaier M, Wirth W, Wyman BT, Benichou O, et al. Femorotibial subchondral bone area and regional cartilage thickness - a cross-sectional description in healthy reference cases and various radiographic stages of osteoarthritis in 1003 knees from the Osteoarthritis Initiative. Arthritis Care Res (Hoboken). 2010.

169. Jones G, Ding C, Scott F, Glisson M, Cicuttini F. Early radiographic osteoarthritis is associated with substantial changes in cartilage volume and tibial bone surface area in both males and females. Osteoarthritis Cartilage. 2004; 12(2):169-174.

170. Hellio Le Graverand MP, Buck RJ, Wyman BT, Vignon E, Mazzuca SA, Brandt KD, et al. Subregional femorotibial cartilage morphology in women--comparison between healthy controls and participants with different grades of radiographic knee osteoarthritis. Osteoarthritis Cartilage. 2009; 17(9):1177-1185.

171. Ding C, Cicuttini F, Jones G. Tibial subchondral bone size and knee cartilage defects: relevance to knee osteoarthritis. Osteoarthritis Cartilage. 2007; 15(5):479-486.

172. Bezakova E, Collins PJ, Beddoe AH. Absorbed dose measurements in dual energy X-ray absorptiometry (DXA). Br J Radiol. 1997; 70:172-179.

173. Braun MJ, Meta MD, Schneider P, Reiners C. Clinical evaluation of a high-resolution new peripheral quantitative computerized tomography (pQCT) scanner for the bone densitometry at the lower limbs. Phys Med Biol. 1998; 43(8):2279-2294.

174. Shrout PE, Fleiss JL. Intraclass correlations: uses in assessing rater reliability. Psychol Bull. 1979; 86(2):420-428.

175. Mueller TL, Stauber M, Kohler T, Eckstein F, Muller R, van Lenthe GH. Non-invasive bone competence analysis by high-resolution pQCT: an in vitro reproducibility study on structural and mechanical properties at the human radius. Bone. 2009; 44(2):364-371.

176. Johnston JD, Kontulainen SA, Masri BA, Wilson DR. A comparison of conventional maximum intensity projection to a new depth specific topographic mapping technique in the CT analysis of proximal tibial subchondral bone density. Skeletal Radiol. 2009; Epub.

177. Issever AS, Link TM, Kentenich M, Rogalla P, Burghardt AJ, Kazakia GJ, et al. Assessment of trabecular bone structure using MDCT: comparison of 64- and 320-slice CT using HR-pQCT as the reference standard. Eur Radiol. 2010; 20(2):458-468.

178. Patel PV, Prevrhal S, Bauer JS, Phan C, Eckstein F, Lochmuller EM, et al. Trabecular bone structure obtained from multislice spiral computed tomography of the calcaneus predicts osteoporotic vertebral deformities. J Comput Assist Tomogr. 2005; 29(2):246-253.

179. Messier SP. Obesity and osteoarthritis: disease genesis and nonpharmacologic weight management. Rheum Dis Clin North Am. 2008; 34(3):713-729.

180. Ellis R, Toksvig-Larsen S, Marcacci M, Caramella D, Fadda M. Use of a biocompatible fiducial marker in evaluating the accuracy of computed tomography image registration. Invest Radiol. 1996; 31(10):658-667.

181. Johnston JD, Masri BA, Wilson DR. Computed tomography topographic mapping of subchondral density (CT-TOMASD) in osteoarthritic and normal knees: methodological development and preliminary findings. Osteoarthritis Cartilage. 2009; 17(10):1319-1326.

182. Herzog W, Diet S, Suter E, Mayzus P, Leonard TR, Muller C, et al. Material and functional properties of articular cartilage and patellofemoral contact mechanics in an experimental model of osteoarthritis. J Biomech. 1998; 31(12):1137-1145.

183. Reilly DT, Burstein AH, Frankel VH. The elastic modulus for bone. J Biomech. 1974; 7(3):271-275.

184. Glantz SA. Primer of biostatistics. 4th ed. New York: McGraw-Hill, Health Professions Division, 1997.

185. Felson DT, Zhang Y, Hannan MT, Naimark A, Weissman BN, Aliabadi P, et al. The incidence and natural history of knee osteoarthritis in the elderly. The Framingham Osteoarthritis Study. Arthritis Rheum. 1995; 38(10):1500-1505.

186. Ding M, Dalstra M, Danielsen CC, Kabel J, Hvid I, Linde F. Age variations in the properties of human tibial trabecular bone. J Bone Joint Surg Br. 1997; 79(6):995-1002.

187. Ding M, Dalstra M, Linde F, Hvid I. Mechanical properties of the normal human tibial cartilage-bone complex in relation to age. Clin Biomech (Bristol, Avon). 1998; 13(4-5):351-358.

188. Choi K, Kuhn JL, Ciarelli MJ, Goldstein SA. The elastic moduli of human subchondral, trabecular, and cortical bone tissue and the size-dependency of cortical bone modulus. J Biomech. 1990; 23(11):1103-1113.

189. Williams JL, Lewis JL. Properties and an anisotropic model of cancellous bone from the proximal tibial epiphysis. J Biomech Eng. 1982; 104(1):50-56.

190. Johnston JD, LaFrance A, Wilson DR. Accuracy of Multimodality Registration of Articular Cartilage and Bone in the Hip. OsteoArthritis Research Society International World Congress on Osteoarthritis. 2006(277).

191. Altman RD, Hochberg M, Murphy WA, Jr., Wolfe F, Lequesne M. Atlas of individual radiographic features in osteoarthritis. Osteoarthritis Cartilage. 1995; 3 Suppl A:3-70.

192. Bellamy N, Buchanan WW, Goldsmith CH, Campbell J, Stitt LW. Validation study of WOMAC: a health status instrument for measuring clinically important patient relevant outcomes to antirheumatic drug therapy in patients with osteoarthritis of the hip or knee. J Rheumatol. 1988; 15(12):1833-1840.

193. Johnston JD, Steeves JB, Kontulainen SA, McWalter EJ, Masri BA, Wilson DR. Computed tomography topographic mapping of subchondral density (CT-TOMASD) in the patella: Associations with localized cartilage degeneration. . Orthopaedic Research Society; 2010 March 6 - 9; New Orleans; 2010. p. 295.

194. Johnston JD, Kulshreshtha S, Masri BA, Wilson DR. Computed tomography topographic mapping of subchondral density (CT-TOMASD) for unicompartmental knee arthroplasty pre-operative planning. International Society for Technology in Arthroplasty; 2009 October 22-24; Big Island, Hawaii; 2009. p. A972.

195. Englund M. The role of the meniscus in osteoarthritis genesis. Rheum Dis Clin North Am. 2008; 34(3):573-579.

196. Hayes WC, Keer LM, Herrmann G, Mockros LF. A mathematical analysis for indentation tests of articular cartilage. J Biomech. 1972; 5(5):541-551.

APPENDICES

Appendix A: Effects of Curvature on CT-TOMASD Measures

Synopsis

This Appendix describes our analysis of curvature effects on CT-TOMASD measured density. The analysis was conducted using CT parameters from the *ex vivo* studies (0.5 mm isotropic resolution, Chapters 2, 3 and 5) and the *in vivo* study (0.625 mm isotropic resolution, Chapter 4). Computational simulations revealed that artifacts associated with curvature along the periphery and tibial spine lead to moderate-to-large overestimations of density (periphery: < 12%; tibial spine: < 17%). However, density measures from the periphery and tibial spine account for a portion of total compartment BMD, resulting in "worst case scenario" increases in total compartment BMD of < 4%. Therefore, the effects of curvature on CT-TOMASD measured density are small.

Introduction

Due to the 2D projection nature of CT-TOMASD, excess surface curvature could lead to overestimations of true density (i.e., density measured normal to inclined surfaces). The objective of this simulation study was to test the effects of surface curvature on CT-TOMASD measured density using a simulated proximal tibial subchondral bone region with varying subchondral cortical and subchondral trabecular bone thicknesses.

Methods

Specimens

We obtained QCT images (0.625 mm isotropic voxel size) of medial and lateral proximal tibial compartments from eight individuals (1 male and 7 females; ages ranging from 34 to 71 years (mean ±

SD: 54.8 ± 10.4)). Medial and lateral compartments were oriented relative to best fit planes fit through landmark boundary points according to CT-TOMASD methodology (Chapter 2).

Surface Curvature

We measured maximum inclination of the tibial spine and outer periphery from coronal QCT images using custom algorithms (Matlab) for both medial and lateral compartments (Figure A-1). We report proximal tibial curvature using descriptive statistics (Table A-1).

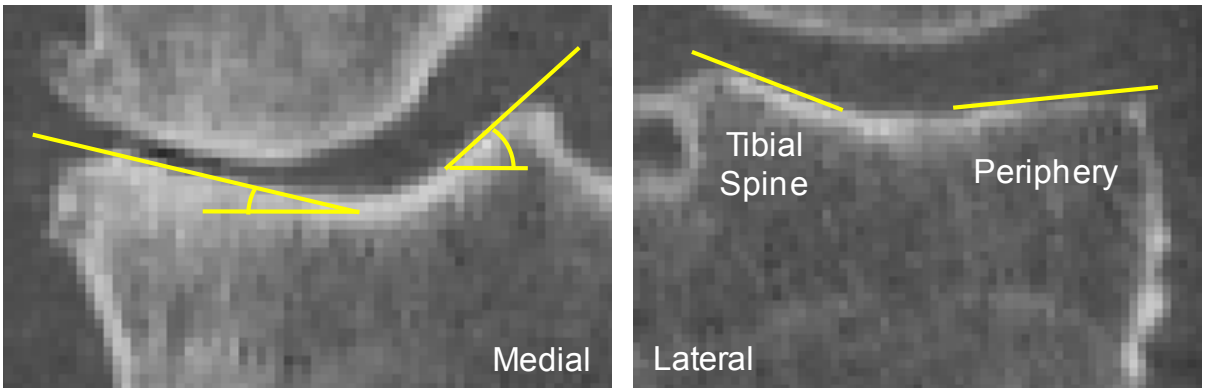

Figure A-1. Illustration of coronal QCT images of medial and lateral compartments used to determine tibial spine and peripheral inclination.

Table A-1. Average inclination (degrees °) at the tibial spine and outer periphery of proximal tibiae.

	Tibial Spine		Outer Periphery	
	Medial	Lateral	Medial	Lateral
Mean ± SD	37 ± 3.7	23 ± 5.9	11 ± 2.3	17 ± 3.0
Min	30	10	7.5	12.5
Max	40	30	15	20

Image Analysis

Using custom algorithms (Matlab), we created simulated QCT images of the proximal tibial subchondral bone region, including cartilage (equivalent imaged density = 100 mg/cm^3), subchondral cortical bone (BMD = 800 mg/cm^3), subchondral trabecular bone (BMD = 500 mg/cm^3) and epiphyseal trabecular

bone (BMD = 200 mg/cm^3) (Figure A-2). The simulated QCT images were based upon *ex vivo* studies (Chapters 2, 3 and 5) which used a 0.5 mm voxel size and the *in vivo* study (Chapter 4) which used a 0.625 mm voxel size. The thickness of subchondral cortical and subchondral trabecular bone were set as variables to test the effects of altered thickness and curvature on CT-TOMASD measured density.

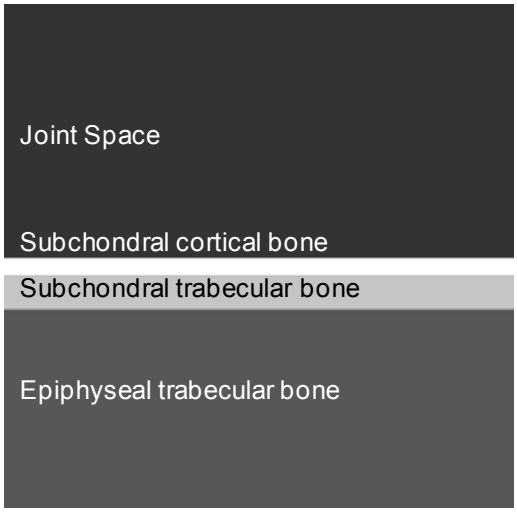

Figure A-2. Illustration of simulated QCT image of subchondral bone, including the joint space, subchondral cortical, subchondral trabecular and epiphyseal trabecular bone. The thickness of subchondral cortical and subchondral trabecular bone is variable with this simulation.

We rotated each simulated QCT image between 0^o and 45^o, and reconstructed the images using cubic interpolation. We used maximum inclination at the tibial spine (40^o) and outer periphery (20^o) as "worst case scenarios" to test the effects of curvature on CT-TOMASD measured density. We compared line-profile densities of simulated QCT images at 40^o and 20^o inclination with actual QCT imaged density at the tibial spine and outer periphery to determine which simulated bone thicknesses were representative of true morphology (Figure A-3). Along the tibial spine, the thickness of subchondral cortical bone ranged between 0.625 and 1.250 mm and the combined thickness of subchondral cortical and subchondral trabecular bone did not exceed 1.875 mm. Along the outer periphery and central regions of the proximal tibia, subchondral cortical bone thickness ranged

between 0.625 and 1.875 mm and the combined thickness of subchondral cortical and subchondral trabecular bone did not exceed 5.0 mm. We limited simulations to these specific thickness ranges.

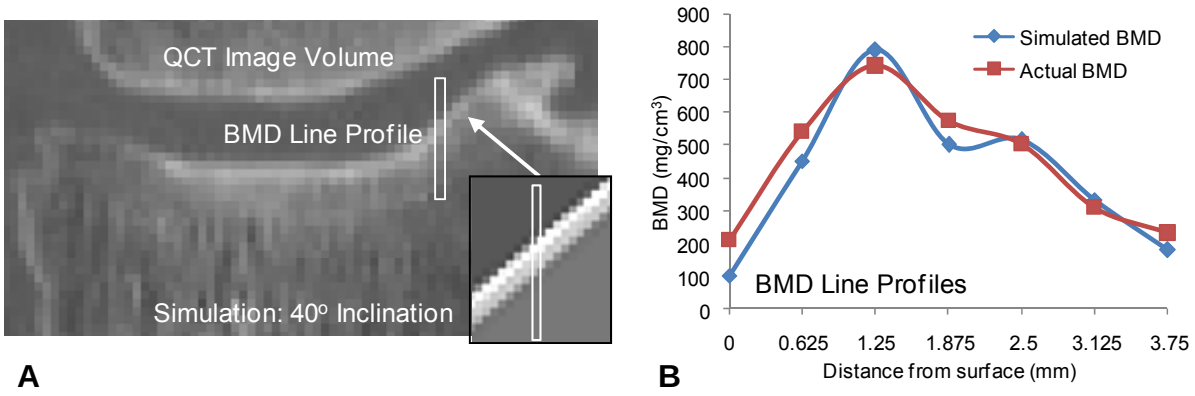

Figure A-3. Illustration of line profile comparison between simulated tibial spine and actual tibial spine BMD (*A* and *B*). The original QCT images were used to help determine which subchondral cortical and subchondral trabecular bone thicknesses represented true morphology and densities observed in QCT images of proximal tibiae (*A*).

At each 1° inclination, we conducted CT-TOMASD layers analyses (0-2.5, 2.5-5, 5-10 mm) using a 10 mm diameter region of interest. At each 1° inclination, we determined the absolute percentage change in BMD relative to 0° inclination (Figure A-4). We limited analyses to "worst case scenarios" at the tibial spine (40°) and outer periphery (20°).

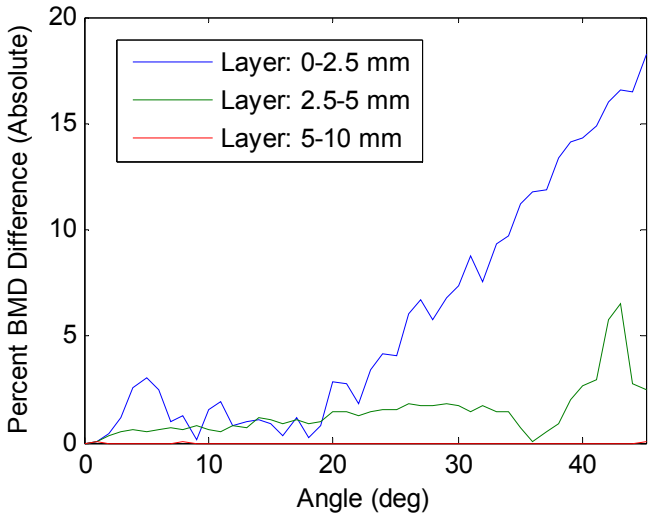

Figure A-4. Analysis of curvature effect on CT-TOMASD measured density for inclinations ranging between 0° and 45°. The effect of curvature is expressed as a percentage (%) change in BMD, expressed in relation to BMD at 0° inclincation.

We tested the effects of curvature on whole compartment BMD using approximate proportionate areas occupied by the tibial spine and outer periphery (Figure A-5). With this simple model, density measures at the tibial spine represented 1/9th of total compartment BMD while density measures across the outer periphery represented 3/9ths of total compartment BMD. For the remaining areas, we assumed curvature to be nominal with no effects on CT-TOMASD measured BMD.

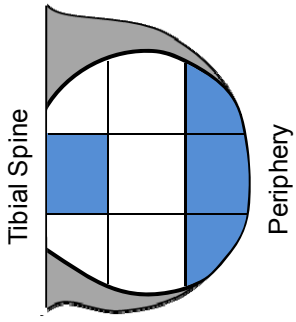

Figure A-5. Simple representation of areas occupied by tibial spine and outer periphery (BLUE).

Results

Along the tibial spine, computational simulations revealed that artifacts associated with 40° inclinations can lead to large overestimations of density (0-2.5 mm layer: < 17%, 2.5-5 mm layer: < 3%, 5-10 mm layer: 0%) (Tables A-2 and A-3). Along the outer periphery, artifacts associated with 20° inclinations can lead to moderate overestimations of density (0-2.5 mm layer: < 3%, 2.5-5 mm layer: < 12 %, 5-10 mm layer: < 10 %) (Tables A-4 and A-5).

Assuming a "worst-case scenario" of 40° inclination along the tibial spine and 20° inclination along the periphery, the combined effects of curvature on whole compartment BMD would lead to small overestimations of density (0-2.5 mm layer: 3%, 2.5-5 mm layer: 4%, 5-10 mm layer: 4%) (Table A-6).

Table A-2. Results of *ex vivo* simulation characterizing the influence of tibial spine curvature (40° inclination) on CT-TOMASD measured density. The effect of curvature is expressed as a percentage (%) change in BMD, expressed in relation to BMD at 0° inclincation. Highlighted regions indicate maximum error for different combinations of subchondral cortical (SubC) and subchondral trabecular (SubT) bone thickness for each specific CT-TOMASD layer analysis.

Thickness (mm)		Error at 40° Inclination (%)		
SubC	SubT	0-2.5 mm	2.5-5 mm	5-10 mm
0.500	0.500	12	0	0
0.500	1.000	15	1	0
1.000	0.500	17	1	0

Table A-3. Results of *in vivo* simulation characterizing the influence of tibial spine curvature (40° inclination) on CT-TOMASD measured density. The effect of curvature is expressed as a percentage (%) change in BMD, expressed in relation to BMD at 0° inclincation. Highlighted regions indicate maximum error for different combinations of subchondral cortical (SubC) and subchondral trabecular (SubT) bone thickness for each specific CT-TOMASD layer analysis.

Thickness (mm)		Error at 40° Inclination (%)		
SubC	SubT	0-2.5 mm	2.5-5 mm	5-10 mm
0.625	0.625	13	0.5	0
0.625	1.250	14	3	0
1.250	0.625	16	1	0

Table A-4. Results of *ex vivo* simulation characterizing the influence of outer peripheral curvature (20° inclination) on CT-TOMASD measured density. The effect of curvature is expressed as a percentage (%) change in BMD, expressed in relation to BMD at 0° inclincation. Highlighted regions indicate maximum error for different combinations of subchondral cortical (SubC) and subchondral trabecular (SubT) bone thickness for each specific CT-TOMASD layer analysis.

Thickness (mm)		Error at 20° Inclination (%)		
SubC	SubT	0-2.5 mm	2.5-5 mm	5-10 mm
0.500	0.500	1	0	0
0.500	1.000	2	0	0
0.500	1.500	3	1	0
0.500	2.000	1	10	0
0.500	2.500	1	10	0
0.500	3.000	1	9	0
0.500	3.500	1	9	0
0.500	4.000	1	9	1
0.500	4.500	1	0	10
1.000	0.500	1	0	0
1.000	1.000	2	1	0
1.000	1.500	0	7	0
1.000	2.000	0	8	0
1.000	2.500	0	8	0
1.000	3.000	0	7	0
1.000	3.500	0	8	1
1.000	4.000	0	1	8
1.500	0.500	3	1	0
1.500	1.000	1	7	0
1.500	1.500	0	8	0
1.500	2.000	0	8	0
1.500	2.500	0	7	0
1.500	3.000	0	8	1
1.500	3.500	0	1	8

Table A-5. Results of *in vivo* simulation characterizing the influence of tibial spine curvature (20° inclination) on CT-TOMASD measured density. The effect of curvature is expressed as a percentage (%) change in BMD, expressed in relation to BMD at 0° inclincation. Highlighted regions indicate maximum error for different combinations of subchondral cortical (SubC) and subchondral trabecular (SubT) bone thickness for each specific CT-TOMASD layer analysis.

Thickness (mm)		Error at 20° Inclination (%)		
SubC	SubT	0-2.5 mm	2.5-5 mm	5-10 mm
0.625	0.625	0	0	0
0.625	1.250	3	1	0
0.625	1.875	1	12	0
0.625	2.500	2	11	0
0.625	3.125	2	10	0
0.625	3.750	2	10	1
0.625	4.375	1	1	11
1.250	0.625	2	1	0
1.250	1.250	0	8	0
1.250	1.875	0	8	0
1.250	2.500	0	8	0
1.250	3.125	0	8	1
1.250	3.750	0	1	8
1.875	0.625	1	7	0
1.875	1.250	1	7	0
1.875	1.875	1	7	0
1.875	2.500	1	8	1
1.875	3.125	1	0	8

Table A-6. Results of *ex vivo* and *in vivo* simulations characterizing the influence of curvature on CT-TOMASD measured density across the tibial spine, outer periphery and complete compartment.

		Error (%)		
Scenario	Location	0-2.5 mm	2.5-5 mm	5-10 mm
Ex Vivo	Tibial Spine	17	1	0
	Periphery	3	10	10
	Whole Compartment	3	3	3
In Vivo	Tibial Spine	16	3	0
	Periphery	3	12	11
	Whole Compartment	3	4	4

Conclusions

Computational simulations revealed that artifacts associated with curvature along the periphery and tibial spine lead to moderate-to-large overestimations of density (periphery: < 12%; tibial spine: < 17%). However, density measures from the periphery and tibial spine account for a portion of total compartment BMD, resulting in “worst case scenario” increases in total compartment BMD of < 4%. Therefore, the effects of curvature on CT-TOMASD measured density are small.

Appendix B: Optimizing *In Vivo* QCT Scanning Parameters

Synopsis

This Appendix describes our comparisons of proximal tibial BMD obtained using different CT voltages and tube currents in an attempt to define optimal *in vivo* CT settings. Using 120 kVp voltage and 200 mA current as the reference standard, density analyses revealed that the 120 kVp / 150 mA settings offered comparable image noise, comparable density measures, and lower radiation.

Introduction

In QCT imaging of bone, radiation dosage and BMD accuracy and precision are directly related to applied CT voltage and tube current. Low voltage and tube current equate with high image noise, which negatively affects BMD accuracy and precision. Conversely, high voltage and tube current equate with low image noise and improved BMD accuracy and precision, but higher inflicted radiation. The relationship between radiation dosage and CT voltage and tube current is relatively linear. The relationship between BMD improvements and CT voltage and tube current is, however, non-linear, and a plateau exists in which large increases in voltage and current result in small improvements in BMD accuracy and precision. Optimal CT scanning parameters should (ethically) coincide with this plateau region to minimize incurred radiation dosage on patients.

A simple method to derive optimal CT scanning parameters is to compare BMD obtained with different CT scanning parameters against a reference 'gold' standard. This reference standard pertains to an object of interest (e.g., reference phantom, cadaver specimen) scanned with the highest possible CT voltage and current. By determining how much BMD differs from the reference standard, along with the standard deviation of these differences, an estimation of the plateau point and optimal CT settings can be determined. For example, a marked decrease in absolute BMD differences and standard deviations would indicate that the plateau point was in the vicinity of the respective CT settings.

For our *in vivo* precision study, colleagues at the New England Baptist Hospital in Boston, MA requested that we optimize our QCT scanning protocol to 1) minimize radiation dosage on study participants, and 2) reduce the probability of CT tube overheating. The employed CT scanner (4-slice General Electric LightSpeed) experiences regular clinical usage at the New England Baptist Hospital and is prone to overheating due to insufficient ventilation and cooling.

The objective of this preliminary pilot study was to determine optimal CT settings for *in vivo* assessment of proximal tibial BMD. Optimal CT settings were selected according to the smallest absolute BMD differences from the reference standard, smallest standard deviations of the differences, and smallest incurred radiation dosage.

Methods

Specimen

We obtained one intact fresh human cadaver knee specimen, including tissues including tissues 25 cm proximal and distal to the tibio-femoral joint line (~50 cm total length), from the New England Baptist Hospital Bioskills Center. The specimen came from a male donor aged 68 years.

Imaging Methodology

QCT Image Acquisition

We performed single-energy QCT using a clinical CT scanner (Lightspeed 4-slice, General Electric, Milwaukee, WI, USA). The cadaver knee was oriented supine and centrally located within the CT gantry. We included a solid QCT reference phantom (Model 3T; Mindways Software Inc, Austin, TX, USA) located below the knee to transform CT HU to equivalent volumetric BMD (mg/cm^3 K_2HPO_4). To prevent specimen movement during repeated CT scanning we secured the knee to the CT table using adhesive tape. Pilot analyses revealed that we were only able to obtain complete 3D datasets of the

knee without overheating when voltage and current did not exceed 120 kVp and 200 mA, respectively. We rescanned the knee, for a total of 6 scans, while varying voltage (100 and 120 kVp) and tube current (100, 150, 200 mA). Fixed CT scanning parameters included: standard bone reconstruction kernel (BONE), axial scanning plane, ~90 second scan time, ~250 slices, 0.625 mm isotropic voxel size.

Effective Dosage Calculation

We determined the effective radiation dosage (mSv) for each CT scan using scan parameters (voltage (kVp), current (mA), dose length product (MGy·cm)) and shareware software (CT-DOSE; National Board of Health, Herley, Denmark) (Table B-1).

Table B-1. Effective radiation doses incurred at the knee joint for different CT settings.

CT Parameters		Radiation Parameters		
Voltage (kVp)	Current (mA)	Dose-Length-Product (mGy·cm)	Length (cm)	Effective Dosage (mSv)
120	200	434	15.625	0.097
120	150	325	15.625	0.073
120	100	217	15.625	0.048
100	200	259	15.625	0.058
100	150	194	15.625	0.043
100	100	130	15.625	0.029

Image Analysis

BMD Conversion

We converted grayscale HU to equivalent volumetric BMD (mg/cm^3 K_2HPO_4) using linear regression equations derived from known densities contained within the reference phantom ($r^2 > 0.99$) (Matlab

2007a, MathWorks, Natick, MA, USA). For our analysis we removed QCT images of the distal femur and distal tibia; focusing primarily on the proximal tibia (44 slices, 27.5 mm length).

BMD Comparisons

Using 120 kVp / 200 mA as the reference standard, we subtract imaged BMD for each CT scan from the reference standard BMD, and computed the mean absolute BMD difference and standard deviation of the differences. We binned the densities into four groups (<250, 250-500, 501-750, >750 mg/cm^3 K_2HPO_4) to determine which imaged densities showed the largest differences from the reference standard. Binning also served to approximate image noise, whereby consistent BMD differences and standard deviations for each density range would indicate low image noise. Conversely, variable BMD differences and standard deviations would indicate high image noise.

Results

Density analyses revealed that the 120 kVp / 150 mA settings offered comparable density measures with the reference standard (Table B-2). Absolute BMD differences and standard deviations for the 120 kVp / 200 mA settings remained relatively constant for each binned density range, indicating low image noise (Tables B-2 and B-3). Radiation dosage with the 120 kVp / 200 mA setting was lower than the reference standard (Table B-1). Absolute BMD differences and standard deviations increased as CT tube current and voltage were lowered, particularly with the 100 kVp voltage setting (Tables B-2 and B-3). Absolute BMD differences and standard deviations for each density range demonstrated increased variability as tube current and voltage were lowered, indicating high image noise.

Table B-2. Absolute mean BMD difference from reference standard BMD (120 kVp / 200 mA settings).

CT Parameters		Absolute mean BMD Difference (mg/cm^3 K_2HPO_4)			
Voltage	Current	Binned BMD Range (mg/cm^3 K_2HPO_4)			
(kVp)	(mA)	< 250	250 – 500	501 – 750	> 750
120	150	50	61	62	64
120	100	75	80	84	87
100	200	90	95	103	114
100	150	97	100	110	123
100	100	105	110	122	140

Table B-3. Standard deviation of mean BMD differences (120 kVp / 200 mA settings).

CT Parameters		Absolute mean BMD Difference (mg/cm^3 K_2HPO_4)			
Voltage	Current	Binned BMD Range (mg/cm^3 K_2HPO_4)			
(kVp)	(mA)	< 250	250 – 500	501 – 750	> 750
120	150	43	48	49	51
120	100	55	63	67	69
100	200	65	76	85	95
100	150	70	80	91	104
100	100	75	87	101	119

Discussion

Using 120 kVp / 200 mA as the reference standard, density analyses revealed that the 120 kVp / 150 mA settings offered comparable image noise, comparable density measures, and lower radiation. The 120 kVp / 150 mA settings represent optimal *in vivo* QCT settings for imaging proximal tibial BMD.

The main strength of this study pertains to our use of a cadaver limb for density analyses instead of a reference phantom. Reference phantoms typically contain materials with densities below subchondral cortical bone. For example, the QCT reference phantom used to convert HU to BMD contains materials ranging in density from -50 to 375 mg/cm^3. Subchondral cortical bone, however, has

a BMD ranging between 800 and 1000 mg/cm^3, approximately. Our use of a cadaver knee as the reference object of interest ensured that density analyses would be representative of actual BMD measures of proximal tibial subchondral cortical, subchondral trabecular and epiphyseal trabecular bone.

This study has specific weaknesses related to possible movement artifacts and sample size. First, specimen movement during CT scanning may have led to variable BMD differences and standard deviations instead of image noise. However, we compared the position of the cadaver specimen from the last scan with the first scan using superposition and there was no noticeable difference in position between the two images. Second, the results of this study are limited to a single specimen, and further testing with multiple specimens may have offered different optimal CT settings. However, the range of densities exhibited by our single specimen matched BMD ranges observed during *ex vivo* analyses (n=16) and *in vivo* analyses (n=14) (Chapters 2 to 5). Our conclusion also agrees with previous findings [177, 178], in particular Patel et al [178] who reported that calcaneus bone properties assessed with 120 kVp and 150 mA did not differ substantially from those obtained with 120 kVp and 300 mA.

Conclusion

The 120 kVp / 150 mA settings represent optimal *in vivo* QCT settings for imaging proximal tibial BMD.